UNICA

UNIVERSITÀ
DEGLI STUDI
DI CAGLIARI

Ph.D. DEGREE IN PHYSICS

Cycle XXXV

Innovative silicon pixel sensors for a 4D VErtex LOcator detector for the LHCb high luminosity upgrade

Scientific Disciplinary Sectors

FIS/01, FIS/04

Ph.D. Student: Andrea Lampis

Supervisor: Dr. Alessandro Cardini

Final exam. Academic Year 2021/2022
Thesis defense: April 2023 Session

Table of contents

List of figures

List of tables

Introduction

To fully exploit the instantaneous luminosity that LHC could provide at interaction point 8, where the LHCb experiment is located, a second experiment upgrade, called upgrade II, is planned to take place during Long Shutdown 4 in 2033. In order for the experiment to improve or at least maintain the current physics performances also in the high luminosity condition, several detectors will have to be upgraded or replaced and this is particularly true for the VErtex LOcator (VELO). In fact, dedicated simulations have shown a significant decreases of the vertices and tracks reconstruction efficiencies of the current VELO detector due to the increased pile-up of the the high luminosity condition. Moreover the harsher radiation environment will also provide a higher radiation damage to the detectors, much higher than the current VELO detector can withstand. The most promising solution to recover the tracking and vertices performances in the high luminosity condition is the development of a new 4D vertex detector capable to measure the time information of the tracks by using pixel sensors with an accurate spatial and time resolution for the particles detection. This set the stage for the development of innovative pixel sensors with unmatched time resolution of the order of tens picoseconds and featuring high radiation hardness. The TimeSPOT (Time and SPace real-time Operating Tracker) project has the aim to cope with these requirements by means of new 3D silicon pixels optimized for the measurement of particle timing. The work described in this thesis has been done in the context of this project and concerns the accurate characterizations of the innovative 3D trench silicon sensors, developed by the TimeSPOT collaboration, in terms of time resolution, detection efficiency and radiation hardness. The description of the thesis structure is given in the following.

Chapter 1 describes the high luminosity phase of the LHCb experiment after the upgrade II, and in particular the technological problems to be addressed for the development of a new vertex locator detector for the LHCb high luminosity phase. Chapter 2 reports the TimeSPOT project, in which I was involved for the last 4 years, a INFN funded R&D project with the goal to develop a prototype of tracking detector

with improved time resolution, a 4D tracker. An overview of a new silicon sensor with accurate spatial and timing resolution but also high radiation hardness developed by the TimeSPOT collaboration is given. Chapter 3 describes the working principles of a silicon pixel detector, from the interaction of particles with matter to the signal formation. A strong focus on the sensor features such as the radiation hardness and the time resolution is given in this chapter. Moreover the state of the art of silicon detectors with enhanced time resolution is reported. Chapter 4 summarizes the first beam test characterization of the 3D trench silicon sensor. The results concern the amplitude characterization and the time resolution measurements of a TimeSPOT sensor. These are the first time resolution measurements of a 3D trench sensors, which have been found to be of about 20 ps although dominated by the electronic readout board noise. A summary of a simulation chain developed for a better understanding of the beam test results is also reported in this chapter. Chapter 5 reports the second beam test campaign performed at the CERN SPS H8 beam-line in which the efficiency of a 3D trench sensor was measured for the first time. Moreover, new test structures made in the second TimeSPOT sensors batch and a new electronic readout board allowed to improve the time resolution measurements with respect to the ones made during the previous beam test, which set the time resolution of a 3D trench pixel at about 10 ps. A complete sub-pixel characterization made with an infrared laser-based setup with micrometric and sub-picosecond accuracy of different 3D silicon pixel sensors is reported in Chapter 6. The characterizations includes a detailed study on the main contribution to the time resolution of a 3D sensor. Finally, the timing response of two 3D sensors are compared: a classic columnar shaped hexagonal sensor and the 3D trench pixel. Chapter 7 reports the beam test characterizations of highly irradiated TimeSPOT pixels up to a fluence of $2.5 \cdot 10^{16}\, 1\, MeV\, n_{eq}\, cm^{-2}$. The time resolution and the detection efficiency of these highly irradiated sensors are evaluated for the first time. The results shown in this chapter conclude the characterization of 3D trench sensor and show why this sensor is one of the best candidates for the future high luminosity upgrade of the LHCb experiment. The last chapter of this thesis shows a feasibility study for the implementation of a new method exploiting the VELO detector to extend the LHCb physics program. This new method aims to directly reconstruct, for the first time, charged B meson tracks in order to close the cinematic of partially reconstructed b-hadron decays. This first feasibility study aimed to evaluate the performances of such a method for the actual VELO detector but also for different detector scenarios for the high luminosity upgrade is reported in Chapter 8.

Chapter 1

The LHCb high luminosity upgrade

The LHCb experiment is one of the four main experiments of the Large Hadron Collider (LHC) located at CERN. This chapter gives a brief overview of the LHCb experiment and its future high luminosity upgrade which takes advantages of the High Luminosity phase of the LHC (HL-LHC). An overview of the first version of the LHCb VErtex LOcator detector (VELO), the Run 1 and Run 2 VELO (referred as Run 1/2 VELO in the following), with a focus on the layout of its first upgrade, the Run 3 and Run 4 VELO (referred as Run 3/4 VELO in the following) is given in this chapter. Finally, a summary of the main requirements needed for the new vertex locator of LHCb are given.

1.1 The Large Hadron Collider

The Large Hadron Collider (LHC) [13] is the the largest and most powerful particle accelerator ever built. The LHC is a two-ring superconducting accelerator installed in a circular underground tunnel of 26.7 km at a depth from 50 m to 175 m, the same tunnel used for the Large Electron Positron (LEP) collider. The accelerator is a part of the CERN accelerator complex and is located at the Franco-Swiss border near Geneva. The LHC is able to accelerate two counter-rotating beams of both protons and ions before they are made to collide. In the main operation mode of the LHC two protons beams are accelerated to a proton energy of 7 TeV and collide at a center of mass energy $\sqrt{s} = 14$ TeV. This is obtained through superconducting magnets and accelerating structures representing the state of the art of the human technologies in those fields. The LHC is the last accelerator stage of the CERN accelerator complex which, as shown in Figure 1.1, is a system that interfaces several accelerators. The acceleration process starts with the protons extractions by ionizing hydrogen gas which are accelerated

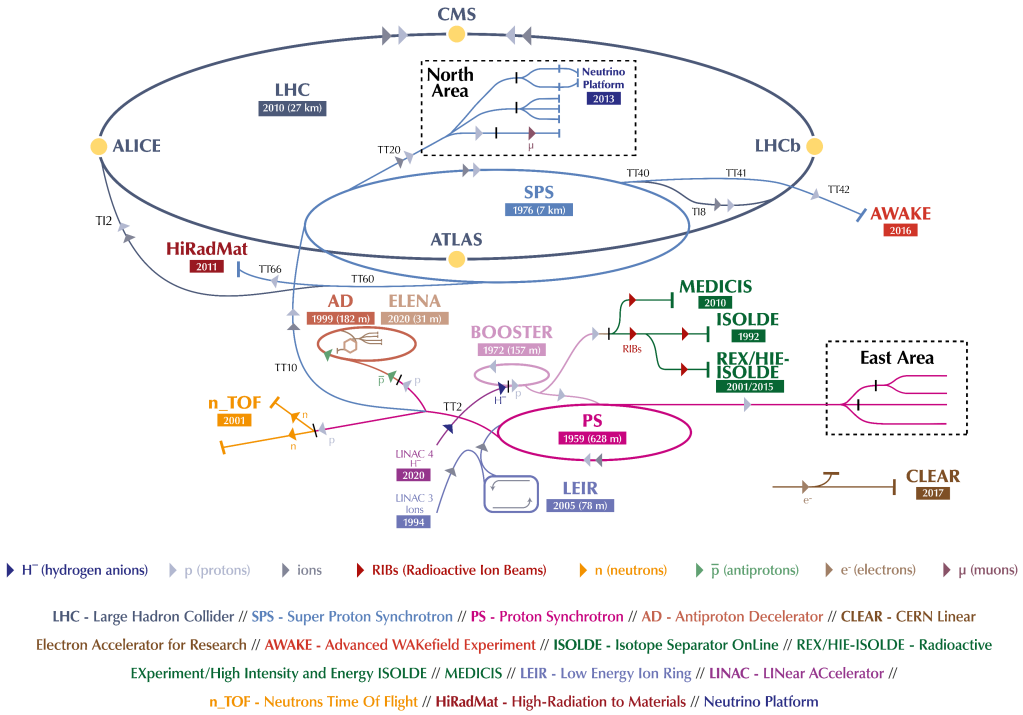

Fig. 1.1 The CERN accelerator complex [1].

up to 50 MeV and then up to 1.4 GeV by the Linear Accelerator 2 (LINAC 2) and the Proton Synchrotron Booster (PSB), respectively. The protons are then injected into the Proton Synchrotron (PS) which accelerates the protons up to 26 GeV. A last acceleration stage is needed before injecting the protons into the LHC at 450 GeV, energy obtained with the Super Proton Synchrotron (SPS). At the SPS the beam is also split and the two beams are injected into the LHC where they travel separate in opposite direction before they are made to collide in the four interaction points where the main LHC experiments, ALICE [14], ATLAS [15], CMS [16] and LHCb [17], are located. The beams inside LHC are non continuous and they typically consist of 2808 protons bunches spaced with a time interval of 25 ns, corresponding to a bunch crossing frequency of 40 MHz. Each bunch contains about $1.15 \cdot 10^{11}$ protons grouped in a length of 7.5 cm along their direction of motion. A maximum instantaneous luminosity of $2 \cdot 10^{34}\,\mathrm{cm}^{-2}\,\mathrm{s}^{-1}$ was reached by the LHC in 2018, which is a factor of two higher than the designed instantaneous luminosity. The instantaneous luminosity is not equal for all the interactions points, some experiments runs at a limited instantaneous luminosity in order to ensure a correct data taking and to prevent too high radiation damages to the detectors. In particular at the interaction point 8 (IP8), where LHCb is located, the instantaneous luminosity is reduced to $5 \cdot 10^{32}\,\mathrm{cm}^{-2}\,\mathrm{s}^{-1}$.

1.2 High Luminosity LHC

The LHC was successfully commissioned in 2010 providing an integrated luminosity of about $30\,fb^{-1}$ during the Run 1 and of about $190\,fb^{-1}$ at the end of Run 2 in 2019 and with the Run 3, started on 5 July 2022, aims to achieve a total of $400\,fb^{-1}$. To increase the statistics recorded by the experiments and extend the discoveries of the LHC a major upgrade of the LHC was foreseen. In particular an increase in the instantaneous luminosity allows to decrease the time needed to reduce significantly the statistical uncertainties of the measurements performed by the experiments at LHC [18]. This major upgrade, called High Luminosity LHC (HL-LHC), is scheduled after the end of Run 3, during the Long Shutdown 4 (LS4) and aims to bring the instantaneous luminosity up to about $5 \cdot 10^{34}\,cm^{-2}s^{-1}$, a factor five higher with respect to the actual luminosity. The schedule of this high luminosity phase is reported in Figure 1.2 and provides for three runs ending in 2039 allowing to achieve an integrated luminosity higher than $3000\,fb^{-1}$. The machine configuration of HL-LHC relies on new operation modes and a number of innovative, profoundly challenging, technologies including: 11 T to 12 T superconducting magnets, novel magnet designs, very compact superconducting RF cavities, new technologies and materials for beam collimation and high-current superconducting links [19]. The considered luminosity refers to ATLAS and CMS interaction points while in the LHCb interaction point the instantaneous luminosity will not be increased after Run 3 but only in Run 5, after the LS4. As Figure 1.3 reports, an instantaneous luminosity of $2 \cdot 10^{34} cm^{-2}s^{-1}$ is expected for Run 5, ten times higher than the Run 1 luminosity. This will allow to bring the total data collected by LHCb to $300\,fb^{-1}$ at the end of Run 6.

1.3 The LHCb detector

The LHCb experiment [20] is one of the four main experiments of the LHC. Unlike the ATLAS and CMS experiments, which are general purpose detectors, LHCb studies the Charge-Parity (CP) symmetry violation in hadrons formed by b or c quarks. These studies aim to search for New Physics (NP), beyond the Standard Model (SM), able to explain the huge asymmetry between matter and anti-matter of our Universe in parallel to the study of Rare Decays involving b, c and s quarks. The LHCb detector is a single-arm forward spectrometer. A major upgrade of the detector started after the end of Run 2, the layout of its first version stand as a reference for the upgrades and it is described in the following. The detector layout, shown in Figure 1.4, is optimized

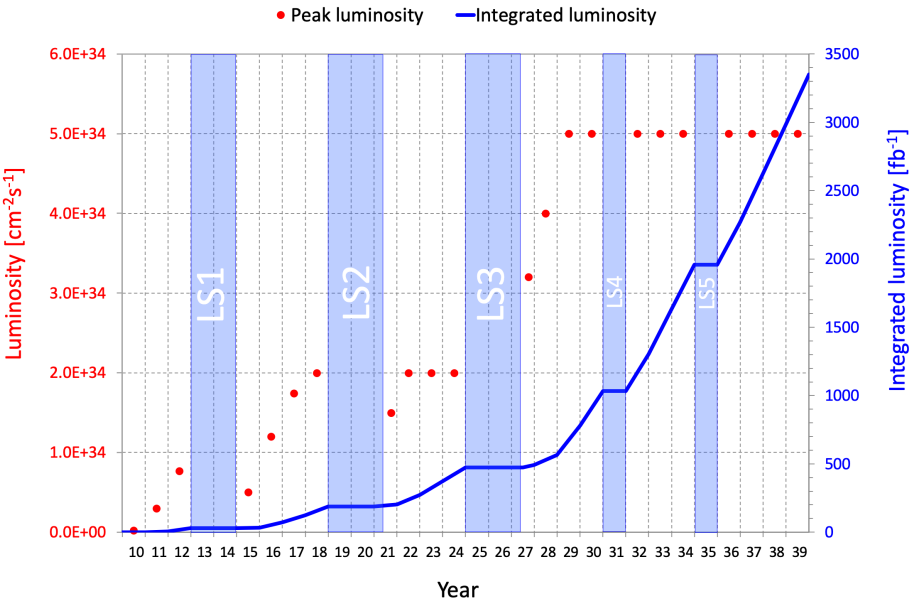

Fig. 1.2 LHC luminosity from 2010 to 2039. In red the instantaneous luminosity, in blue the integrated luminosity. The values refers to ATLAS and CMS interaction points.

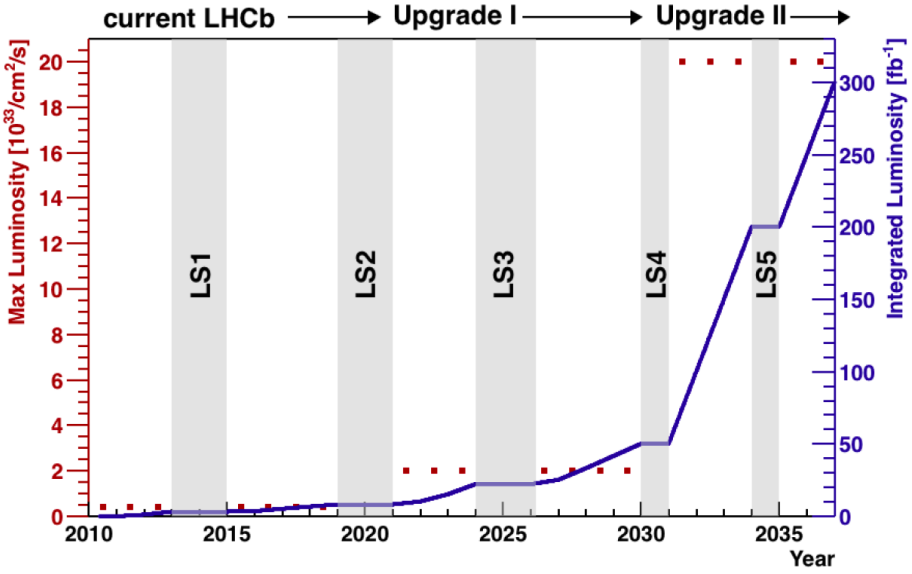

Fig. 1.3 LHCb luminosity from 2010 to 2037. In red the instantaneous luminosity, in blue the integrated luminosity.

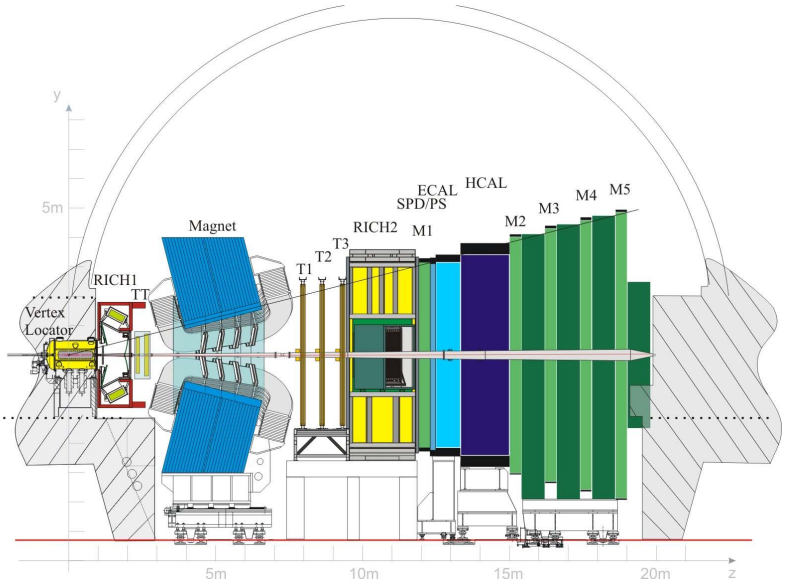

Fig. 1.4 Scheme of the vertical section of the LHCb detector.

for heavy flavour physics in fact, as the simulation of Figure 1.5 shows, $b\bar{b}$ pair are mainly produced forward or backward, with respect to the beam axis, at the high center of mass energies of the LHC proton-proton collisions. The coordinate system of LHCb is right-handed: the z axis follows the direction of the beam and goes from the interaction point towards the muon chambers, while the y axis is vertically directed and pointing upwards. The particles produced in the pp interactions are deflected on the x-z plane, called bending plane, by the magnet. The layout was designed to cover the angular region from approximately 10 mrad to 300 mrad in the bending plane and from 10 mrad to 250 mrad in the y-z plane equal to a pseudorapidity coverage between $2 < \eta < 5$ where $\eta = -ln(tan(\theta/2))$[1]. The LHCb detector assures essential requirements for obtaining top level measurements in the heavy flavour physics such as a high-performance trigger system, optimized for b-hadrons; an excellent system for primary and secondary vertices reconstructions which is essential for studying the oscillations of b-mesons and their CP violation and an excellent particle identification. These features are granted by two main types of sub-detector systems: a tracking system and a particle identification system (PID).

1.3.1 Tracking System

The LHCb tracking system provides efficient reconstruction of charged-particle tracks. These are used to determine the momenta of charged particles and, with extremely

[1] θ is the angle with respect to the beam axis.

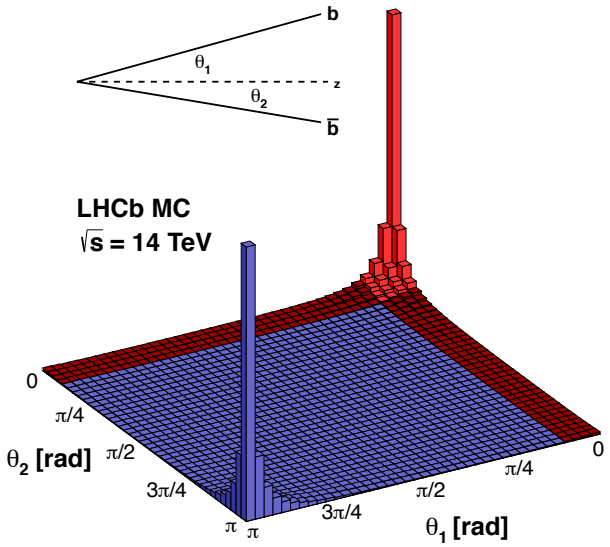

Fig. 1.5 Simulation of polar angles distribution for $b\bar{b}$ production at $\sqrt{s} = 14$ TeV. The red area represents the LHCb acceptance. Image taken from [2].

high precision, the first interaction vertices, called Primary Vertices (PV) and the secondary vertices. It consists of the VErtex LOcator system (VELO) and four planar tracking stations: the Tracker Turicensis (TT) upstream of the dipole magnet and T1-T3 downstream of the magnet. A brief description of each sub-detector of the tracking system is given in the following:

- the VErtex LOcator detector (VELO) is the sub-detector nearest to the LHCb interaction region and it is used to reconstruct the PV and the secondary vertices by means of several planes of silicon sensors. A detailed description of the VELO detector is given in Section 1.4.

- the TT consists of a system of silicon strip detectors arranged in four layers placed upstream the magnet, it has the function to determine the position of the tracks after the VELO but gives also fundamental information for the reconstructions of decay products of long lived particles.

- the dipole magnet is used together with the tracking system to measure the momenta of the charged particles through the reconstruction of their curved trajectories. A maximum magnetic field of 1.1 T can be generated by the magnet with an integrated value of 4 Tm.

- The three tracking stations placed downstream the magnet T1, T2 and T3 are composed of two separated detectors: the Inner Tracker (IT) covers the innermost region of the stations and it is made in silicon strip technology; the Outer Tracker (OT) is a drift gas detector based on straw tubes with 4.9 mm diameter vertically aligned.

1.3.2 Particle Identification system

Particle Identification (PID) is a fundamental requirement for LHCb, it has the purpose of distinguishing the different particles species produced in pp collisions. It is provided by several subdetectors: two RICH sub-detectors, Hadronic (HCAL) and Electronic Calorimeters (ECAL), and a Muon system. The Calorimeters provide identification of electrons, photons and hadrons in addition to the measurement of their energies. The Muon system provides identification of muons which is essential for many CP-sensitive measurements that have J/Ψ in their final states. Two RICH sub-detectors perform Hadron identification, in particular the ability to distinguish kaons and pions, is crucial to many LHCb analyses, particularly where the final states of interest are purely hadronic. A brief description of the sub-detectors of the LHCb PID system is given in the following:

- two Ring Imaging Cherenkov (RICH) systems exploit the Cherenkov light emitted by the particles passing trough a material, called radiator, whose characteristic Cherenkov cone depends on the velocity of the particles, and thus with the trajectory information, combined with the particle momentum it is possible to estimate the mass of the particles. Two separate RICH detectors are employed, utilising three separate radiators. The RICH 1 by using aerogel and C_4F_{10} radiators covers the low momentum charged particle range from about 1 GeV/c to 60 GeV/c while the RICH 2 with a CF_4 radiator covers from about 15 GeV/c up to and beyond 100 GeV/c.

- The calorimetry system (CALO) consists of an electromagnetic calorimeter (ECAL) followed by a hadron calorimeter (HCAL), both located downstream of RICH 2. The ECAL is composed of 66 alternating layers of lead absorber and scintillators. The scintillation light is converted trough WaveLenght-Shifting fibers and detected by photomultipliers (PMT). The ECAL measures the energy of lighter particles, such as electrons and photons. The HCAL instead, has the goal to measure the energy of the hadrons by means of alternating layers of iron and scintillators. The system is completed with two detectors, the Scintillator Pad

Detector (SPD) and the PreShower (PS). The PS is used to separate electrons, photons and pions while the SPD contributes to separate neutral particles from charged ones.

- The Muon system is composed of five stations of Multi-Wire Proportional Chambers (MWPCs), M1-M5. M1 is located upstream to CALO, while the stations M2 to M5 are located downstream. The stations are separated with 80 cm thick iron plates acting as absorbers to reduce any hadronic background that survives the calorimeters. Due to the high fluences in the inner region of M1 triple-GEM (Gas Electron Multiplier) detectors are used.

1.3.3 LHCb Upgrade I

At the end of Run 2, during the LS2, a major upgrade of the LHCb detector started. The LHCb Upgrade I [21] allows the LHCb experiment to operate to an increased instantaneous luminosity of $2 \cdot 10^{33}\, cm^{-2}\, s^{-1}$. This luminosity will bring higher statistics and thus higher occupancy and higher radiation damage to the detector, which to maintain the performances during Run 3 and Run 4 required an upgrade. Moreover the actual trigger system has been substituted by a full-software trigger able to operate at the full LHC bunch crossing frequency of 40 MHz requiring the replacement of all the electronic readouts. To cope with the increasing in luminosity several sub-detectors of the tracking systems have been replaced. A new VELO detector has been developed and installed, it is made in silicon pixels technology to cope with the higher density of charged particles to be detected, a detailed description of the VELO upgrade is reported in Section 1.4. The TT has been replaced by the Upstream Tracker (UT), a new detector having a similar layout of the the TT but made of silicon pixel sensors with improved granularity, in its innermost region, and higher radiation hardness. Finally, the IT and OT of tracking stations T1-T3 have been replaced with a single homogeneous detector based on scintillating fibers, the Scintillating Fibre (SciFi) Tracker.

1.4 The VELO detector and its first upgrade

The VErtex LOcator (VELO) provides precise measurements of track coordinates close to the interaction region, which are used to identify primary and secondary vertices. In its first version, the Run 1/2 VELO consists of a series of modules made in silicon strip technologies arranged along the beam direction, as shown in Figure 1.6. Each VELO

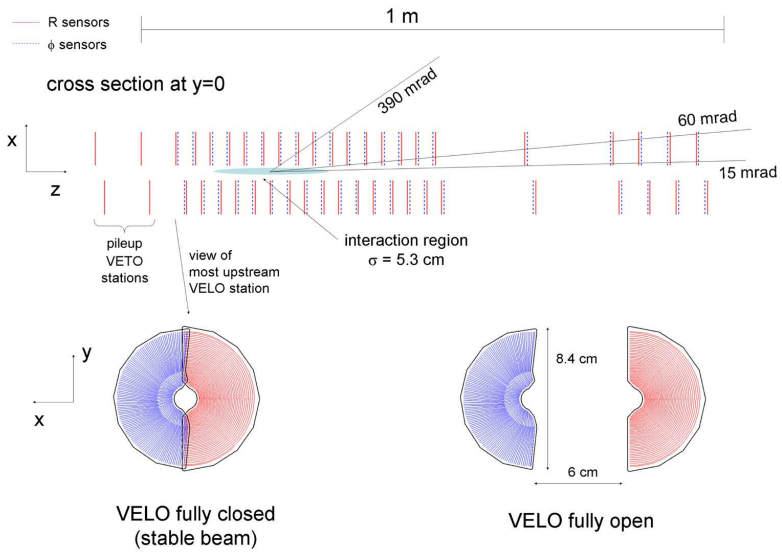

Fig. 1.6 Scheme of the VELO planes placed near the interaction region. The front face of one module is also reported in both the closed and open positions, in blue (red) part of the strips of the ϕ (r) modules are displayed.

plane is made of two silicon strip modules arranged in two different configurations. The ϕ sensors provide the information of the azimuthal coordinate, while the R-sensors measure the radial distances. The modules are mounted in a back to back configuration forming a VELO station so that a particle passing trough a plane releases an hit in both the modules. The last coordinate of the particle is given by the z position of the station. The sensors are silicon strips with a thickness of 300 μm developed in n^+ on n technology. One of the peculiarities of the VELO detector is its extremely short distance to the beamline, which for the innermost sensor is only 8.2 mm. This distance is smaller than the aperture required by the LHC during initial phases of beam injection and thus the VELO modules can be retracted and then closed when the stable beam condition is reached in the LHC.

The increase in luminosity and of the readout frequency of LHCb, starting from Run 3, required a full replacement of the VELO detector. A new VELO detector was designed and installed for the operation during Run 3/4 capable of 40 MHz readout at a luminosity of $2 \cdot 10^{33}\, cm^{-2}\, s^{-1}$. The new detector consists of two retractable halves each of them composed of 26 L-shaped silicon modules, as reported in Figure 1.7. Each module is made by hybrid silicon pixel sensors 200 μm thick developed in an n-in-p technology and bump-bonded to the readout VeloPix ASIC. The Run 3/4 VELO also features a closer distance to LHC beams of just 5.1 mm. The detector contains a total

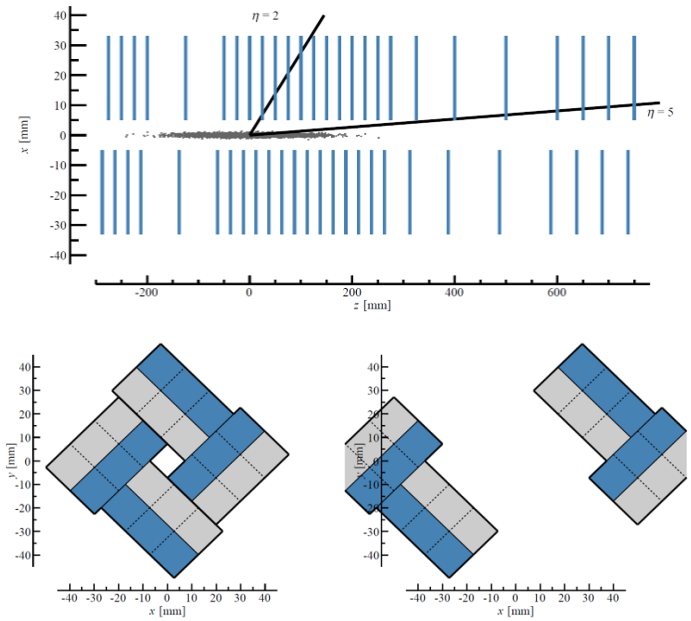

Fig. 1.7 Scheme of the new VELO planes placed near the interaction region. The front face of one module is also reported in both the closed (left) and open (right) positions. Image taken from [3].

of 41 million of pixels and a new cooling system provided by evaporative CO_2 that circulates in micro-channel cooling substrates.

1.5 The LHCb Upgrade II: the high luminosity phase

The advent of HL-LHC will provide new opportunities for the study of flavour physics which, to be fully exploited, require a further major upgrade of the LHCb detector, the LHCb upgrade II. The expression of interests for the LHCb Upgrade II was presented by the collaboration already in 2017 [4], the aim for this upgrade is to exploit an increasing of instantaneous luminosity of about 7.5 higher than the one of the Upgrade I in order to achieve an equivalent statistic higher than 300 fb^{-1} during Run 5 and Run 6. This major upgrade, scheduled for the LS4, is needed to have an efficient detector operating in a harsher environment due to the increased luminosity. The main problems to be solved are related to the increased number of particles produced by proton proton collisions which bring an higher detector occupancy, an average of about 40 proton proton collisions are expected for single bunch-crossing, but also an

increased radiation damage. For these reasons the collaboration foresees to replace all the detector subsystems with more radiation hardness ones capable to achieve the same performances of the current detector but in the high luminosity environment [20]. As a possible solution, examined by the collaboration, to cope with the increasing pile-up there is the usage of detectors with improved time resolution. In fact, a precise time measurement allows to identify events coming from different proton-proton interactions and thus improving the event reconstruction. The main efforts of the collaboration is focused on the development of innovative detectors with improved time resolution which are also enough radiation hard to survive during the whole data taking period. In the following a summary of the considerations made by the collaboration for the high luminosity upgrade of the vertex locator detector is reported.

1.5.1 A vertex locator detector for the high luminosity LHCb upgrade

A correct vertex reconstruction and its association to the proper decay plays a fundamental role for the LHCb flavour physics program. Around 2000 charged particles will be produced per each bunch crossing coming from about 40 different primary interaction vertices. These high multiplicity leads to a challenging condition for the tracks and vertices reconstruction. The performances of the Run 3/4 VELO detector have been evaluated in the harsher environment of the high luminosity upgrade by means of a MonteCarlo simulation, reported in [4], and shown in Figure 1.8. The mean rate of ghost tracks[2] in the VELO increases dramatically from 1.6% to 40% for the increased luminosity, corresponding to a reduction in tracking efficiency falling from $\sim 99\%$ to $\sim 96\%$. Moreover a modest degradation in the impact parameter (IP) resolution, due to a deterioration of the primary vertex resolution, is expected for the high luminosity operation. These results clearly show that a new detector must be developed in order to maintain the same performances of the Run 3/4 VELO detector after the high luminosity upgrade. To increase the efficiency of the event reconstruction the LHCb collaboration found as a possible solution the addition of the track time information. In fact, simulations of pp interactions made in the LHC high luminosity conditions have shown a time spread between primary vertices of about 180 ps [22] and thus by exploiting the time information, the event reconstruction could be improved. In order to obtain the timestamp of a track two main methods can be exploited: measuring the time at the hit level (4D tracking) or by using dedicated timing layers.

[2] A ghost track is a fake track reconstructed from uncorrelated hits.

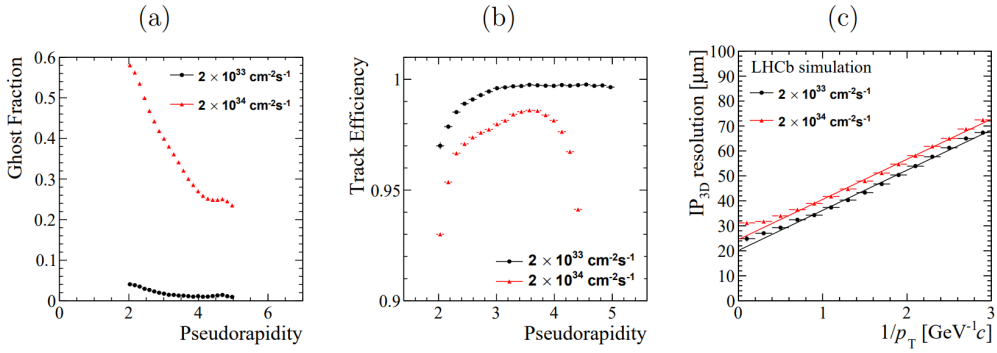

Fig. 1.8 Simulations of the VELO upgrade I performances at the high luminosity (red) and the actual luminosity (black). (a) Fraction of ghost tracks as a function of the pseudorapidity; (b) Track reconstruction efficiency as a function of the pseudorapidity; (c) Resolution of the impact parameter as a function of the inverse of the transverse momentum. Image taken from [4].

Although CMS and ATLAS used the timing layer solution, dedicated studies made for the LHCb upgrade II vertex locator found that the timing layer solution bring lower primary vertex reconstruction efficiency and lower resolution with respect to the 4D tracking solution. Because of that the 4D tracking layout is considered a preferred option for the LHCb vertex locator upgrade. Considering this option, Figure 1.9(Right) shows the primary vertex reconstruction efficiency of a vertex locator detector with the same specification of the Run 3/4 VELO as a function of the hit time resolution. The simulations show that a time resolution of about 50 ps at the hit level restores the performances of the Upgrade I VELO even at high luminosity. Figure 1.9(Left) instead, compares the primary vertex reconstruction efficiency versus the number of tracks per primary vertex for the high (U-II) and low (U-I) luminosity for a detector with 50 ps time resolution per hit (4D) and as it is during Run 3 (3D). The results clearly show the importance of implementing a 4D vertex locator detector to maintain the same vertex reconstruction efficiency of the previous upgrade.

The development of a 4D tracker poses several technological issues, mainly on the sensor technologies, its readout electronics but also on the detector services such as the cooling. Another crucial requirement for the future vertex locator detector is the radiation hardness. In fact, during all Run 5 and Run 6 a total fluence of $6 \cdot 10^{16}\, 1\, MeV\, n_{eq}\, cm^{-2}$ is expected in the innermost region of the vertex locator detector if the Upgrade I VELO layout will be maintained. Focusing on the sensors, which is the topic of this thesis, the set of requirements for the development of a 4D VELO detector to be used in Run 5 and Run 6 are:

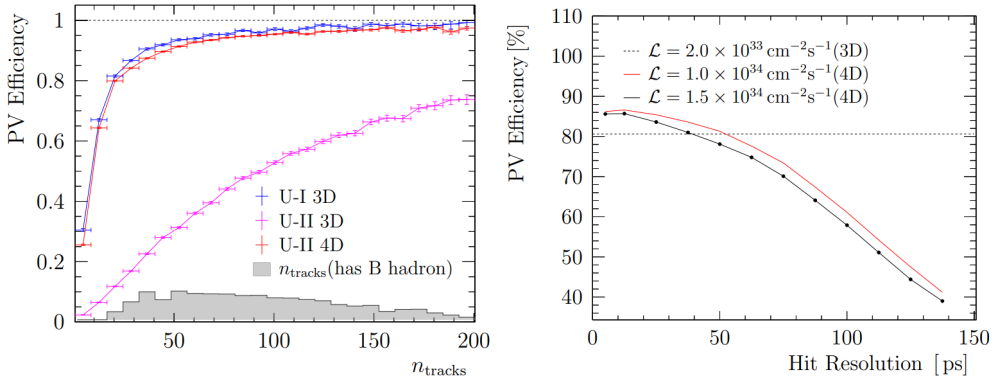

Fig. 1.9 (Left) Primary vertex reconstruction efficiency against the number of tracks per primary vertex, comparing the Upgrade I 3D reconstruction in both luminosity condition, and a variant using the time information (4D).(Right) Reconstruction efficiency against temporal resolution for different luminosity condition.

- a time resolution less than 50 ps (50 ps with the readout electronic contribution);
- a radiation hardness of about $6 \cdot 10^{16}\, 1\, MeV\, n_{eq}\, cm^{-2}$;
- a spatial resolution of about 12 μm, corresponding to a 55 μm pitch.

Currently there is no sensor able to fulfill these three requirements at the same time. This motivate the development of new technologies capable to replace the current LHCb vertex detector with a 4D tracker with high spatial and temporal resolution and unmatched radiation hardness.

Chapter 2

The TimeSPOT project

Time and SPace real-time Operating Tracker (TimeSPOT) is an INFN-CSN5 funded R&D project, that has the goal to develop a prototype vertex detector capable to cope with the challenges of tracking detectors in high luminosity colliders for high-energy-physics experiments. In this chapter the project is presented with a focus on the innovative TimeSPOT silicon 3D trench sensors whose characterizations are described in the next chapters of this thesis.

2.1 Project overview

The TimeSPOT project [23] was launched to develop a new tracking detector capable to satisfy the requirements imposed by the new high luminosity colliders experiments. In particular, looking to the high luminosity phase of the Large Hadron Collider (HL-LHC) [24], CMS and ATLAS collaborations have already defined their new inner tracking systems that will be operative already in Run 4 [25] [26]. The LHCb collaboration instead, as shown in the previous chapter, has not yet defined the design of its Phase II upgrade VErtex LOcator detector (VELO) that is scheduled to be operative for Run 5. The LHCb upgrade appears to be one of the first scenario for which the TimeSPOT innovative vertex detector could find an application.

The main problems faced by TimeSPOT are due to the increase of the luminosity and they mainly concern:

- the higher event pile-up that drastically decrease the events reconstruction efficiency;
- the higher radiation damage of the detector;

- the higher data rate to be extracted due to the higher number of charged particle to be detected.

The solution to the first problem, adopted by TimeSPOT, is the use of the time information to separate the tracks that are originated from different primary vertices, as the scheme of Figure 2.1 shows. The TimeSPOT technical solution to measure the

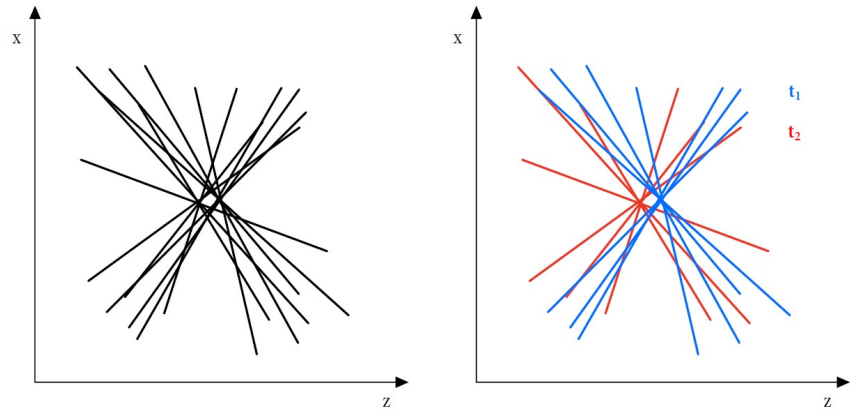

Fig. 2.1 Scheme of the reconstruction of two primary vertices event. (Left) No time information all the tracks could be associated to both vertices. (Right) The use of the time information, t_1 and t_2, allows to associate the track to the correct vertex.

time of the tracks is to add the time information at the hit level (4D tracking). This put a very high constraint on the sensor technology and on the readout electronic that must be capable to measure the hit time information, at a pixel level, with very high accuracy. Another constraint on both sensors and electronics technologies is the radiation damage that will be delivered during the entire life of the detector that, for the LHCb phase II upgrade, is estimated up to about $6 \cdot 10^{16}\, 1\, MeV\, n_{eq}\, cm^{-2}$ for the innermost region of the detector. These two features, and a very good spatial resolution $\mathcal{O}(10\ \mu\text{m})$, must be satisfied at the same time by the sensor and electronic readout. To this day, a sensor technology or a readout electronics capable to fulfill these requirements do not exist. Therefore, a dedicated R&D for the sensors and its readout was carried on during the last four years by the TimeSPOT collaboration. The main result reached by TimeSPOT is the development of an innovative sensor that, as this thesis shows, fulfill all the requirements imposed for the development of a 4D tracker in the context of the LHCb high luminosity upgrade. Moreover a first ASIC readout for a matrix of pixel capable to measure the time information from each pixel with a resolution in the order of 50 ps was developed (see Section 2.3). A final solution concerning the huge amount of data to be extracted by the detector is

still to be found, however a very promising R&D made by the Falaphel collaboration on integrated Silicon Photonics modulators [27] has started. In the next sections a detailed description of the proposed solutions for the sensor technology and for its readout are reported.

2.2 The TimeSPOT sensors

3D silicon sensors are a very promising technology for high granularity sensors for the vertex detectors. In fact with this technology small pixels can be made, with a pitch of $\mathcal{O}(50\ \mu\text{m})$ which have also shown an unmatched radiation hardness [28]. For these reasons 3D sensors are the technology chosen by ATLAS and CMS for the innermost regions of their inner tracking detectors [25] [26]. The sensors are typically realized in a single side process with a support wafer, which allows the fabrication of thin active layers (about $150\,\mu\text{m}$), small size columnar shaped electrodes ($\varnothing \sim 5\ \mu\text{m}$) and fine pitch ($\sim 50\ \mu\text{m}$). The main characteristics of 3D sensors is that the inter-electrode distance is decoupled to the sensor thickness so that, differently to planar sensors, it is possible to have very short inter-electrode distances without reducing the sensor active thickness. A short inter-electrode distance allows improving the timing properties due to a faster charge collection time, however, before the TimeSPOT project, only a single study was done in the direction of measuring the timing properties of a 3D sensor [29], but beside promising results no 3D sensor optimized for timing were ever made.

Dedicated studies on the optimizations of 3D sensor for enhanced timing performances have been done by TimeSPOT. The basic concept toward the optimization is the design of electrodes with a shape that guarantees the most uniform electric field in all the active volume of the sensor since, as reported in Section 3.6.1, it plays a key role in the timing performances of a 3D sensor. Figure 2.2 shows two classic 3D sensor geometries, and the corresponding electric field map, compared to the innovative trench geometry made by TimeSPOT. The trench geometry features a more homogeneous electric field in all the pixel volume compared to the five columns geometry, used by ATLAS, and to the nine columns sensor. The results shown before have led TimeSPOT to choose an electrode shape very similar to a planar geometry and, since the electrodes are built through the sensor thickness, it is called the trench geometry. The layout of the 3D trench sensor is shown in Figure 2.3 and 2.4. The sensor has a n-in-p doping profile which guarantees higher electron collection efficiency also after high radiation damage provided to the sensor [30]. The pixel dimensions is chosen to have a bonding pitch of 55 μm in order to be compatible to the TIMEPIX readout and processing

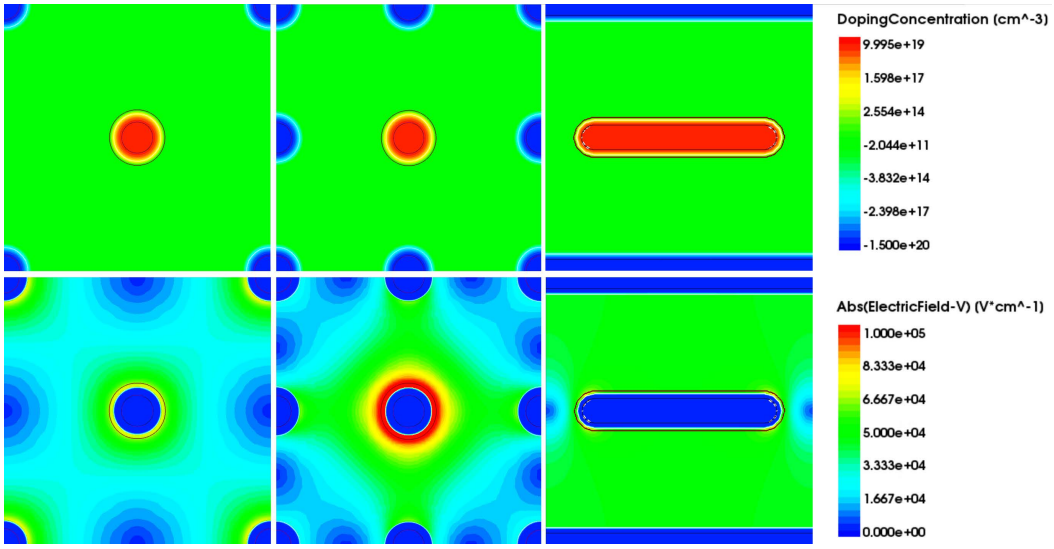

Fig. 2.2 TCAD 2D model simulation of three different electrode geometries at bias voltage $V_{\text{bias}} = 100$ V. From left to right: 3D five columns electrodes, 3D nine columns electrodes, 3D trench. (Top) the electrode geometries and doping profiles. (Bottom) electric field inside the sensible area. The 3D trench geometry presents a more uniform electric field.

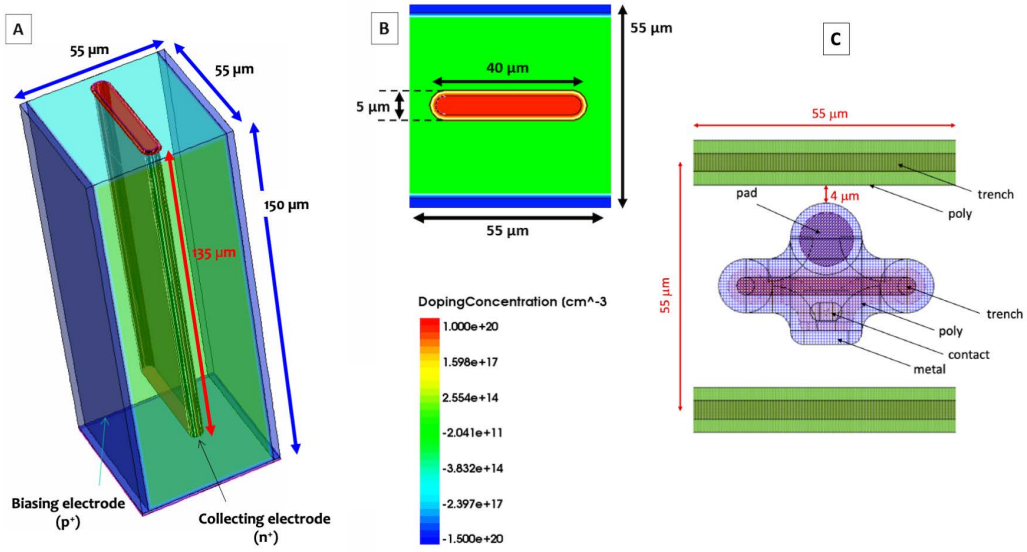

Fig. 2.3 Geometry of the designed 3D trench pixel, showing dimensions and doping profiles (red for n++ doping, green for p- doping and blue for p++ doping). (A) 3D rendering. (B) Pixel section showing the electrode configuration. (C) Pixel layout.

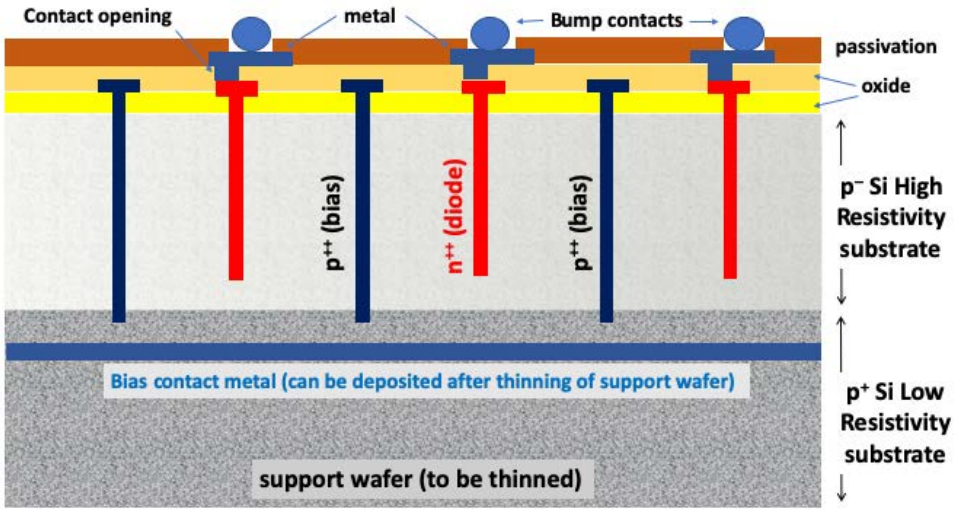

Fig. 2.4 Structure of a 3D trench sensor (not on scale). The sensitive volume (p Si substrate) has a thickness of 150 μm and a resistivity of about 5 kΩcm. The support wafer has a thickness of 500 μm and has very low resistivity (some Ωcm). The support wafer is usually, but not necessarily, thinned out.

ASIC [31]. The electrodes configuration presents two external ohmic-wall electrodes which are shared over an entire pixel line of a matrix and provide the bias voltage to every pixel. The depth of the sensitive volume is 150 μm, a trade-off between a safe silicon thickness to achieve good electrodes shape uniformity during the fabrication process and a sufficient amount of energy deposited by a MIP (about 2 fC). The collecting electrode, placed between the two ohmic-wall electrodes, is 135 μm deep. Two batches of sensor were fabricated by Fondazione Bruno Kessler in 2019 and 2021 using the Deep Reactive Ion Etching (DRIE) MEMS technique (Bosch process [32]). Several test structures were produced in the two batches with different metallizations that allow to readout, with a single amplifier channel, single pixels, double pixels and pixel-strips (see Figure 2.6). Moreover, matrices of 32×32 3D trench pixels have been produced to be bump-bondend to the TimeSPOT ASIC. Figure 2.5 shows a Scanning Electron Microscope (SEM) view of a section of one of the 3D trench test structures. The sensors have typical leakage current of about 10 pA per pixel at a bias voltage of -50 V and a capacitance of about 100 fF. The typical breakdown voltage ranges from -150 V to -200 V [33].

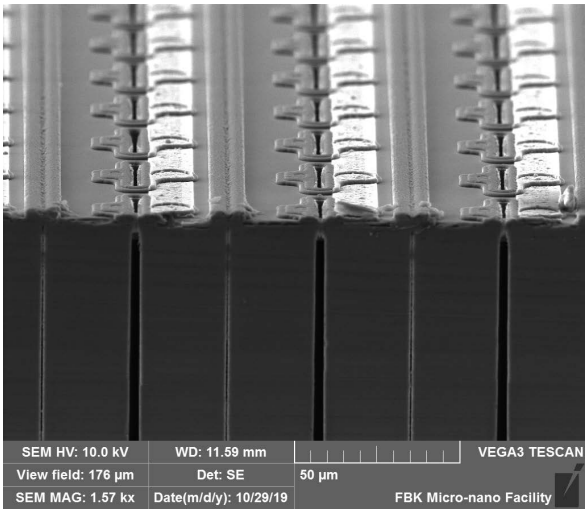

Fig. 2.5 Scanning Electron Microscope image of a section of a 3D trench test structure.

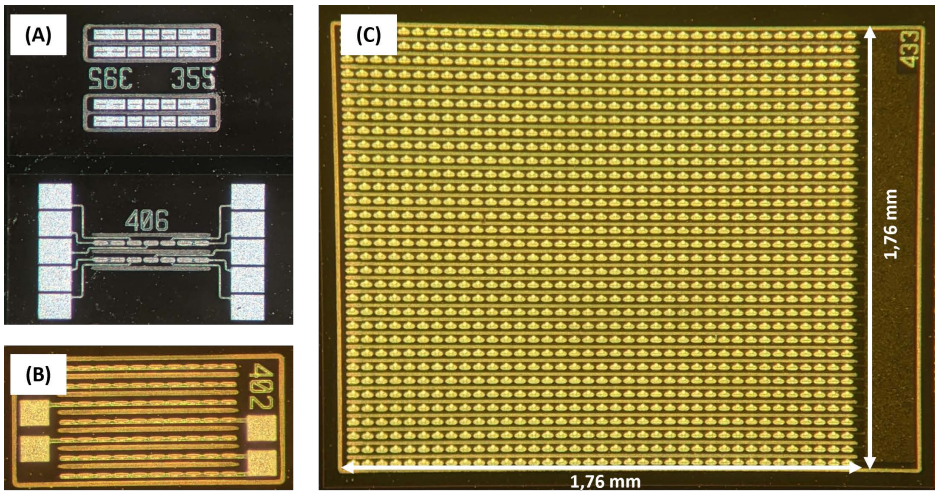

Fig. 2.6 TimeSPOT 3D trench test structure. (A) single and double pixels; (B) pixel-strip sensors; (C) a 32×32 pixel matrix.

2.3 A 28 nm CMOS ASIC: the Timespot1

The TimeSPOT project aimed to develop a complete vertex detector for future generation colliders. All the problems reported so far do not concerns only the sensor performances but they must be satisfied also by its readout electronics. Specifically to the $\mathcal{O}(10\ \mu\text{m})$, time resolution below 50 ps per hit and the high radiation hardness requirement it is important to notice that they must be satisfied also at high input hit rates $\mathcal{O}(100\ \text{kHz})$ while keeping the overall power density typically well below 2 W/cm^2. No device has been yet produced nor designed matching such set of requirements. The TimeSPOT collaboration started a dedicated development to study possible technical solutions and a first sensor readout ASIC has been developed in 28 nm CMOS technology, the Timespot1. This technology has been chosen due to its improved radiation hardness and because of the higher transistor density with respect to less scaled technologies. The scheme of this innovative ASIC consists of a charge pre-amplification stage followed by a discriminator and a TDC used for the measurement and the digitization of the time of arrival information. The Timespot1 chip integrates 1024 channels and is able to read a matrix of 32 $\times$ 32 TimeSPOT 3D trench pixels. Each channel is equipped with its own Analog Front-End (AFE) and Time to Digital Converter (TDC) allowing to measure the ToA and the Time over treshold (ToT) from each pixel. The block architecture of the ASIC is shown in Figure 2.7. The channels are organized in two blocks of 512 pixels, each one consisting

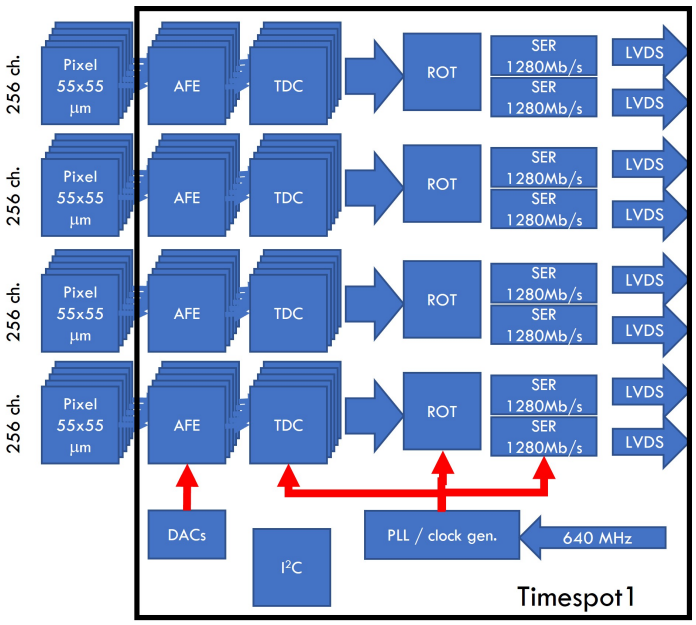

Fig. 2.7 Scheme of the TimeSPOT 1 ASIC.

of 2 groups of 256 channels. Each group have a dedicated Read Out Tree (ROT) block that collects the data from the channels, assigns them a global timestamp and sends the formatted data to one of the two serializers connected to LVDS drivers, to send the data to the acquisition system. The ASIC have a total of 8 LVDS drivers each of them able to sustain a data rate of 1.28 Gbit/s, with an overall nominal data throughput of 10.24 Gbit/s. First measurements of the Timespot1 have shown an average time resolution for the AFE of about 40 ps, and of about 23 ps for the TDC [34]. The ASIC has been recently hybridized (see Figure 2.8) on 3D trench silicon sensor matrix. Using the TSPOT1-PCB the hybrid will be characterize by means of the infrared laser setup shown in Chapter 6.1 and with a dedicated setup with radioactive sources. Several hybrids will be then used as detection planes of the TimeSPOT final demonstrator which will be characterize in a beam test campaign in 2023, to prove the tracking and timing capabilities of the entire system.

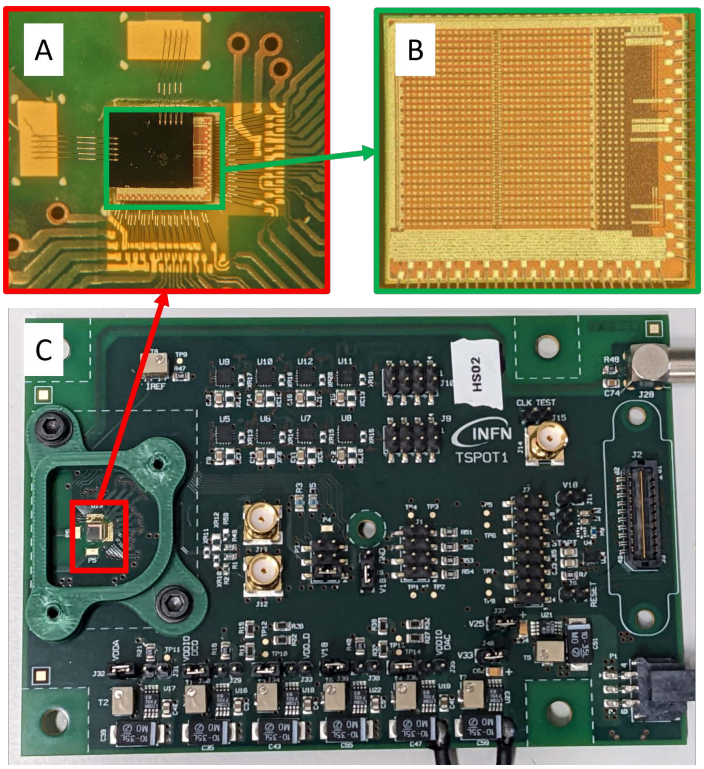

Fig. 2.8 The TimeSpot1 Hybrid wire bonded to the TSPOT1-PCB: (A) Magnification of a 3D trench pixel matrix bump-bonded to the TimeSPOT1 ASIC;(B) The top surface of the TimeSPOT1 ASIC; (C) The TSPOT1-PCB hosting a TimeSPOT1 hybrid, the hybrid is inside the red box.

Chapter 3

Silicon pixel sensors with enhanced time resolution

Silicon pixels are the sensors typically used to track the particles very near to the primary vertices of proton proton collisions in high-energy physics colliders. The basic concept of these detectors is that if a particle pass through a small pixel it is possible to determine the accurate position of the particle, if multiple positions are measured by means of different pixelated planes placed along the particle path, it is possible to reconstruct the tracks of particles and through them the production and/or decay vertices position can be reconstructed as well. This chapter describes the basic principles of charged particle detection by means of silicon pixel sensors. The mechanisms of particle interaction with the detector material are reported with also a brief summary of the basic principle of the signal formation. Detector properties crucial for the high luminosity upgrades are also presented such as the radiation hardness of silicon devices and an overview of the timing performances of these sensors. Finally, a description of the state of the art of silicon pixel sensors with enhanced timing performances concludes this chapter.

3.1 Passage of particles through matter

A charged particle passing through a material interacts in different ways with the matter components. These interactions allow to detect the particles when they pass through a material. For charged particles the most common processes are the electromagnetic interactions with the atomic electrons [35, 36, 5]. A distinctions must be made between heavy charged particles and light charged particles, where heavy means particles heavier than electrons. In the following only the case of heavy charged particle is considered.

The interactions can cause excitation of the involved electrons to a higher energy level or to a ionization of the atoms for which, if enough energy is exchanged, the bound between the electron and its nucleus breaks. Moreover there is the chance that a ionized electron has enough energy to cause, in turn, secondary ionization; these secondary electrons are called delta rays. The particles lose a small fraction of its energy in a single interaction so during their passage through a material several interactions with multiple electrons occurs. The measurements of the energy released by the particle on a material, that interaction by interaction is ruled by stochastic processes, allow to detect particles that passes through a material. The mean rate of energy loss is described by the Bethe-Bloch equation [35]:

$$-\frac{dE}{dx} = 2\pi N_A r_e^2 m_e c^2 \rho \frac{Z}{A}\frac{z^2}{\beta^2}\left[ln\left(\frac{2m_e c^2\beta^2\gamma^2 W_{max}}{I^2}\right) - 2\beta^2 - \delta - 2\frac{C}{Z}\right], \qquad (3.1)$$

where N_a is the Avogadro number, r_e and m_e are the electron classical radius and mass, ρ, Z and A are the density, the atomic number and mass number of the absorbing material, z is the charge of incident particle in units of electron charge, W_{max} is the maximum energy transfer in a single interaction and I is the average excitation and ionization potential of the absorber element. C and δ are the shell and the density corrections to the Bethe-Bloch formula which become more important for the low and high particles energy, respectively. The shell correction takes into account the case in which the velocity of the incident particle is comparable or smaller than the orbital velocity of the bound electrons, while the density correction adds to the formula the effect of the charged particles that are able to polarize the atoms of the material along their paths. The Bethe-Bloch equation is valid only in the $0.1 \leq \beta\gamma \leq 1000$ range. Figure 3.1 shows the mean rate of energy loss, also referred as stopping power, for positive muons in copper as a function of $\beta\gamma$ [5]. It is shown that for low energy particles the energy loss decreases as the $1/\beta^2$ dominant factor. This trend extends to $\beta\gamma \sim 3 \div 3.5$ for which a minimum is located. The location of the minimum for different crossing particles and for different materials is almost the same. Particles with energy near to the minimum value of the stopping power are called Minimum Ionizing Particles (MIP). Those particles assume an important role for sensors characterizations since they allow to test the detectors in the worst possible condition, which is the one of minimum energy released in the detecting material. For particles with higher energy than a MIP the logarithmic term of the equation became dominant with a resulting increase of the stopping power as $\beta\gamma$ increases.

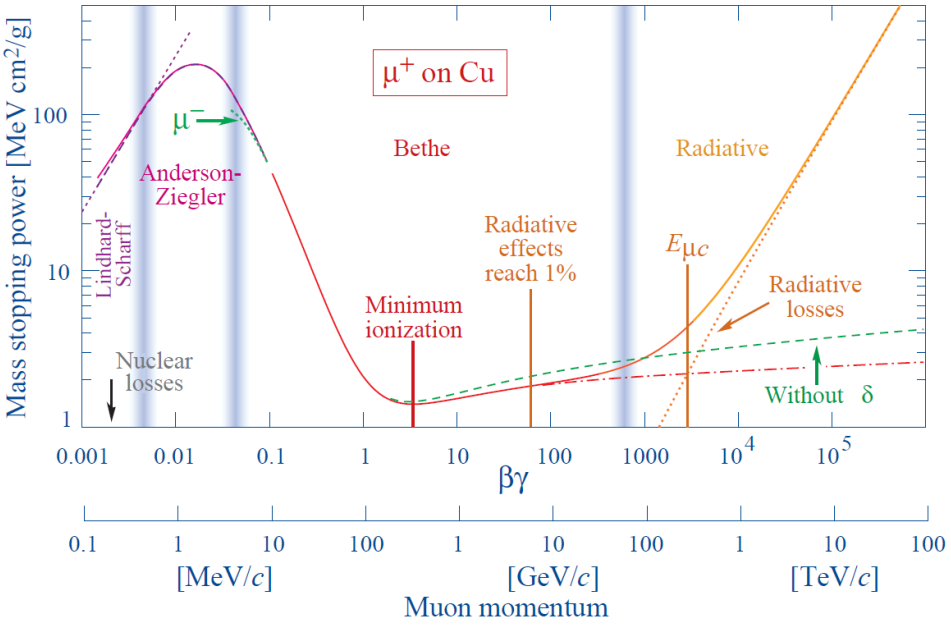

Fig. 3.1 Stopping power $-dE/dx$ for positive muons in copper as a function of $\beta\gamma = p/Mc$ [5].

The Bethe-Bloch equation represents a valid model for the mean energy loss of particles passing through matter, however the total energy exchanged depends on the number of interactions that the particles have with the component of the matter. This makes the total energy lost dominated by the statistics fluctuations of the number of collisions that occurs. For relatively thick detectors, a large number of collisions occurs and thus the total energy loss distribution is expected to have a Gaussian shape according to the Central Limit Theorem. Particles passing through thin detectors however, produce less number of collisions and thus the energy fluctuation of each interaction is more dominant. Typically this fluctuations are dominated by the delta rays production which, as previously described, allow higher energy loss. The resulting energy loss distribution for thin sensors deviates from a Gaussian and became asymmetric with a tail of high energy loss, as shown in Figure 3.2 [5]. While the inelastic interactions of the particles with the electrons of the material are the main contributions of the energy loss, several elastic Coulomb interactions with the nucleus can deflect the directions of particles, as reported in the scheme of Figure 3.3. The scatter angle of a single interaction typically is very small, but many interactions can cause a net particle deflection. The Central Limit theorem predict that the tilt angle is distributed as a Gaussian and experimental measurements taken from [37] show that

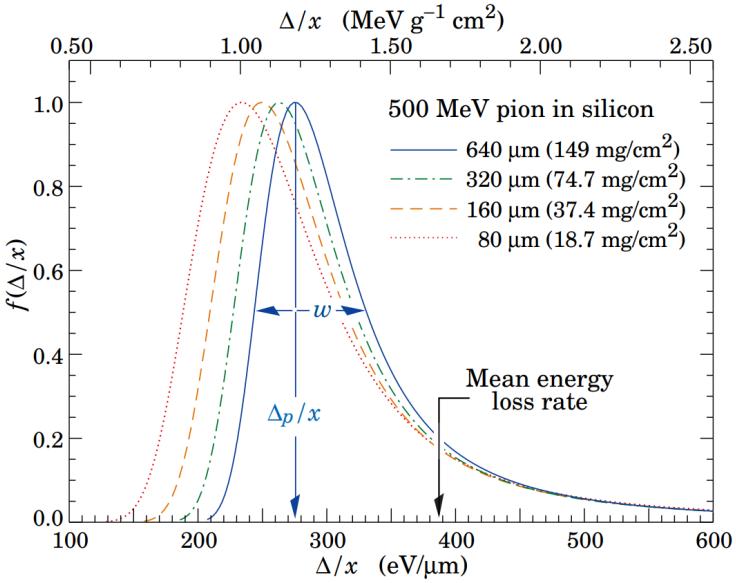

Fig. 3.2 Energy loss distribution of 500 MeV pions passing through silicon sensors of different thickness [5].

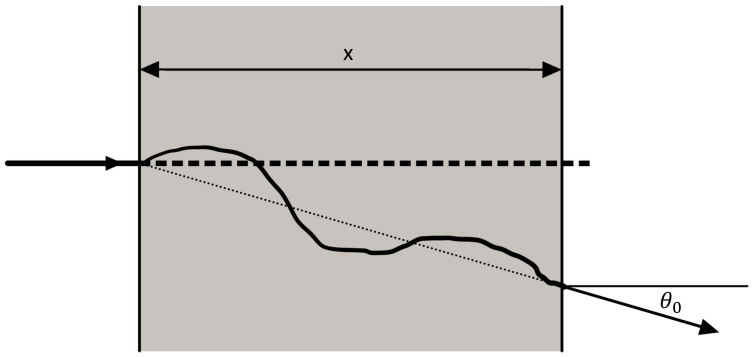

Fig. 3.3 Scheme for the multiple Coulomb scattering. A particle passing through a material can be deflected with an angle θ_0 with respect to its initial direction.

the RMS of the angular distribution θ_0 is given by:

$$\theta_0 = \frac{13.6 \text{ MeV}}{\beta cp} z \sqrt{\frac{x}{X_0}} \left[1 + 0.038 ln \left(\frac{xz^2}{X_0 \beta^2} \right) \right], \tag{3.2}$$

where βc, p and z are the velocity, momentum and charge expressed in electron number of the particle and x/X_0 is the thickness of the scattering medium in radiation lengths.

This concludes this brief description of particle interaction through the material. The particle detection, as described, can modify the properties, such as the energy or the direction of the particles. This puts a severe constraint on the thickness of the sensor used in tracking detectors.

3.2 Energy conversion in silicon and basic operation principles

Semiconductor detectors base their working principle on the direct conversion of the energy deposited by a particle to free electron-hole pairs, which can be collected by an electric field. The motion of such charges causes a current induction on the detector electrodes which, after its amplification by means of a pre-amplifier electronic circuit, became measurable and it can be used to detect the passage of a particle.

Semiconductors, such as silicon, are materials characterized by energy bands for the electrons separated by a forbidden energy region, called the band gap. The higher energy band for the electron is the conduction band, only electrons with an energy inside this band can conduct a current inside the semiconductor. This because, unlike the low-energy electrons which are in the valence band, the electrons in the conduction band have enough energy to be unbounded from the atoms of the material. The detection process of semiconductor devices is based on the energy transfer from the particles to the electrons in valence bands, which if enough energy is exchanged, can be promoted to the conduction band and thus they can be collected by an electric field. The value of the band gap distinguishes a semiconductor from an insulator and a conductor. Conductors have no energy gap while semiconductors differ from insulator materials for a lower energy gap. The energy gap of Silicon is 1.12 eV, while insulator materials have typical energy gap of 5 eV or higher. Another important feature of semiconductors is that a current circulating inside them it is formed by two charge carriers: the electrons of the conduction band and the vacancies in the valence band, called holes. The holes are electron vacancies in the valence band left when electrons

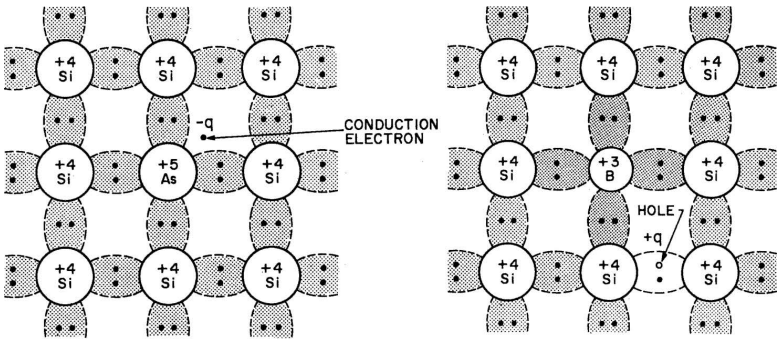

Fig. 3.4 Representation of the bonds in doped silicons: (left) arsenic is used to obtain n-type silicon bringing an electron in conduction band; (right) p-type silicon obtained with boron as a dopant, leading to a formation of a mobile hole in valence band.

are promoted to the conduction band. Although the energy gap in silicon is 1.12 eV a mean energy of 3.6 eV [38] is needed to create an electron-hole pair, this is due to the fact that part of the deposited energy is used for phonon generation [39].

The use of intrinsic silicon as a particle detector would not be possible without advanced cooling techniques or methods allowing the removal of free charge carriers in the sensor. In fact in the case of an intrinsic silicon with the same size of a typical sensor used in high energy physics, there are about 10^9 free charge carriers. This number is several order of magnitude higher than the number of electrons induced by an ionizing particle in a sensor of typical thickness used in high energy physics experiments. The resulting signal would be completely dominated by the free charge carriers already present in the sensor. The removal of free charge carriers in a semiconductor sensor is obtained by making a p-n junction.

3.2.1 The p-n junction

It is possible to modify the free charge carriers concentration in silicon by acting on its composition with a process called doping. In particular, it is possible to replace silicon atoms with atoms having one more valence electron, called donor atom, or one less, acceptor atom. In the first case atoms from the Group V replace some silicon atoms while in the second the silicon atoms are replaced by atoms from the Group III, as shown in Figure 3.4. The addition of acceptor atoms has the effect to increase the number of holes in the conduction band and in this case the doped silicon is known as p-type. The donor atoms instead, increases the number of electrons in the conduction band, in this case the extrinsic silicon is called n-type. These phenomena occur because the dopant atom adds energy levels in the forbidden region, just above the valence

band (p-type) or just below the conduction band (n-type). For the n-type the new levels are at first occupied by the excess electrons given by the donor atom which, by thermalization, can be promoted in the conduction band. For a p-type silicon instead, the new levels just above the conduction bands allow to valence electrons to be promoted and thus leaving mobile holes in the valence band. This mechanism allows, by varying the dopants concentration, to control the number of majority carriers, which are electrons for n-type and holes for p-type silicon. The introduction of the dopants does not just increase the concentration of electrons (holes) for n-type (p-type) but also reduces the number of the minority charge carrier, since according to the mass action law the product between the two charge carriers concentrations must be constant:

$$np = n_i^2, \tag{3.3}$$

where n, p are the the density of free electrons and holes in the doped silicon, while n_i is the density of free electrons[1] of intrinsic silicon.

A p-n junction is a doping configuration in which a n-type silicon is in close contact to a p-type silicon. The difference in charge concentration of electrons and holes between these two zones originates a diffusion current through the junction. This current leads to the formation of a net charge density in the two zones: positive for the n-type and negative for the p-type. The formation of the charge density creates a potential between the two zones, the built-in potential. The electrical potential counteracts the diffusion current until an equilibrium is reached. At the equilibrium a zone free of charge carriers is created, that zone is called depletion region. The depletion region is the active zone of a particle detector and thus the electron-hole pairs generated by the passage of a particle in this region can induce a significant signal on the readout electrodes of the sensor. The depth W of the depletion region depends on the dopants concentrations of the two zones N_D for the n-type and N_A for the p-type and for a planar geometry can be evaluated as:

$$W = \sqrt{\frac{2\epsilon V_0}{e}\left(\frac{1}{N_A} + \frac{1}{N_D}\right)}, \tag{3.4}$$

where ϵ is the silicon dielectric constant and V_0 is the built-in potential. It is possible to increase or decrease the depth of the depletion region by applying an external voltage on the p-n junction, in particular by applying an higher potential on the n-side with respect to the one of the p-side the depletion region increase. This configuration, shown

[1] For intrinsic silicon $n = p = n_i$.

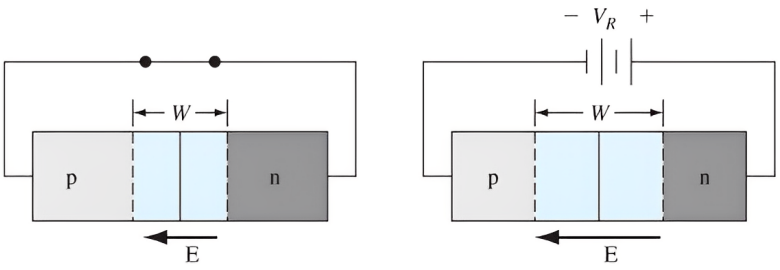

Fig. 3.5 Scheme of a p-n junction: (left) unbiased p-n junction; (right) reverse biased p-n junction, the depth of the depletion region increases compared to the unbiased condition.

in Figure 3.5 is called reverse bias, and is the standard operation of silicon particle detectors. The maximum reverse bias voltage is the breakdown voltage. In fact for higher voltages, the free charge carriers obtain enough energy to ionize other electrons which start an avalanche multiplication that can even damage the detector.

3.3 Signal formation

The motion of charges inside the sensor active area induces a current on the sensor's electrodes [40].

The Ramo-Schockley theorem [41] provides a simpler way, with respect to the charge image theory, to evaluate the induced current I by a charge carrier q moving among electrodes, that is expressed as:

$$I = q\vec{E}_w \cdot \vec{v}_d \tag{3.5}$$

where $\vec{E}_w$ is the weighting field and $\vec{v}_d$ is the drift velocity of the considered charge carrier. The weighting field is a quantity related only on the electrodes geometry and is a vector field calculated by solving the Laplace Equation by removing the charge carrier, setting a unit potential to the given electrode and zero potential to all the other electrodes. The total induced current can be approximated as the sum of the current contributions of all the charge carriers. Another useful process that rules the signal formation in semiconductor detectors is the motion of the charge carriers through the silicon. In fact electrons and holes in presence of an electric field drift with an average drift velocity that is:

$$v_d = \mu E \tag{3.6}$$

where μ is a quantity that takes into account the energy exchange between the moving charge carriers and the silicon lattice, and it is called mobility. Electrons and holes in silicon has a different mobility, electrons are faster than the holes, but their mobility also depends on the temperature. Typical values of electrons and holes mobility for silicon at room temperature are $\mu_e = 1350\,\mathrm{cm^2\,V^{-1}\,s}$ and $\mu_h = 480\,\mathrm{cm^2\,V^{-1}\,s}$. However at high electric fields the scattering of carriers is significantly influenced by carrier heating and a saturation of the velocity of the charge carriers is observed [42]. These elements allow to calculate the current generated between two planar electrodes using some approximations. The example of a planar-like p-n junction facilitate the comprehensions of the current signal generated by a silicon sensors and its variation, which for a 3D trench sensor is characterized in detail in Section 6.4.2. With the assumptions of parallel plates much larger compared to the distance d between them, the weighting field has only one component E_w in the orthogonal direction of the plates,and is equal to [41]:

$$E_w = \frac{1}{d}, \tag{3.7}$$

while the other components are null. If a potential difference V_b, much larger than the built-in potential, is applied to the plates an electric field in the direction between the plates is generated which is equal to:

$$E = \frac{V_b}{d}. \tag{3.8}$$

Using the Ramo-Schokley theorem the current given by a single charge carrier can be evaluated as:

$$I = \frac{q\mu V_b}{d^2} \tag{3.9}$$

which is obtained by replacing Equation 3.6, 3.7 and 3.8 to Equation 3.5. If an electron hole pair is generated at a distance x from the positive electrode, as reported in Figure 3.6, the electron and the hole start to drift towards the positive and negative electrodes respectively. Assuming a uniform drift velocity for both the charge carriers a constant current is induced at the electrodes:

$$I = I_e + I_h = \frac{q\mu_e V_b}{d^2} + \frac{q\mu_h V_b}{d^2}. \tag{3.10}$$

The current is induced until each charge carrier reaches the corresponding electrode. The time interval between the pair formation and the time in which the charge reaches the electrode is called charge collection time, which, according to the previous

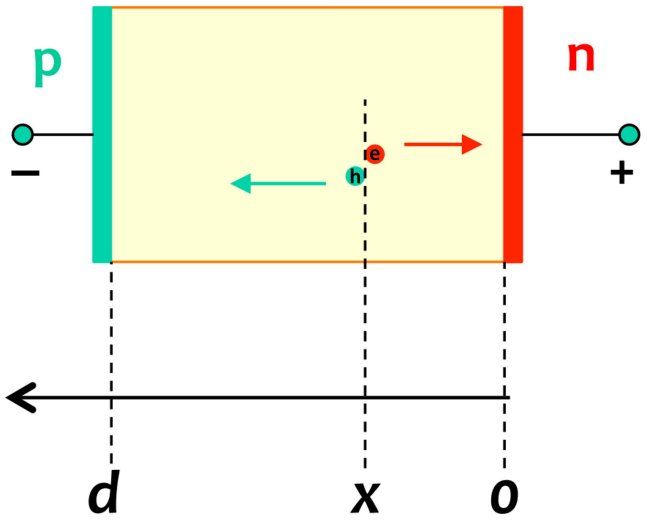

Fig. 3.6 Scheme of a parallel plate p-n junction. An electron hole pair is generated at a distance x from the positive electrode (n).

calculations is different for electrons and holes and are equal to:

$$t_e = \frac{x}{v_e} = \frac{xd}{\mu_e V_b}, \; t_h = \frac{x}{v_e} = \frac{d(d-x)}{\mu_h V_b}. \tag{3.11}$$

The ratio between the two charge collection times is:

$$\frac{t_e}{t_h} = \frac{x}{(d-x)} \frac{\mu_h}{\mu_e}, \tag{3.12}$$

this quantity clearly show that the differences on the charge collection time of the two charge carriers arises for two reasons: the different mobility of electrons and holes and the different distances which the two carriers have to travel before reach the electrodes. This difference leads to a variation of the induced current signal depending on where the charges are generated, as shown in Figure 3.7 The results obtained from this simplified model beside explain the signal formation in a silicon sensor, also show that the current of a detector changes according on the charge generation position but also depending on the mobility of the charge carriers. This shape variation, as reported in the following, is a limiting factor of a silicon sensor time resolution.

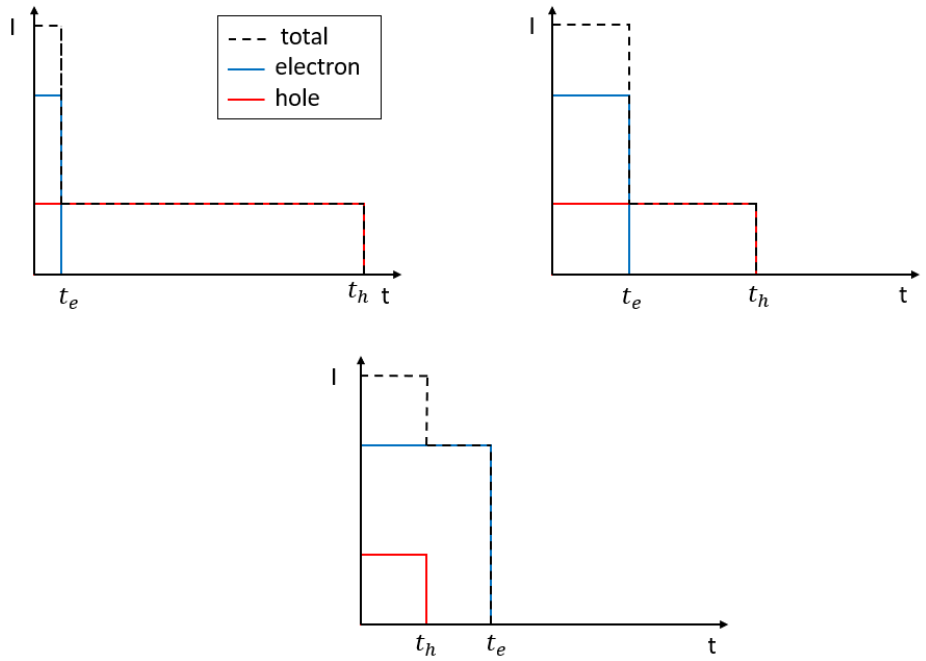

Fig. 3.7 Qualitative scheme of the current variation for the considered simplified model for different charge generation position x, the black line is the total current, in blue the electron current and in red the hole current currents. (Top left) $x \sim 0$, (Top right) $x \sim d/2$ and (Bottom) $x \sim d$.

3.4 Pixel sensors for tracking detectors

Silicon pixel sensors are position sensitive detectors. Thanks to their small dimensions, a pixel is capable to measure with high accuracy the spatial coordinates of a particle in a precise time instant. The detection of a particle by a pixel is called hit and by means of several planes of pixel sensors it is possible to reconstruct the track of a particle during its motion, as the scheme of Figure 3.8 shows. The spatial resolution of

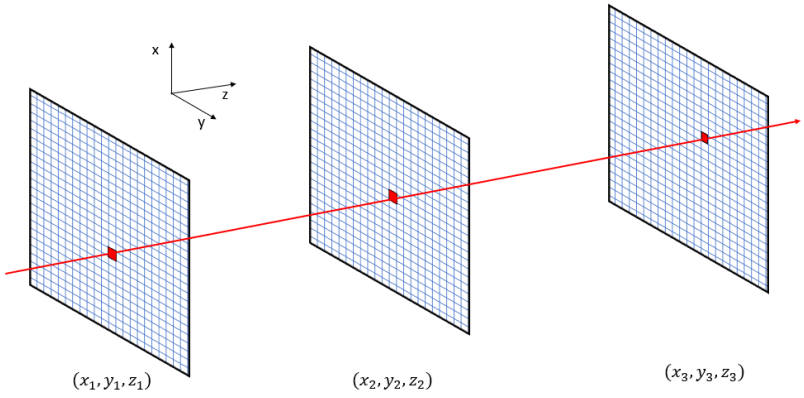

Fig. 3.8 Scheme of a pixel tracking detector. Three planes made of pixels sensors allow to reconstruct the track of a particle by reconstructing the straight line that intercepts the three hitted pixels shown in red.

a squared pixel, along the x-y, according to the x-y-z axis reported in Figure 3.8, is:

$$\sigma_{x,y} = \frac{d}{\sqrt{12}} \tag{3.13}$$

which is obtained by considering a flat probability for the hit position inside the pixel pitch d and no charge sharing between adjacent pixels. Silicon pixel sensors can be identified in two main categories: the hybrid pixels and the monolithic ones. Monolithic pixels contain, in a single silicon wafer, both the sensors and the electronic read-out, while hybrid pixels are silicon pixels sensors that to be operated must be connected to a chip containing the read-out electronics. The connections between the pixels and their front end electronic chip are typically made by means of bump-bondings, as shown in Figure 3.9. Both types of pixels have their advantages and disadvantages, for example monolithic sensors can achieve higher spatial resolution of few microns unlike hybrid pixels whose typical spatial resolution is $\mathcal{O}(10\,\mu\text{m})$. Moreover monolithic pixels are typically used for large area coverage since they are less expensive than hybrid detectors. However an important limit of current monolithic technologies is the lower

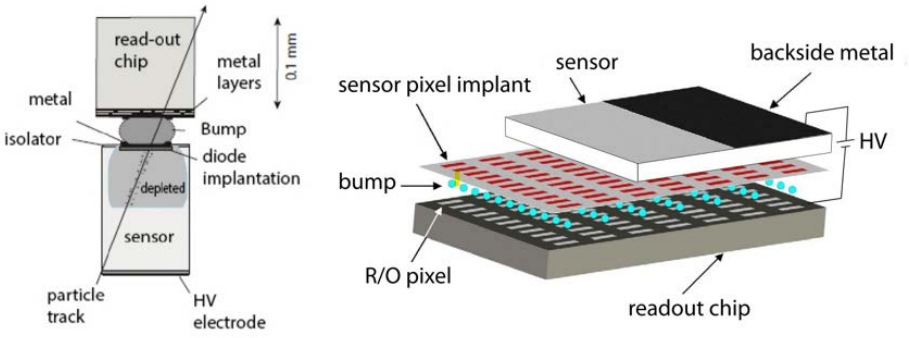

Fig. 3.9 Scheme of an hybrid pixel. (Left) a single pixel connected to the read-out channel by means of a bump bonding. (Right) A matrix of pixels bump-bonded to a read-out chip.

radiation hardness with respect to hybrid pixels. Because of this, tracker detectors placed near to primary vertices are typically made of hybrid pixels.

3.5 Radiation damage

Silicon pixel sensors of high energy physics tracking detectors are typically placed as near as possible to the colliders interaction point. These devices must survive for long periods of time in a very harsh radiation environment maintaining high standard of performances during their operations. Silicon sensors can be affected by the ionizing radiation by means of two type of damages: the bulk damages and the surface damages. Surface damages are caused by ionization process at the insulator surface of pixels and in the silicon-oxide interfaces, since they are related to interface zones they mostly affect the inter-pixel properties of a silicon detector. Bulk damages instead, are caused by a particle nucleus interaction that causes the displacement of some atoms in the lattice. The atoms displacements can affect the operation of a silicon pixel sensor in different ways. Moreover the damage is different for different kind of radiations and also for different energies of the radiation. To overcome this, usually the damage caused by different type of radiation is normalized to the one of a 1 MeV neutron equivalent fluence $1\,MeV\,n_{eq}\,cm^{-2}$. The main effects of the bulk damages is the formation of new energy levels in the forbidden energy gap which, depending on where are located, affects differently the sensor operation [39]. The leakage current of irradiated sensors normalized to the volume $\Delta I/V$ increases proportionally to the 1 MeV neutron equivalent fluence Φ_{eq}, as shown in Figure 3.10(left) [6]. Moreover a variation in the sensor depletion voltage is observed for irradiated sensors, as reported in

Figure 3.10(right) [6, 7]. This behaviour is explained by the variation of effective doping concentration caused by a donor removal together with an increase of acceptor-like energy levels that for high enough fluences lead to an inversion of the sign of the majority charge carriers, that is called type inversion. The last variation in the operation of the silicon detector is a reduction of the total charges capable to induce a current at the electrodes, referred as charge collection efficiency loss; this variation became significant for silicon detectors irradiated at fluences higher than $10^{15}\,1\,MeV\,n_{eq}cm^{-2}$[39]. This phenomena is related to the probability of the charge carriers to be trapped in new energy levels created in the forbidden energy gap after the nucelus dislocation. The measurements reported in [43] show that by reducing the inter-electrode distance of the sensors the loss in the charge collection efficiency of irradiated sensors is also reduced. The silicon pixel sensors with the highest radiation hardness ever tested are 3D sensors which have proven to survive to fluence higher than $10^{17}\,1\,MeV\,n_{eq}cm^{-2}$ [28], thanks to their very short inter-electrode distance.

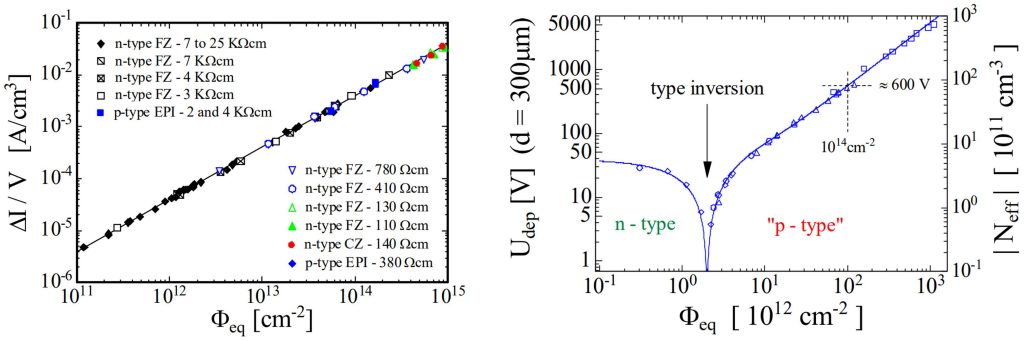

Fig. 3.10 (Left) Leakage current per unit of volume as a function of the irradiation fluence, taken from [6]. (Right) Full depletion voltage as a function of the irradiation fluence; image taken from [6, 7].

3.6 Time Resolution

The time resolution of a silicon sensor connected to its front-end amplifier and to a Time to Digital Converter (TDC) it is described as the squared sum of various independent contribution:

$$\sigma_t = \sqrt{\sigma_{un}^2 + \sigma_{ej}^2 + \sigma_{TW}^2 + \sigma_{Landau}^2 + \sigma_{TDC}^2}. \tag{3.14}$$

Several different contribution affect the overall time resolution of a silicon detector, each of them related to different mechanism. A deep understanding of each contribution is

fundamental to develop sensors with unmatched time resolution. With the exception of σ_{TDC}, which is the time jitter due to the digitization of the time measurement, the other therms of Equation 3.14 can be a major or minor contribution depending on the sensor technology and they must be taken into account to model a sensor with enhanced timing performances.

3.6.1 Non-uniformity jitter

The σ_{un} component is the time jitter due to a shape variation of the sensors current depending on the impact position of the particle to be detected and thus the positions in which the e-h pairs formation occurs. This shape variation, explained in Section 3.3, could be enhanced by inhomogeneous electric and weighting field which lead to higher shape variation of the current signals and thus to a higher time jitter. This component represents the intrinsic time resolution of 3D silicon sensors. Planar sensors, with or without gain, are less affected by this contribution since a variation in the particle impact position do not affect the charge collection process, which for planar sensors is related to the sensor thickness. Detailed measurements of this jitter contribution for different 3D sensors are reported in Section 6.4.2 and 6.5.

3.6.2 Electronic noise jitter

The electronic noise jitter σ_{ej} is the jitter component due to the voltage noise of the signals. As Figure 3.11 shows, the amplitude noise causes a time fluctuation. It can be

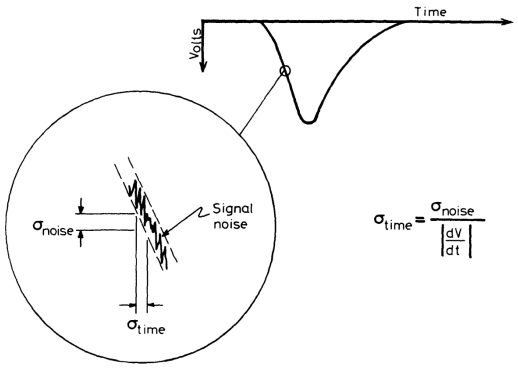

Fig. 3.11 Scheme for the noise jitter. The noise of a signal cause a time fluctuation that is called electronic jitter [8].

expressed as:

$$\sigma_{ej} = \frac{\sigma_V}{|\frac{dV}{dt}|} \sim \frac{\sigma_V t_r}{S}, \tag{3.15}$$

where σ_V is the amplitude noise, $|\frac{dV}{dt}|$ is the signal slope, t_r is the rise time of the signal and S is the signal amplitude. According to Equation 3.15 the key ingredients to reduce the electronic jitter are high signal to noise ratio and fast rise times. This jitter is related to both the sensors and their front-end electronics. All the R&D for the developments of sensors with enhanced timing performances are searching for technological solutions which allow to increase the signal and to have faster charge collection times. For example planar sensors with gain, like the hybrid Low Gain Avalanche Detector (LGAD) [44] and the monolithic Picosecond Avalanche Detector (PicoAD) [11], exploit the fast charge collection time of thin silicon sensor and increase the signal amplitude by means of the addition of a gain layer. 3D silicon sensor instead, achieves fast charge collection time thanks to short inter-electrode distance made without reducing the sensor thickness and thus without loosing signal amplitude [45]. Historically this was the dominant jitter contribution of a silicon detector, however the increasing performances of both sensors and electronics amplifier, with higher SNR and rise times equal, or even lower, to the charge collection times allowed to reduce this noise contribution [46, 47]. However the noise jitter is still the dominant contribution for the applications in which a low power consumption of the electronics is needed, such as the vertex detectors.

3.6.3 Time-walk jitter

The time-walk jitter σ_{TW} is originated by the variations on the signal amplitude. In fact, two signals of different pulse height but exactly coincident in time will trigger a fixed amplitude threshold at two different times, as Figure 3.12 shows. The time-walk effect depends on the method used to measure the time of a signal. Typically this jitter component is made negligible by means of a constant fraction discriminators (CFD), which instead of triggering on a constant threshold it triggers on a constant fraction of the signal. Another solution is to correct the measured time with an amplitude dependent method so that the time dependence on the amplitude is removed. This contribution have a higher impact on thin silicon sensors since they are subjected to higher amplitude fluctuations. However, the time-walk jitter typically became negligible when amplitude or time over threshold corrections methods are used.

3.6.4 Landau fluctuation jitter

The stochastic process of the energy deposition can also cause signal shape variation. This is true in particular for planar sensors in which the charge collection occurs in the

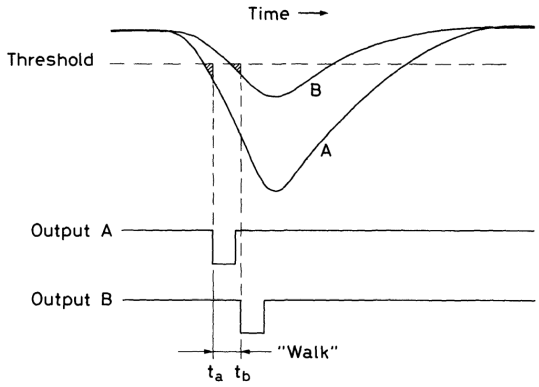

Fig. 3.12 Scheme for the time-walk effect. Two sychronous signals with different amplitude exceed a fixed threshold at different times [8].

same direction of the energy deposit profile. The current shape variation of a silicon sensor was already considered, for a single e-h pair in Section 3.3, according to that, if the free charge carriers profile along the inter-electrode distance changes a current shape variation is expected. For example the simulations reported in Figure 3.13, taken from [9] show that two different charge carriers profiles along the sensor thickness of a planar sensor lead to two different currents. This signal shape variation causes a time jitter called landau jitter σ_{Landau}. This contribution represents the intrinsic limit of the time resolution of a planar sensor with or without gain and, to reduce this jitter, it is possible to reduce the sensor thickness. 3D sensors, thanks to their very short inter-electrode distance and because the charge collection occurs orthogonally to the particles path are less affected by this type of jitter.

3.7 Timing silicon detectors: state of the art

In this section the state of the art of silicon pixel sensors with enhanced timing performances is reported.

3.7.1 3D sensors

3D sensors are silicon pixel sensors with the electrodes directly built into the sensor thickness. This feature allows to develop sensors with a very short inter-electrode distance with respect to standard planar sensors without reducing the active material in which the crossing particles can create e-h pairs, as shown in Figure 3.14. This allows to exploit short inter-electrodes distances without loosing signal amplitude. One

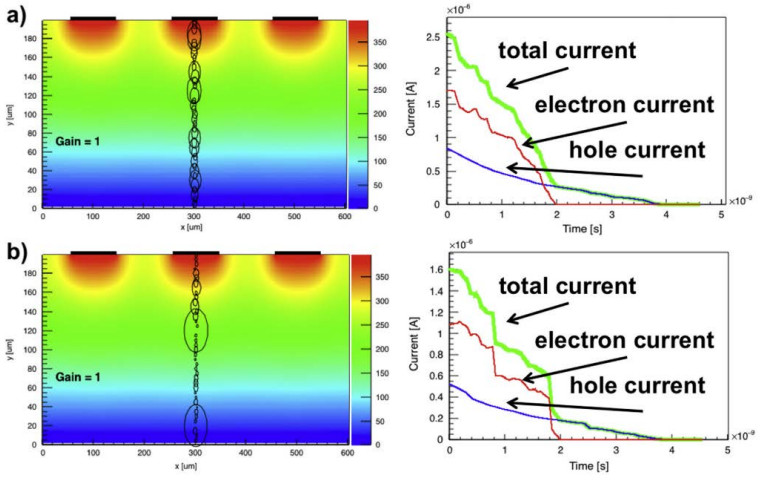

Fig. 3.13 Simulation of two different charge depositions in a planar silicon sensor with a thickness of 200 μm. The two charge deposition lead to different current shapes. Picture taken from [9].

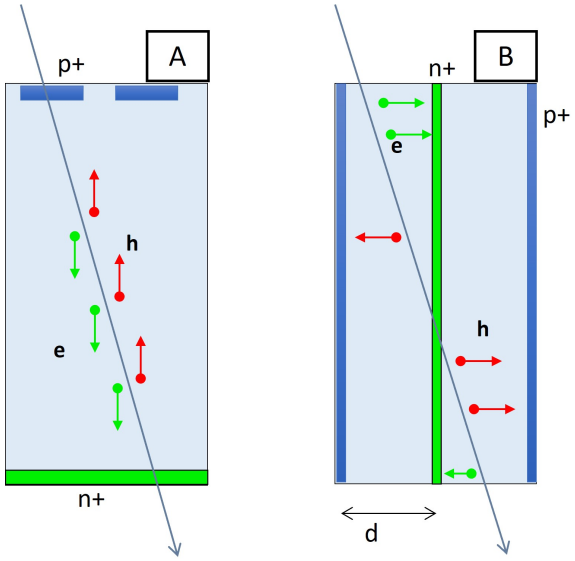

Fig. 3.14 Comparison of the charge collection process between a planar sensor (A) and a 3D sensor (B).

of the main features of 3D sensors are the extremely fast signals, given by the shorter path travelled by the charge carriers before being collected by the electrodes. Moreover, higher electric fields and thus charge carriers mobility saturation are obtained with a lower bias voltage. Another important advantage of sensors with short inter-electrode distance is a high radiation hardness, that for a columnar 3D silicon sensor was tested up to $1 \cdot 10^{17}\, 1\, MeV\, n_{eq}\, cm^{-2}$ [28]. These two characteristics lead 3D sensors to be one of the most suitable sensors for the tracking detectors of HL-LHC experiments and beyond.

The first 3D sensors were proposed by Sherwood Parker [45] with a columnar electrode layout. However, for 3D sensors it is possible to make electrodes with different shapes and layout, since the electrodes are built through the sensor thickness. The TimeSPOT project by means of accurate simulation studies, developed a 3D silicon sensor optimized for timing applications. In fact, albeit the 3D sensors timing performances are expected to be good due to the short inter-electrode distance, achieved without decreasing the sensor thickness, this type of sensors have a limit in their intrinsic time resolution that is represented by the non-uniformity jitter contribution. This contribution, related to the variation on the impact position of the particles, is higher for non-planar electrodes geometries since they lead to inhomogeneous electric and weighting fields. According to the Ramo theorem, reported in Equation 3.5 uniform weighting field and charge carriers drift velocities inside the sensor volume should guarantee more uniform sensors currents. From this simple concept the TimeSPOT collaboration developed an innovative 3D sensor with planar-like electrodes, the 3D trench sensors. Figure 3.15 shows TCAD simulations of a traditional 3D sensors with a 5 columns electrodes layout compared to the innovative 3D trench sensor. The maps show that 3D trench sensor have much more homogeneous weighting field and electric field in the sensor active volume. The resulting charge collection curves obtained from a transient simulation [10] for MIP that uniformly cross the pixels sensitive area are reported in Figure 3.16. The curves show that the 3D trench sensor provide shorter and much more uniform charge collection times than the 5 columns geometry. The 3D trench pixels have a typical dimension of 55×55 μm^2 which grants a spatial resolution in the order of 15μm. In this thesis accurate characterizations of the 3D trench sensors are shown proving their excellent radiation hardness and time resolution.

3.7.2 Planar sensors with gain

The gain in silicon pixel sensors have been added to improve the time resolution of standard planar pixels [48], for which the best time resolution achieved is 115 ps by

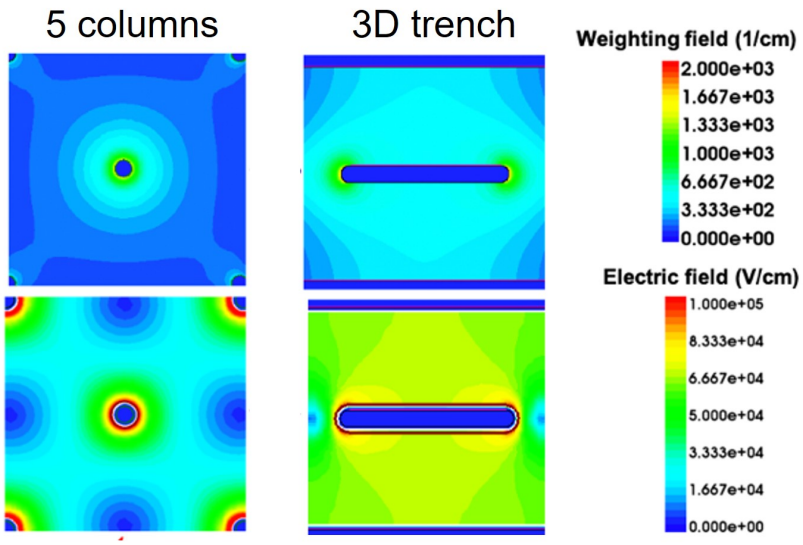

Fig. 3.15 TCAD simulations of the weighting field and the electric field of a 3D sensor with a 5 columns electrodes layout (left) and for the TimeSPOT 3D trench sensor (right). Simulations made for -150 V bias voltage.

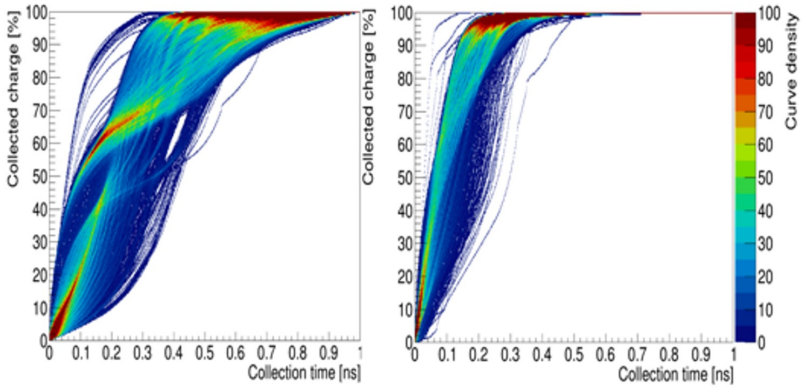

Fig. 3.16 Simulations of charge collection curves for MIPs uniform incidence for the five columns geometry (left) and for the trench geometry (right) [10] .

the planar sensors developed for the GigaTracKer of the NA62 experiment [49]. The addition of a gain layer allows to cope the reduction in signal amplitude of thin planar sensors and thus allows to fully exploit the benefits, in terms of timing performances, of sensors with smaller inter-electrode distances.

The state of the art of silicon pixels with gain are the hybrid Low Gain Avalanche Detector (LGAD) and the monolithic Picosecond Avalanche Detector (PicoAD). The LGAD is a planar silicon pixel sensor in which a thin p-type layer is diffused just below the n^+ electrode, as shown in Figure 3.17. The insertion of the p-type layer allows to

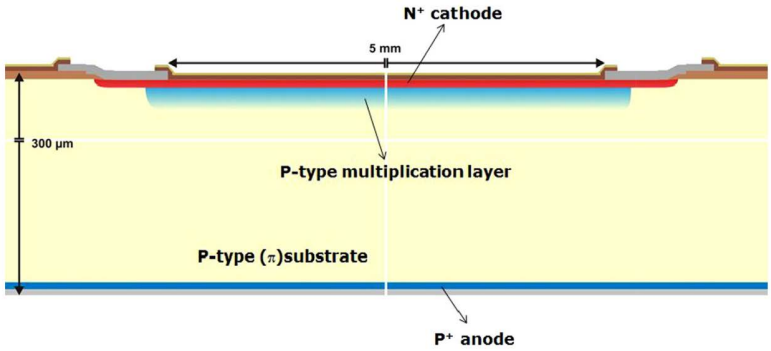

Fig. 3.17 Scheme of a Low Gain Avalanche Detector. The insertion of a p^+ layer under the n layer allows electron multiplication.

create a $n^+/p/p^-$ junction which for reverse bias voltage operation, originates a high electric field in this region. If the field is high enough a multiplication of the electrons approaching the n^+ electrode occurs. A typical gain of $10 \div 15$ are obtained with these devices under standard bias voltage operation. The timing characterizations of these devices [50], show a time resolution of about 30 ps and 25 ps for 50 μm and 35 μm thick sensor respectively, both results are dominated by the σ_{Landau} jitter.

The main issue of these detectors for HL-LHC tracking purposes near to the interaction vertices is the gain degradation at high irradiation fluences. Recent studies have been shown that LGAD totally lose the gain factor when irradiated at fluences higher than $2 \cdot 10^{15}\, 1\, MeV\, n_{eq}\, cm^{-2}$ [51]. However a new R&D aimed to improve the radiation hardness of these devices is ongoing [52].

The monolithic Picosecond Avalanche Detector (PicoAD) is a multi-junction silicon pixel sensor developed in the framework of the H2020 ERC Advanced MONOLITH project. This development aims to improve the time resolution of monolithic pixels by exploiting a gain mechanism to increase the signal to noise ratio of these devices combined with the usage of fast SiGe BiCMOS electronics which allows to fully exploit the fast charge collection time. The main difference between LGAD and PicoAD

technologies is the higher design flexibility achieved by moving the gain layer away from the pixel readout matrix and separating the region where the primary charge is produced [11]. Figure 3.18 shows a cross section of the PicoAD sensor, three main regions can be identified to explain the working principle of this detector. The primary

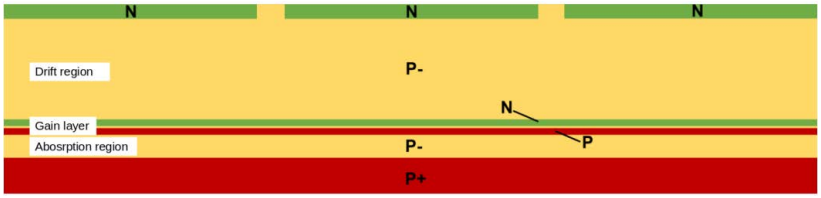

Fig. 3.18 Scheme of a PicoAD. A second junction, deep inside the sensor volume, is used as a gain layer to produce electrons avalanches [11].

absorption region, located near the backside contact, is the region in which the primary electrons are generated. The uniform and continuous deep np junction represents the gain layer. The thicker p^- zone is the drift region, in which the primary charges and the multiplied electrons drifts towards the readout electrode inducing the signal current. Placing the gain layer away from the readout electrodes allows to make smaller pixel and thus to achieve better spatial resolution than LGAD sensors but also to reduce the σ_{Landau} jitter by decreasing the thickness of the absorption region, which, differently to LGAD sensors, is done without increasing the detector capacitance. First characterizations of PicoAD sensors have shown a maximum gain achieved of about 23 [53]. A beam test campaign have proven a time resolution of 17 ps and a detection efficiency of 99.9% for 100 μm pitch PicoAD pixels [54]. This innovative technology appears very promising but, more studies on the radiation hardness must be done in order to consider this sensor as a good candidate for the HL-LHC tracking detectors.

Chapter 4

First TimeSPOT sensors batch beam test characterization

This chapter summarize the first beam test characterization of the 3D trench silicon sensors. The results obtained, even if dominated by the electronic noise contribution and, as shown in the following, limited by the sensor structure, represent a world record result in terms of the time resolution of silicon sensors for MIP (Minimum Ionizing Particle) detection [55].

4.1 Test structure

The devices tested are 3D trench double pixel structures made in the first TimeSPOT batch by Fondazione Bruno Kessler (FBK), in Trento. This kind of sensor consists of two adjacent TimeSPOT 3D trench pixels which have the n++ readout electrodes shorted to the same metalization pad. An image of the sensor is shown in Figure 4.1, the tested device is circled in red.

Each structure is attached with a conductive tape to a printed circuit board (PCB) containing the discrete-components front-end electronics. The sensor readout electrodes are wire bonded to the input of the amplifier, as reported in Figure 4.2. The bias voltage is provided to the sensor from the back contact through the pad where they are attached. The 3D sensors are operated at room temperature.

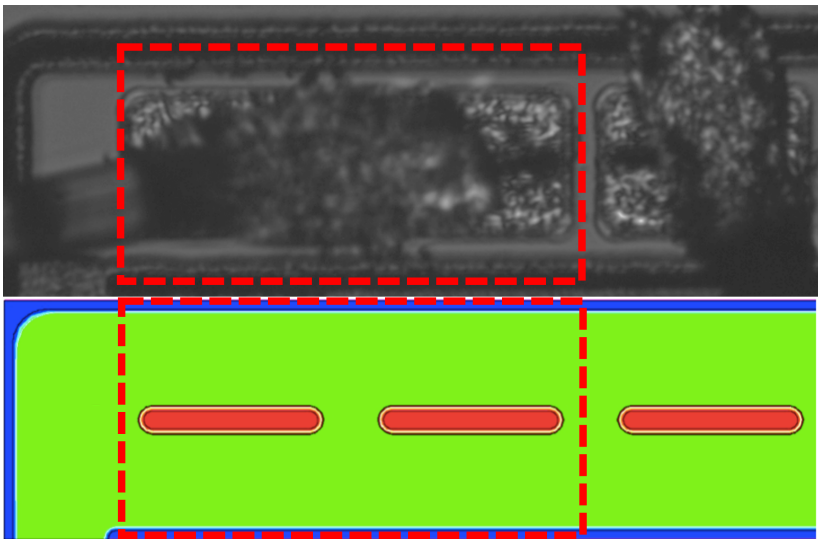

Fig. 4.1 3D trench double pixel structure: (top) picture of the tested device, (bottom) scheme of the test structure. The double pixel is inside the red box.

4.2 Front-end electronic board

The sensor readout is based on a two-stage signal amplification scheme acting as an inverting transimpedance amplifier, implemented on a custom-made circuit. The first amplification stage is performed by an AC-coupled silicon-germanium bipolar transistor designed for high bandwidth (up to 5 GHz) and low noise applications, featuring a gain of nearly 30 dB at 2 GHz and an integrated output noise of 260 μV. The design is optimised for sensors with capacitance $\mathcal{O}$(10 pF), producing signals with charge $\mathcal{O}$(10 fC) and a rise time of about 200 ps. These characteristics does not fully match those of the 3D trench sensors which have a capacitance of $\mathcal{O}$(100 fF), producing a charge of 2 fC with a very short charge collection time, less than 100 ps. This, as will be discussed in the following, will be the limiting factor of the measured time resolution. Despite these are rather different values, the board, shown in Figure 4.2, has proved to perform satisfactorily on the signals produced by this innovative sensors.

The PCB design has been optimised for small and fast signals by minimising all parasitic capacitance and inductance sources, choosing very small size components, and ground-burying all signal and power lines whenever possible. Protection from external electromagnetic noise is ensured by hermetic metal shields. The second stage consists of a current amplifier, designed for fast signals. It is based on a monolithic wideband amplifier, with 2 GHz bandwidth, and provides a 20 dB gain factor.

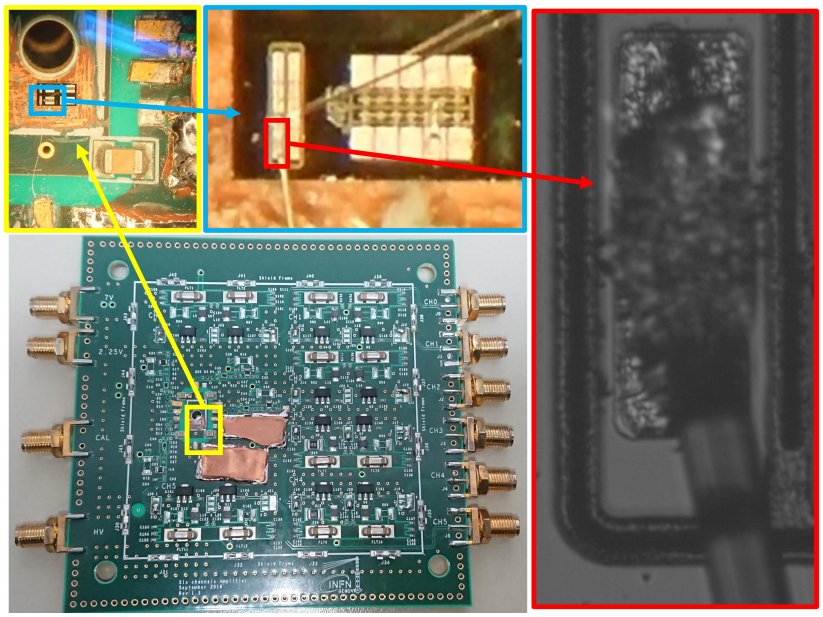

Fig. 4.2 The six-channels front-end board used for the first stage signal amplification. The amplifier connected to the double pixel is located underneath the copper shielding. The tested 3D trench silicon sensor is in the right picture.

4.3 Setup

The time resolution of 3D trench silicon sensors was measured for the first time in October 2019 at the PSI πM1 beamline with 270 MeV/c positive pions, which in silicon produce an energy deposit only slightly larger ($\sim 5\%$) than those from minimum ionising particles (MIPs). The reference measurement of the pion arrival time is provided by two Cherenkov detectors. Each of them consists of a 20 mm thick quartz radiator attached by means of an optical silicon to a large area (53 mm $\times$ 53 mm) active window micro-channel plate photomultiplier tubes (MCP-PMT) [56]. Both the MCP-PMTs and the PCB with the 3D trench silicon sensors are mounted inside a light-tight box positioned on the pion beamline, as shown in Figure 4.3. The silicon sensors are located upstream of the two MCP-PMTs and are transversely aligned with each other with a 1 mm accuracy. The pions crosses all detectors at normal incidence and provide a uniform illumination of the 3D sensor.

4.4 Data acquisition

The signal waveforms from 3D sensor and the MCP-PMTs detectors are acquired by means of a 8 GHz analogue bandwidth, 20 GSa/s, 4-channels digital oscilloscope,

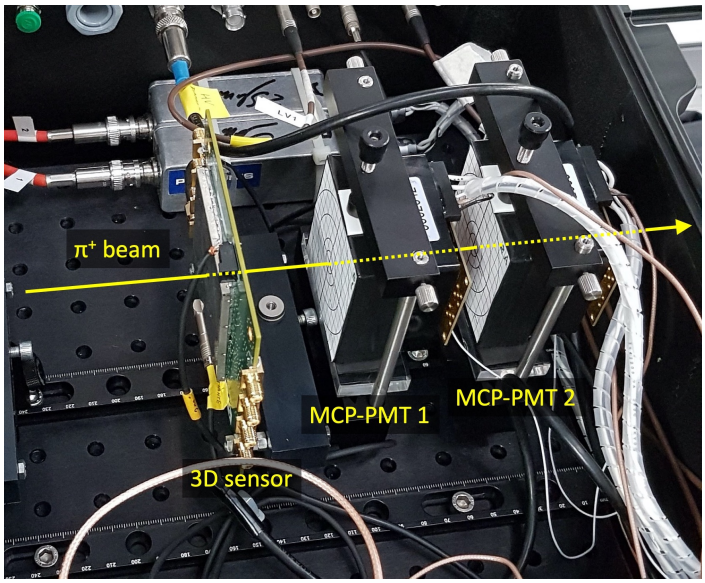

Fig. 4.3 Picture of the detector setup used during the beam test at PSI. A 3D trench silicon sensor on the front-end electronic board and the two MCP-PMTs used to provide the time reference are visible in the picture.

the Rhode&Schwartz RTP084. The silicon sensor and the MCP-PMTs are connected to the oscilloscope by means of 10 m-long low-loss coaxial cables. The oscilloscope trigger condition required a signal from the 3D trench silicon sensor in coincidence with signals from both the MCP-PMTs. The trigger thresholds on signals is adjusted to allow an efficient noise rejection while keeping most of the events, typical events are shown in Figure 4.4. At 270 MeV/c the PSI πM1 positive beam has a momentum resolution of 0.1% and a transverse size of approximately $40mm \times 40mm$ full-width at half-maximum (FWHM) at the focal point where the sensor are located. The beam is mostly composed by pions, with a small contamination of positive muons, positrons and protons. Since only a small fraction of the particles crossed both the 3D trench silicon sensor and the two MCP-PMTs, the beam intensity is adjusted, by means of collimators, to achieve a data acquisition trigger rate of the order of 100 Hz. One channel of the oscilloscope is used to record the radio-frequency signal coming from the PSI Ring Cyclotron (RF) and was used to further improve the pion beam purity by selecting a proper delay between the MCP-PMTs signals and the phase of the RF, implementing an effective Time-of-Flight (TOF) detector. Samples of 20000 events (3000 at Vbias = 80 V) are recorded for different sensor reverse bias voltages and oscilloscope trigger thresholds.

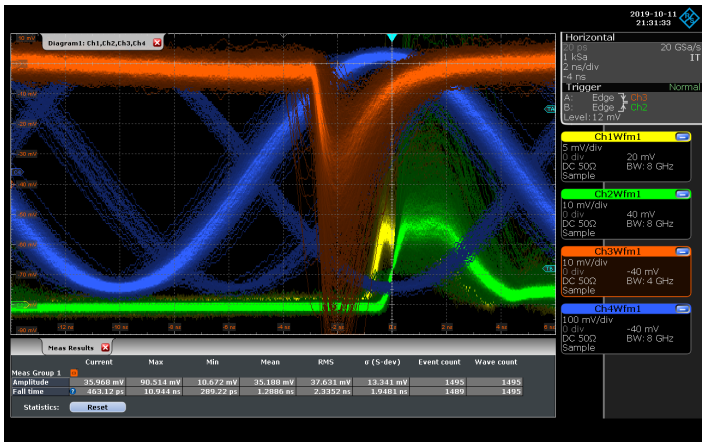

Fig. 4.4 Waveforms acquired with the oscilloscope. The yellow and green waveforms are the reference signals from the MCP-PMTs, the red waveform is the signal from the 3D trench silicon sensor and the blue waveform is the radio-frequency from the PSI Ring Cyclotron. The three different RF phases correspond to the various components of the beam.

4.5 Data analysis

The waveforms analysis has the main purpose of determining the time resolution of the 3D trench silicon sensor. To take into account the attenuation of the 10 m low-loss coaxial cable used during the data acquisition, the cable's transfer function, measured in laboratory, is deconvoluted from the 3D trench silicon sensor's waveforms. Figure 4.5 shows the average shape of the two MCP-PMTs and the 3D trench silicon sensor waveforms. The typical rise time values (20–80% of the signal) are 370, 490 and 200 ps, respectively. The signal amplitude (A) is given by the maximum value of the waveform, corrected by evaluating the baseline just before the beginning of the sensor signal, as reported in Figure 4.6. The time of each sensor signal is determined by means of three different methods. The first one is the amplitude and rise time-compensated (ARC) method [57], referred as reference in the following, in which from each waveform an identical contribution delayed by about half of the signal's rise time is subtracted. The resulting waveform, showing a peaking structure, is fitted with a Gaussian function to determine the amplitude as Figure 4.6 reports (black line). The time of each waveform is set as the value corresponding to 50% of the Gaussian's amplitude, by linearly interpolating the signal rising edge (red line of Figure 4.6).

The second method, the PSI method, is a Constant Fraction Discriminator (CFD) based method, initially employed for the waveforms analysis. In this method the time of each waveform is set as the value corresponding to 35% of the signal's maximum

amplitude and is calculated from a linear interpolation of the signal's 20-80 % rising edge. The last method, the leading edge, follows the simplest possible approach. The signal time is defined as the value at which the amplitude exceeds a fixed threshold, also this method includes a linear interpolation of the waveform in the range of ±40 ps around the threshold.

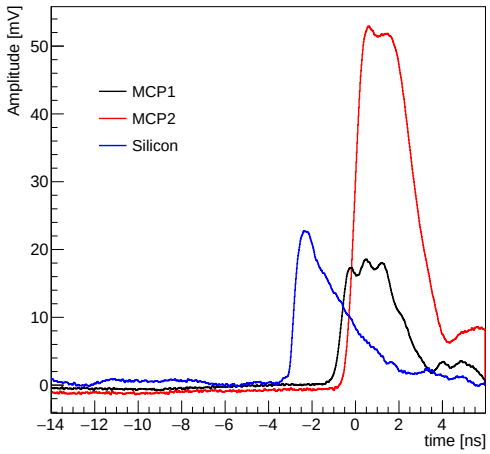

Fig. 4.5 Average waveforms of the (black) MCP-PMT1, (red) MCP-PMT2 and (blue) silicon sensor. The 3D trench silicon sensor signal is reversed. The waveforms correspond to the average of fifty signals.

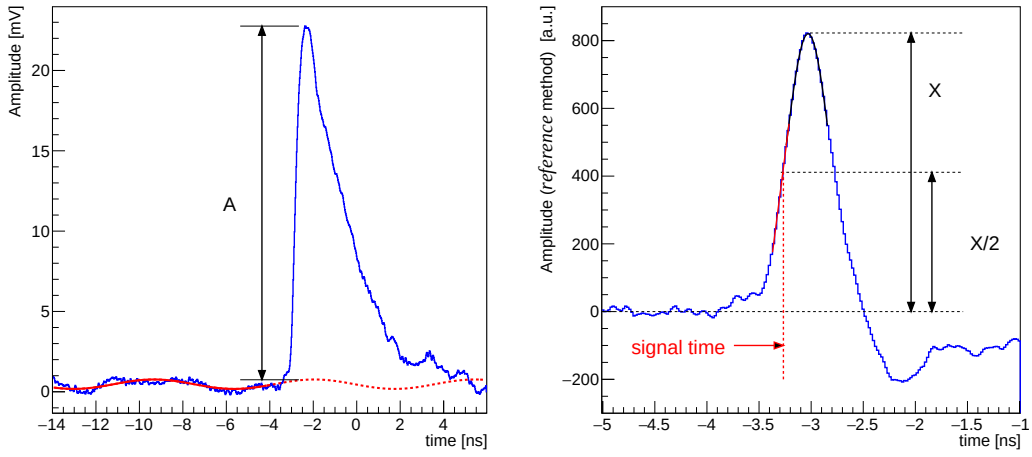

Fig. 4.6 (Left) Average 3D trench silicon sensor waveform and (right) resulting waveform after the reference method is applied. Arrows and functions illustrate how the signal amplitude and the time are determined.

4.6 Results

The signal amplitude distribution of the silicon sensor, corresponding to a sensor bias of -140 V, is shown in Figure 4.7. It follows a Landau distribution convoluted with a Gaussian down to the smallest amplitudes, indicating that the trigger threshold does not bias the amplitude distribution of the minimum ionising particles signals. Moreover, the most probable value and the width of the Landau scale as expected for the energy deposit of a MIP in 150 μm of silicon [58], providing an important cross-check of the proper operation of the 3D trench silicon sensor.

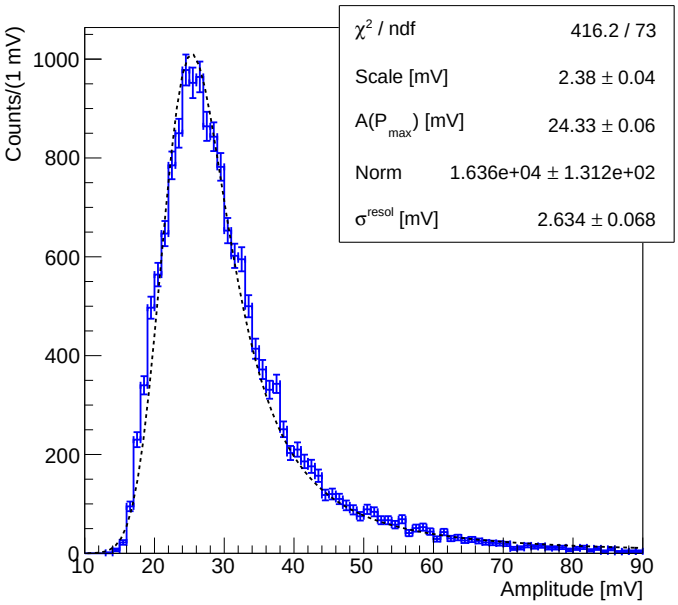

Fig. 4.7 Distribution of the signal amplitudes for the silicon sensor. The superimposed blue curve is the result of a fit to a Landau distribution convoluted with a Gaussian. Fit parameters are shown in the legends.

The time resolution of the 3D trench silicon sensor was evaluated from the waveform analysis. The delay of the sensor's signal with respect to the pion arrival time was measured using the reference method. The pion arrival time was given by the average time of the two MCP-PMTs signals, $\langle t_{\mathrm{MCP-PMT}} \rangle$. Its accuracy is computed from the width of the distribution of their time difference, $t_{MCP-PMT1} - t_{MCP-PMT2}$, shown in Figure 4.8 (left),which has a resolution $\sigma_{\Delta_t} = 24.8 \pm 0.2$ ps and resulting in a pion arrival timing accuracy of about 12.5 ps when the time information of the two

MCP-PMTs are averaged, as Equation 4.1 shows:

$$\sigma_{\langle t_{MCP-PMTs}\rangle} = \frac{1}{2}\sqrt{\sigma^2_{t,MCP-PMT_1} + \sigma^2_{t,MCP-PMT_2}} = \frac{1}{2}\sigma_{\Delta_t}, \tag{4.1}$$

where $\sigma_{t,MCP-PMT_i}$ is the time jitter of the i-th MCP-PMT.

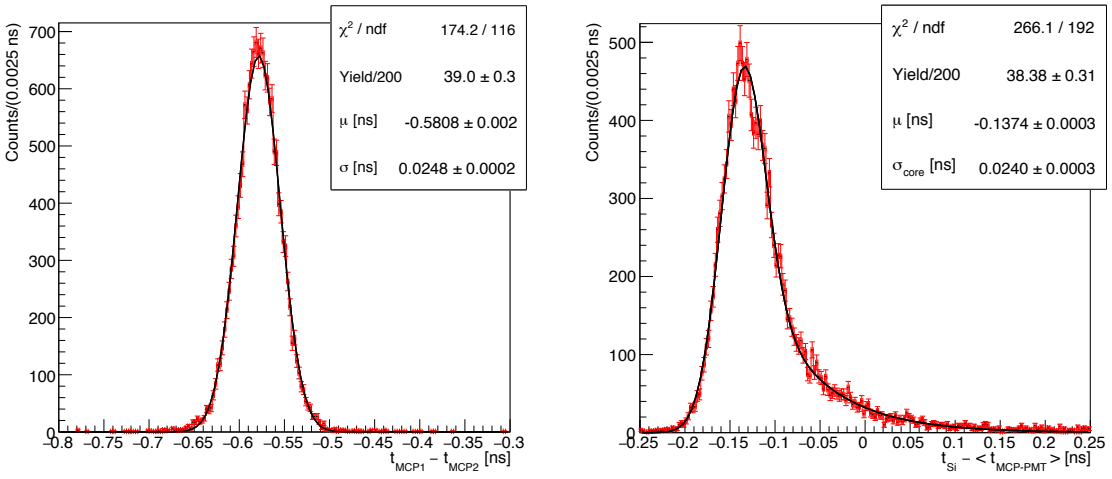

Fig. 4.8 (Left) Distribution of the time difference between the two MCP-PMTs with a Gaussian fit overlaid. (Right) Distribution of the time difference between the 3D trench silicon sensor and the pion arrival time with the result of the fit overlaid.

Figure 4.8 (right) shows the distribution of the time difference between the 3D trench sensor signal and the pion arrival time, $t_{\mathrm{Si}} - \langle t_{\mathrm{MCP-PMT}}\rangle$. The distribution has a dominant peaking structure with a Gaussian core of $\sigma_{\mathrm{core}} = 24.0 \pm 0.3$ ps and an exponential tail of late signals, unexpected in its long duration and that is analyzed in detail in the next section. Assuming that the Gaussian core provides an estimate of the sensor performance and combining it with the pion arrival time uncertainty, the time resolution for the 3D trench silicon sensor is $\sigma_t^{\mathrm{Si}} = 20.6 \pm 0.4$ ps. The reference method provides the best results, however excellent time resolutions are obtained with the PSI method but also with the very simple leading edge algorithm, as Table 4.1 reports. The leading edge method results are below 35 ps and they are obtained without time-walk correction.

The results obtained with the various methods and as a function of the sensor bias voltage are shown in Figure 4.9. A mild dependence on the bias voltage is present, proving that high timing performance can be obtained even with low revere bias voltages.

Table 4.1 Average signal-to-noise ratio, noise, slew rate (dV/dt) and time resolution of the 3D trench silicon sensor for different values of the bias voltage and for different analysis methods. The values of the time resolution are subtracted by the pion time of arrival uncertainty. All results correspond to samples of 20 000 events, except for that at $V_{\text{bias}} = -80$ V, that contains 3 000 events.

setting	*reference*				*PSI*				*leading edge*
V_{bias} [V]	S/N	N [mV]	dV/dt [mV/ps]	σ_t^{Si} [ps]	S/N	N [mV]	dV/dt [mV/ps]	σ_t^{Si} [ps]	σ_t^{Si} [ps]
−20	12.2	2.22	0.097	24.2 ± 0.5	14.8	2.13	0.070	32.7 ± 0.7	46.4 ± 0.5
−50	13.0	2.24	0.114	21.9 ± 0.4	13.1	2.38	0.086	30.3 ± 0.4	37.6 ± 0.3
−80	13.3	2.26	0.121	22.7 ± 1.2	12.2	2.56	0.095	30.0 ± 1.1	34.2 ± 1.0
−110	13.6	2.26	0.125	20.9 ± 0.4	12.3	2.57	0.098	27.8 ± 0.4	34.7 ± 0.3
−140	13.9	2.25	0.128	20.6 ± 0.4	12.6	2.56	0.100	27.1 ± 0.4	35.3 ± 0.4

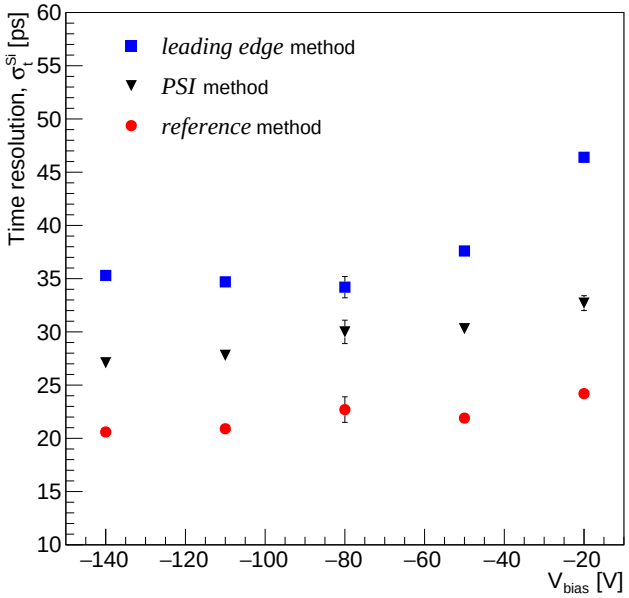

Fig. 4.9 Time resolution of the 3D trench silicon sensor, σ_t^{Si}, as a function of the sensor bias for different analysis methods considered. The contribution due to the pion ToA uncertainty is subtracted.

A rough estimate of the contribution of the electronic jitter to the time resolution can be computed from the average slew rate and noise as $\sigma_{\text{ej}} \sim \text{N}/(\text{dV}/\text{dt})$. Using the values in Table 4.1 the resulting σ_{ej} ranges from 18 to 20 ps giving a strong indication that the contribution due to the electronics noise is the dominant part of the measured time resolution.

4.7 Understanding the tail of late signals

The time resolution results, shown in the previous section, refers to the Gaussian core of the $t_{\text{Si}} - \langle t_{\text{MCP-PMT}} \rangle$ distributions. This approach does not include the contribution of the tail of late signals that the measured time distributions show. A long effort was spent in order to understand the origin of the tail, that was not foreseen by the sensor simulations [59]. The first step was to characterize the test structure with the laser setup, described in details in Chapter 6. The characterization consists of exciting the test structure with an infrared laser and measure its response throughout its active volume. Unfortunately the metallization pads cover almost the whole sensor top area, making impossible to completely characterize the test structure. However this double pixel test structure present a side region without the metallization pad. This region is not representative of a 3D trench pixel structure but, with a laser excitation in this region, it is found to be active. Figure 4.10 shows the recorded signals for different position of laser excitation.

The signals show an increasing ToA as the distance from the collection electrode increases. This measurement gave a first, qualitative, explanation of the tail origin: the tail is due to signals generated in a side area of the sensors. This first result opened the way to an accurate modelling of a 3D trench double pixel sensor [60]. The simulation is based on the combined use of several software tools (TCAD [61], GEANT4 [62], TCoDe [10] and TFBoost [63]) which allow to fully design and simulate the physics response of the detector in a very short computational time $\mathcal{O}(1 \div 100\,\text{s})$ per simulated signal, by exploiting parallel computation using single or multi-thread processors. This allowed to produce large samples of simulated signals, perform detailed studies of the sensor characteristics and make precise comparisons with the beam test results, a summary of all the steps of the modelling is presented in the following.

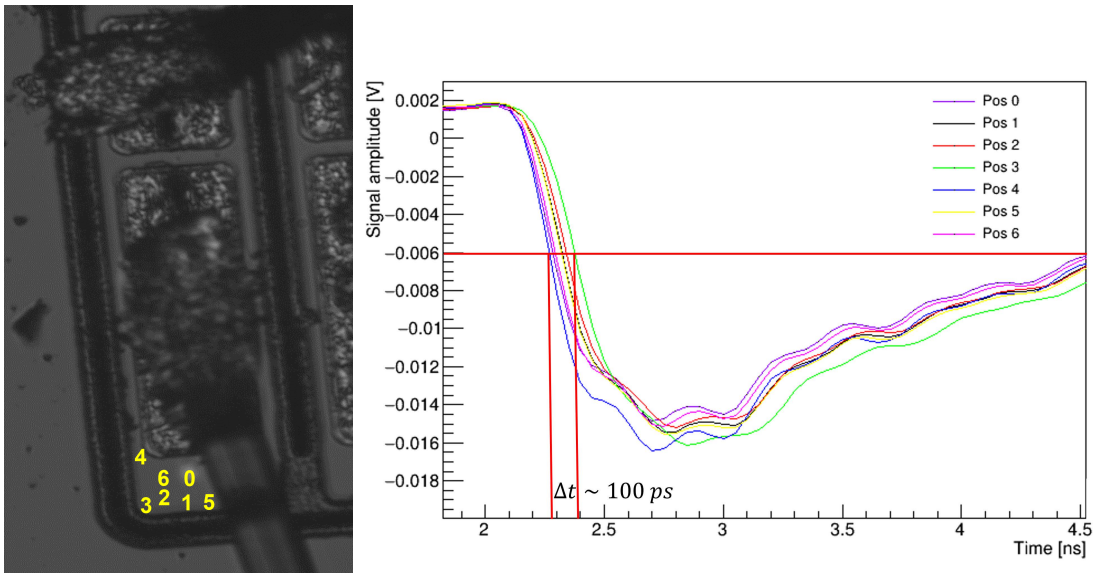

Fig. 4.10 (Left) Picture of the double pixel test structure under the laser setup. The yellow numbers represents different laser excitation positions. (Right) Signals recorded for the different excitation position, a time delay higher than 100 ps emerges from the signals.

4.7.1 Static modelling of 3D trench double pixel

The model designed for the simulation is an exact replica of the double-pixel device tested at PSI in 2019. It consists of two standard parallel trench pixels connected to the same readout electrode (referred to as double pixel) and a third neighbouring pixel, connected to ground, to better describe the boundary conditions of the active pixels (electric and weighting fields). The double pixel is located at the border of a test structure as shown in Figure 4.11

The sensor design and the simulation of its physical properties (electric and weighting fields, charge carrier mobility) is performed by using Synopsys Sentaurus TCAD package [61]. The model is simulated using a quasi-stationary voltage ramp from 0 V to −150 V. The relevant information at the bias voltages of −50 V, −100 V and −150 V are saved for the subsequent transient simulation. As Figure 4.12 shown, the simulated test structure presents an uniform electric field in the regions placed between the biases and readout electrodes. Areas with smaller electric field are located in the inter-pixel regions between the readout electrodes and in the active volume aside the rightmost pixel. The inter-pixel areas are not particularly critical for fast timing, thanks to the small drift path travelled by charge carriers to reach their collection electrodes and the higher weighting field, which implies stronger current induction. The region aside the

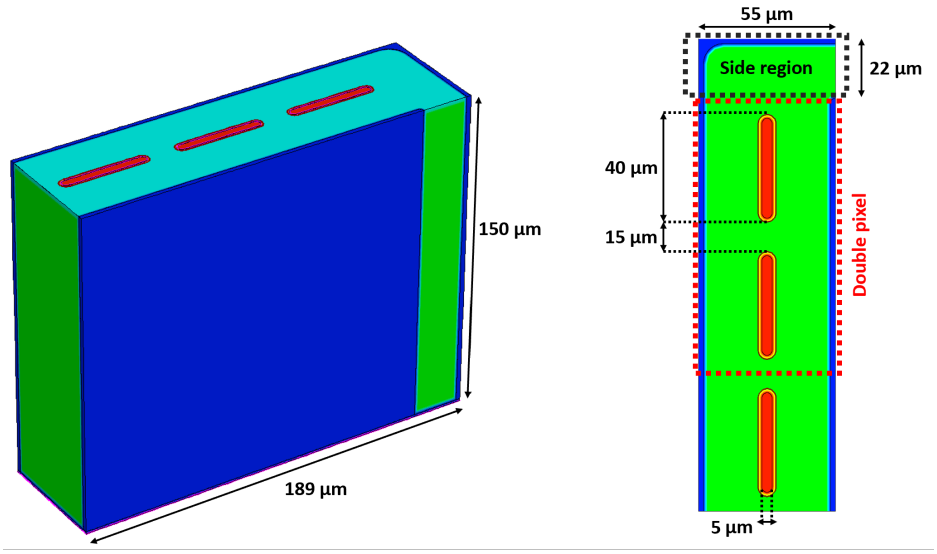

Fig. 4.11 Layout of the simulated TimeSPOT test structure, including sections and sizes, designed using Sentaurus TCAD. The double pixel is indicated by the dotted-red lines.

rightmost pixel (referred to as *side region* in the following) instead is the main critical region for the timing performances of this particular test structure. Larger distances from the electrodes and less uniform electric and weighting fields cause larger charge collection times and a more diversified current signal depending on the position.

4.7.2 Transient simulations

The transient simulations have the goal to simulate the events generations, from the energy deposition of the particles in the sensor, to the current induced by the sensors electrodes. Finally it combines the sensor currents to the front-end amplifier transfer function. These tasks are solved with different packages, in particular the TCoDe [10] and TFBoost [63] packages are developed inside the TimeSPOT collaboration.

The transient simulation start with the energy deposit that is modelled via the GEANT4 [62] Monte Carlo simulator. The simulation performs a sequence of single particle interactions in the silicon detector. Each particle is a positive pion with momentum of 270 MeV/c and impinges on the detector surface with an uniform spatial distribution and with an angular distribution in agreement with the characteristics of the PSI π-M1 beam line (angular divergence on the target of 35 mrad horizontal and 75 mrad vertical). For each event, the energy deposits, the trajectories of the incoming pion and all the secondary particles produced in its interaction with the silicon detector

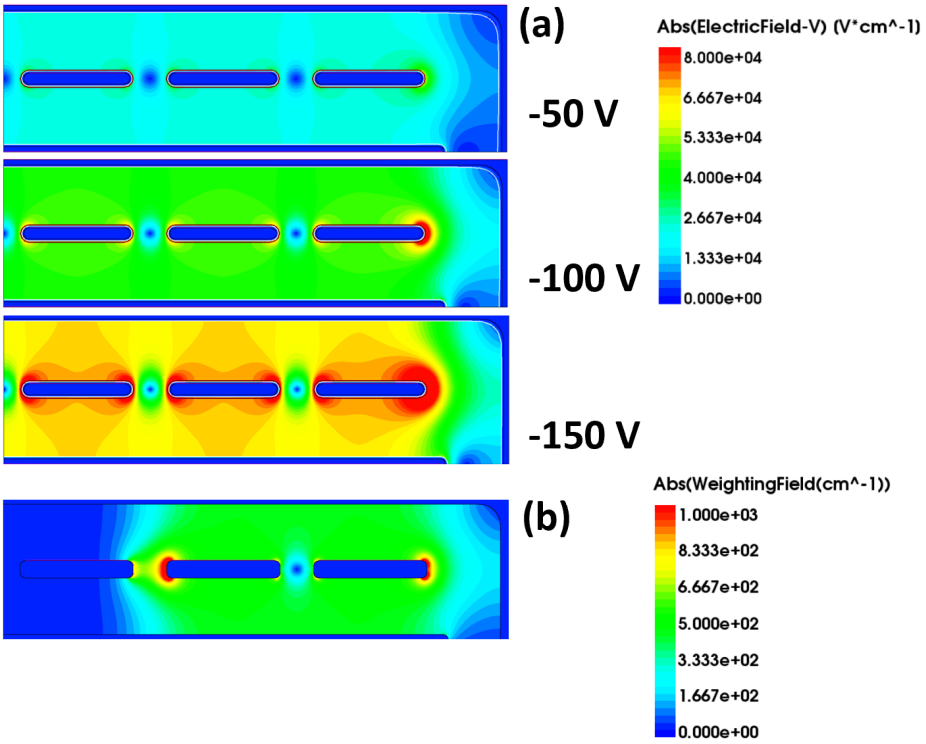

Fig. 4.12 (a) Electric field amplitude at different bias voltages for the double-pixel test structure and (b) weighting field.

are computed. This information and the results of the TCAD static simulations are then used by the TCoDe simulation package to compute the charge carrier kinematics and calculate separately the effect of single charge motion inside the volume and the consequent induced signal on the readout electrode.

For a quantitative comparison with measurements the induced signals, simulated with TCoDe, need to be convoluted to the front-end electronics response of the board used for the beam test characterization. In order to accomplish this, an open-source application named TFBoost (TimeSPOT Front-End Booster) was used. In particular, TFBoost allows to perform convolutions between the set of input signals from TCoDe and the electronics transfer function by exploiting multi-thread parallelism, both in CPU and GPU.

4.7.3 Semiempirical method for transfer function determination

The transfer function acting on the transient signals generated in the sensor is characterised not only by the front-end electronics itself but also by the sensor capacitance and the impedance of the sensor-electronics connection (e.g. wire bonding). For this reason, a direct and accurate measurement of such transfer function requires the sensor connected to the electronics. This make a semiempirical approach more convenient to estimate this transfer function. The method consists of the measurement of the response of the DUT under the laser setup, as shown in the previous sections. The measurements are done in such a way that the energy deposition is as similar as possible to that one of a MIP, (approximately 2 fC). In order to have higher accuracy in the transfer function estimation average signals from 3000 waveforms are recorded. The recorded signals are then deconvoluted with TFBoost using the simulated currents obtained from TCoDe at the corresponding laser positions and bias voltages. In this case a specific TCoDe tool that simulates laser energy deposition, tuned to the laser characteristics reported in Chapter 6, is used for the energy deposition and the calculation of the sensor currents. If the current transients of the sensor are precisely simulated, the deconvoluted responses are semiempirical precise descriptions of the front-end transfer function [64]. An example of the deconvolution procedure is shown in Figure 4.13 at -150 V bias voltage and in one specific irradiation position.

Several checks were done to verify the semiempirical approach, applying the method with different sensor bias voltages or in different laser excitation position and in all cases the transfer functions obtained were compatible. In particular, since the semiempirical

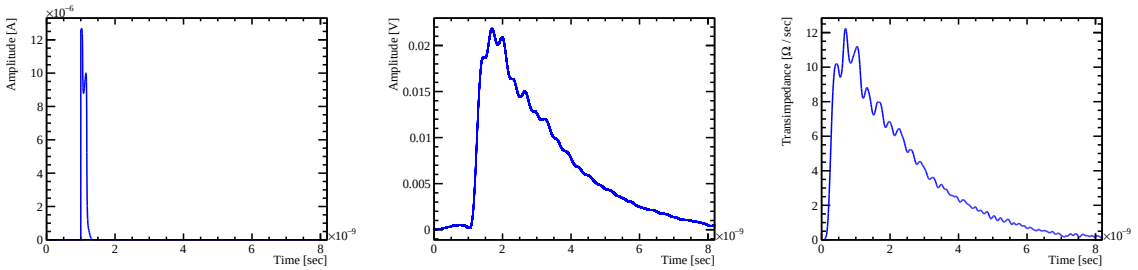

Fig. 4.13 Example of the front-end transfer function deconvolution. (Left) Simulated input current for an IR laser deposition in the sensor. (Centre) Averaged measured waveform using the IR laser setup. (Right) Deconvoluted front-end transfer function.

transfer function depend only on the electronics response and the electronics-sensor coupling, a direct comparison of the transfer functions, obtained at different laser positions and at different bias voltages, allows to verify the robustness of the method. This because a variation on the excitation positions cause a variation of both the simulated current and the measured signal. This study is shown in Figure 4.14 and, as expected, the resulting transfer functions are in a very good agreement, especially in their rising edges.

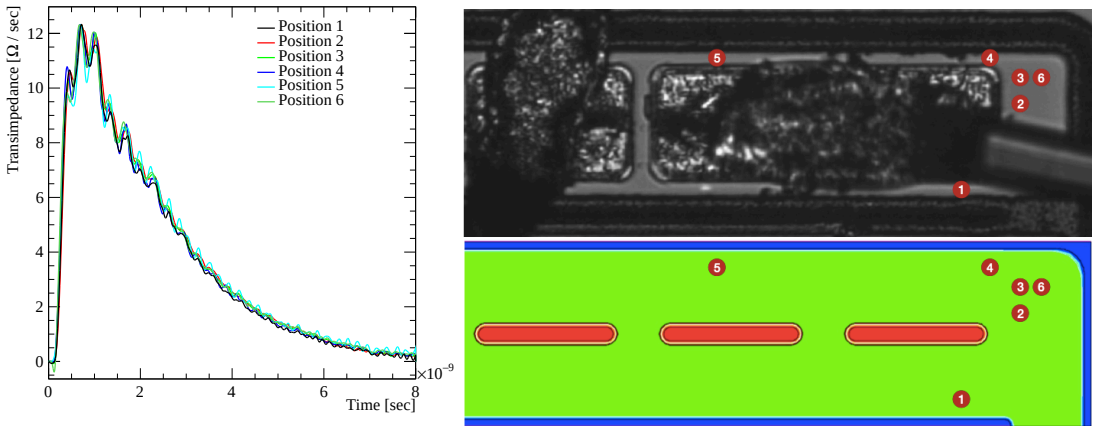

Fig. 4.14 (Left) Comparison of semiempirical transfer functions obtained in different irradiation positions with the laser setup. (Right) Illustration of the excitation positions of the actual double-pixel test structure (top) and the corresponding positions in the simulated structure (bottom).

4.7.4 Simulation results

The results of the convolution of the TCoDE currents to the semiempirical transfer function are shown in this section. The TCoDE currents refers to several events of energy deposition simulated with the GEANT4 tool reproducing the beam condition of the PSI beam test. In order to fully reproduce the beam test sensor signal, realistic noise waveforms are added to the simulated waveforms. The noise waveforms are several signals, generated by the tested board, in absence of laser excitation and recorded by the same oscilloscope used in the beam test.

The resulting waveforms reproduce with very good accuracy the different structures visible in the mean waveform shown in Figure 4.15, computed by averaging about 30000 waveforms. The main quantities representing the signals properties agree within 5% and are summarised in Table 4.2. The good agreement between data and simulation is also visible by comparing qualitatively the single waveforms, as shown in Figure 4.16.

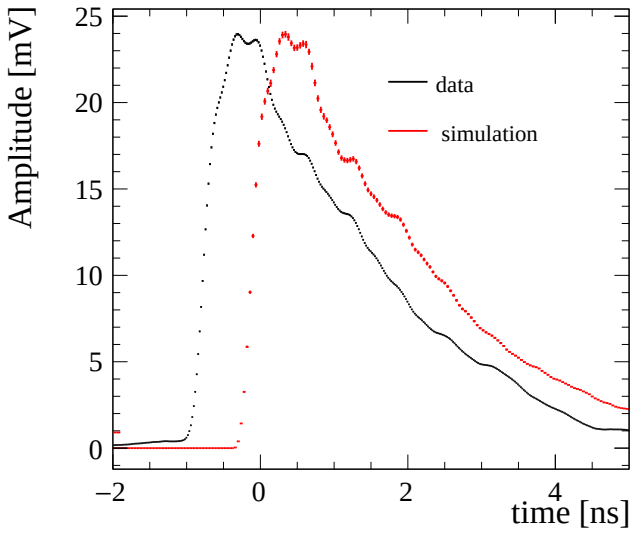

Fig. 4.15 Silicon sensor average waveform from the full (black) data and (red) simulation sample (about 30000 signals). An arbitrary time shift between the two shapes is applied to allow a qualitative comparison.

Figure 4.17 shows the reconstructed amplitude for data (black) and simulation (red) at $V_{\text{bias}} = -150$ V. The simulation reproduces the data distribution that is characterised by a Landau probability density function shaped by the trigger acceptance function at low amplitudes.

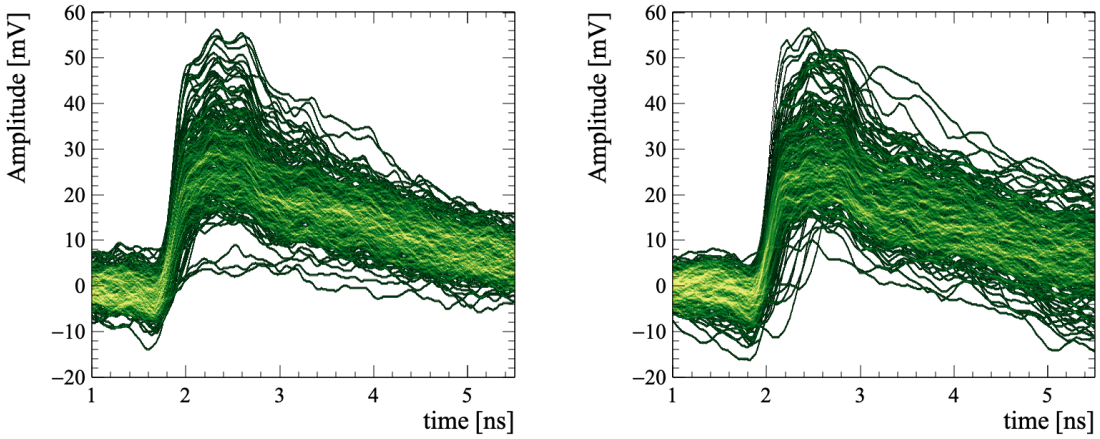

Fig. 4.16 Overlap of 3000 silicon sensor waveforms for (left) simulation and (right) test beam data.

Table 4.2 Maximum amplitude, noise and rise time (20-80%) of the 3D trench silicon sensor signal at different values of the bias voltage for simulation and data. The statistical uncertainties are below 1%.

	V_{bias} [V]	Amp(P_{max}) [mV]	$\langle N \rangle$ [mV]	rise time [ps]
Simulation	−50	25.0	2.11	247
	−100	24.5	2.17	224
	−150	24.4	2.19	217
Data	−50	24.1	2.19	258
	−110	24.4	2.30	221
	−140	24.7	2.29	217

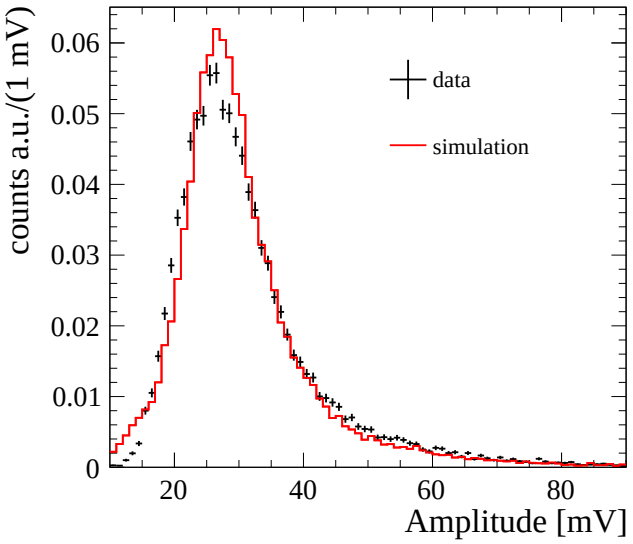

Fig. 4.17 Distribution of the reconstructed amplitudes for the silicon sensor in data and simulation at $V_{\text{bias}} = -150$ V.

In order to obtain the time distribution, and evaluate the origins of the tail of late signals, the reference method described in Section 4.5 is applied to the simulated waveforms. To take into account the uncertainty of the pion arrival time, that for the beam test measurements was 12.5 ps (given by the MCP-PMTs), a random value generated according to the measured time reference resolution is subtracted to the time of the simulated waveforms. Figure 4.18 shows the distributions of the time difference between the silicon sensor signal and the pion arrival time, $t_{\text{Si}} - \langle t_{\text{MCP-PMT}} \rangle$, for data (black) and simulation (red). The time distributions of the simulated data are in very good agreement to the measured distributions, both in the region of the peak and of the tail. The good agreement of the simulation results to the measured data allows to use the simulation tool to investigate in detail the ToA distribution measured at the PSI beam test. In particular with the simulation it is possible to investigate the distributions of the ToA with respect to the coordinates of track impact point, which are shown in Figure 4.19 The slowest events of the distributions are produced in a small region on the right of the double pixel, $165\,\mu\text{m} < \text{X} < 189\,\mu\text{m}$ (side region). In this region the electric field is lower but sufficient to collect charges and produce a signal that exceeds the imposed threshold.

In a real detector made of a 3D pixel matrix, the contribution of the side region might possibly affect only the pixels located at the borders of a matrix. Since this

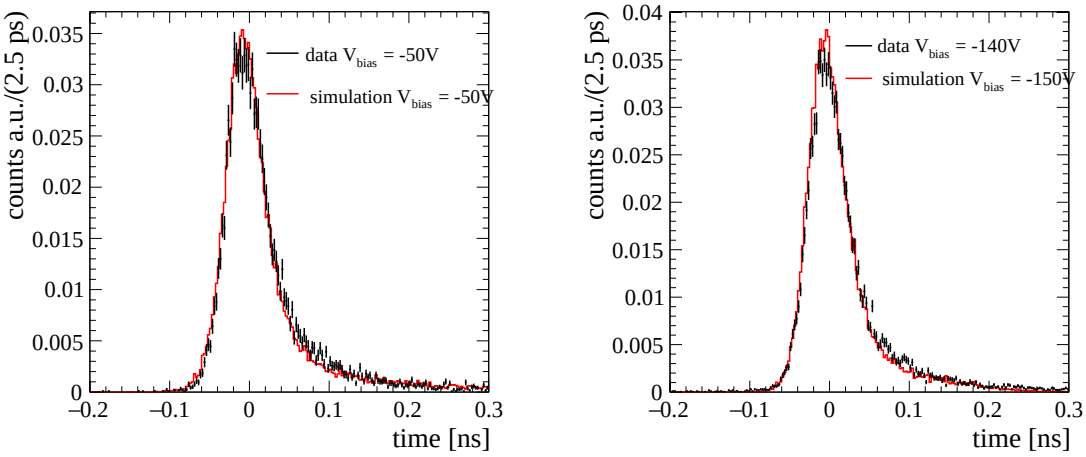

Fig. 4.18 The distribution of the time difference between the 3D trench silicon sensor signal and the pion arrival time at (left) $V_{\text{bias}} = -50$ V and (right) -150 V for (black) data and (red) simulation.

zone is not representative of a double pixel sensor, it must be excluded for the timing characterisation of the double pixel.

The time distribution of the simulated response at $V_{\text{bias}} = -150$ V is shown in Figure 4.20. The contribution from the double pixel region and the side region are highlighted. The tail is due to signals originated in the side region, while the signals originated in the double pixel contribute to the peaking structure, originating a low asymmetric distribution.

This study allowed to understand the importance of the boundary conditions for 3D sensor timing characterizations. In the next chapter a full characterization of a single 3D trench silicon pixel sensor, made for the second batch of TimeSPOT sensors is presented. The new measurements exploit a more performing custom made front end electronic amplifier which, thanks to a reduced electronic jitter, allows to better study the timing performances of a 3D trench silicon pixel sensor.

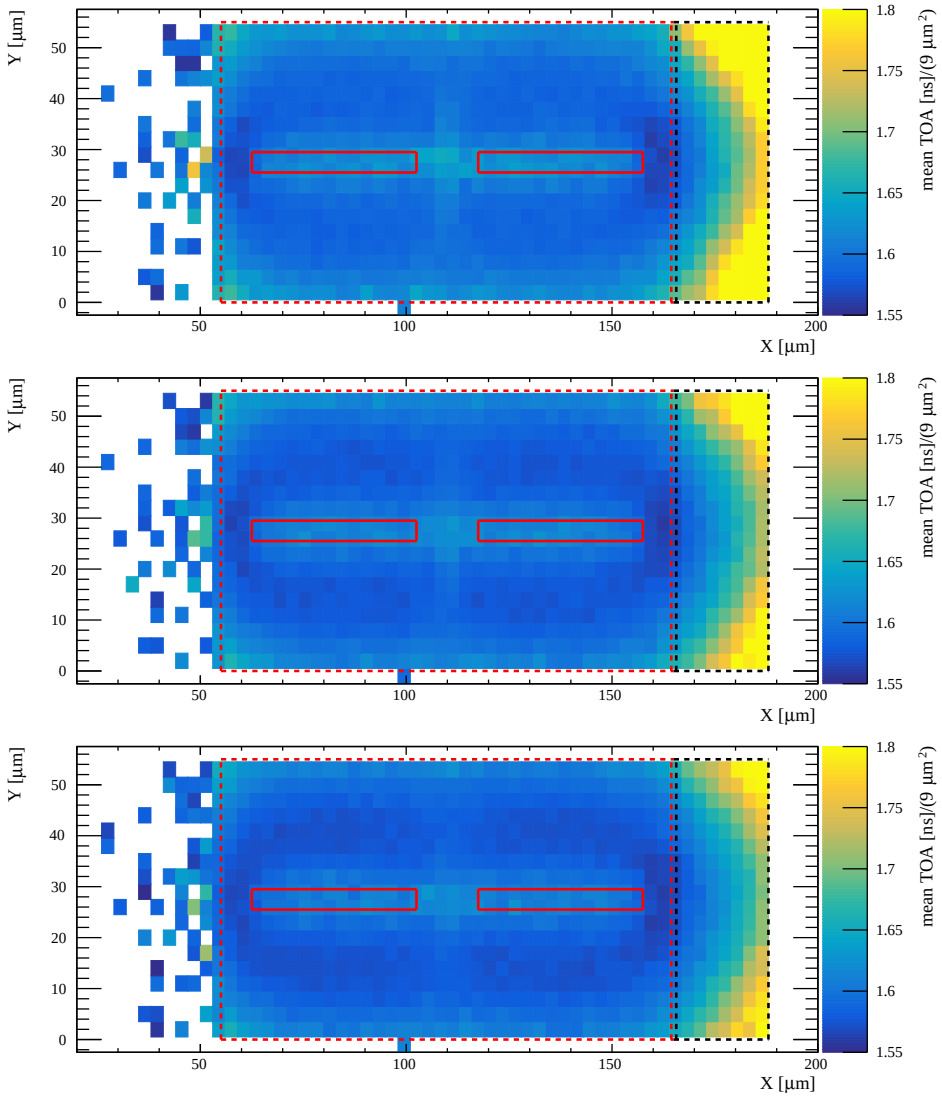

Fig. 4.19 Simulated signal mean time of arrival with respect to the (X,Y) track impact point coordinates. The double pixel region is limited by the red-dashed line, while the *side region* is limited by the black-dashed line. The readout trenches are indicated by the full-red lines. The simulations correspond to a bias voltage (from top to bottom) $V_{\text{bias}} = -50, -100$ and -150 V.

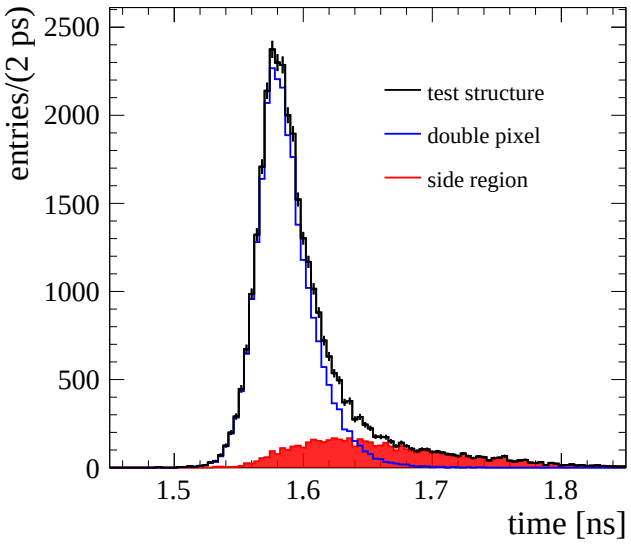

Fig. 4.20 Distributions of the time of arrival for simulated signals at a bias of −150 V. All reconstructed signals in the test structure are included, where the contributions due to signals originated in the double pixel ($55\,\mu\text{m} < \text{X} < 165\,\mu\text{m}$) and in the low-field *side region* ($\text{X} > 165\,\mu\text{m}$) are overlaid.

Chapter 5

Second TimeSPOT 3D trench batch beam test characterization

This chapter summarize the measurements of the non-irradiated 3D trench TimeSPOT sensors made in the October 2021 and May 2022 beam test campaigns at the SPS H8 beam line.

The new sensors test structures, made in the second TimeSPOT batch, allow to read a single pixel sensor providing the proper bias voltage to the adjacent pixels. This avoids the long tails that characterized the sensors time distributions obtained at the previous beam test, which, as reported in Section 4.7, they are not representative of a 3D trench pixel. The new test structures and a new custom made front end amplifier board, which in the previous beam test was the limiting factor of the measured time resolution, allow to accurately measure the timing performances of a 3D trench pixel. Finally, the usage of a new setup for the fine alignment of two small test structure permits to remove the DUT from the data acquisition trigger condition and thus perform unbiased characterizations and, for the first time, detection efficiency measurements of 3D trench TimeSPOT silicon sensors.

5.1 Test Structure

The tested devices are 3D trench silicon pixel sensors made in the second TimeSPOT production batch by Fondazione Bruno Kessler (FBK) in Trento. A detailed description of the 3D trench TimeSPOT pixel is reported in Section 2.2. Several structures are characterized under the beam, of three different type, as shown in Figure 5.1. They are single pixel sensors, single strip sensors (10 pixels with the collecting electrodes shorted

together) and triple strip sensors in which three adjacent strip sensors are connected to the same readout channel.

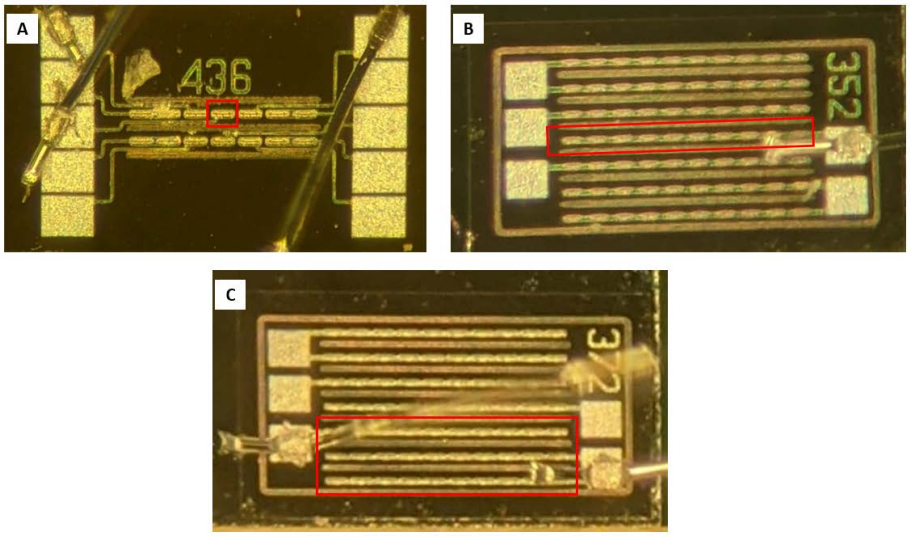

Fig. 5.1 Pictures of some of the 3D pixel test structures used in this work. For each structure the active area is outlined in red. (A) Single pixel sensor; (B) strip sensor (10 adjacent pixels located on the same row); (C) triple strip sensor (30 pixels located in three adjacent rows).

The single pixel test structure is composed of seven adjacent pixels that can be individually readout. To test a single pixel with the proper electric field condition, even in the outer zones, the test structure was wire bonded in such a way to have a central pixel connected to the amplifier input and the two adjacent pixels connected to ground. This allows testing a pixel in the same electric field condition of a pixel inside a matrix. A different arrangement was done for the charge sharing measurements for which the adjacent pixels are connected to additional readout channels of a multi channel board in order to measure the effect of charge sharing between three pixels of the same row.

5.2 Front-end electronics

The results of the first beam test characterizations have shown the high impact of the front-end electronics in the time resolution of a silicon detector. In fact, the time resolution of the 3D trench double pixel, measured at the first beam test, was dominated by the amplifier electronics jitter. For this beam test campaign a new dedicated fast amplifier board is used in order to fully exploit the intrinsic time resolution of a 3D trench silicon sensor. The amplifier is based on wide-band Si-Ge bipolar transistors,

having transition frequency of about 85 GHz, and a very accurate design of the board to minimize high-frequency losses of the signals. The circuit is based on a transimpedance amplifier (TIA) scheme with two amplification stages to boost signal amplitude while keeping the noise at a reduced level. This front-end electronics features a signal-to-noise ratio (SNR) of about 20, a rise time below 100 ps and an electronic time jitter of about 7 ps at 2 fC input charge [65]. Two type of electronics boards were produced (see Figure 5.2), a single channel version and a four channel version, the last capable to readout up to four sensor. The TimeSPOT boards also provide the bias to the sensors, which are readout through a wire bonding connected to the amplifier input pads. A detailed description of the features and design of the boards used for the characterizations are reported in [66].

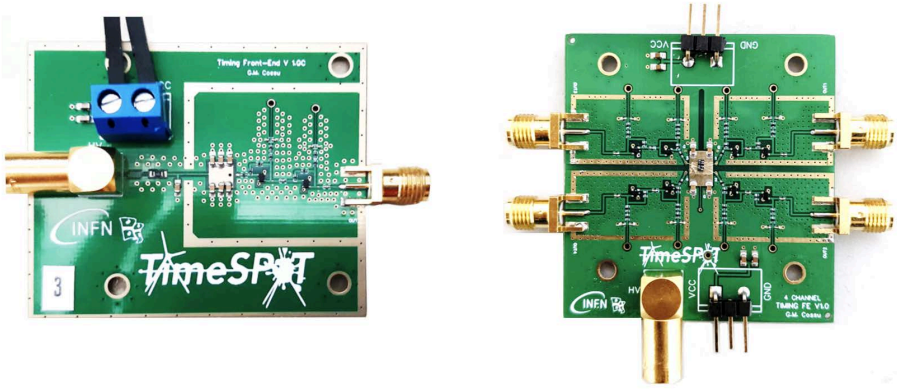

Fig. 5.2 The front-end boards: (left) single-channel and (right) four-channel versions. The sensors are attached with conductive tape to the large metal pad at the board centre and the readout electrodes are wire bonded to the input pad. The large metal pad provides the bias to the sensor under test.

5.3 Test beam setup

TimeSPOT sensors have been tested in October 2021 and in May 2022 at the CERN SPS H8 beamline with a 180 GeV/c positive pions beam. About 10^6 particles are extracted every 30 seconds in a 4 second long spill and are focused on an approximately circular spot of 8 mm (sigma). One of the main upgrade of this setup with respect to the one of the previous beam test is the use of two 3D silicon sensors one downstream of the other along the beamline. This was done in order to make unbiased measurements on the DUT. One of the two 3D sensors is installed on a fixed mount while the other is mounted on a movable holder driven by two closed-loop piezoelectric linear stages [67]

allowing the fine alignment of the two sensors with 10 nm position accuracy. In this way it is possible to trigger the data acquisition without imposing any amplitude threshold on the signals of the DUT but triggering on the signals of the other pixel and thus record all the events seen by the DUT. The two 3D silicon sensors wire-bonded to their front-end electronics (FEE) boards are mounted inside an electromagnetically shielded and light-tight box, as shown in Figure 5.3. Finally one of the holders also allows to manually rotate the sensor around the vertical direction in a such a way that non-normal beam incidence characterizations are possible.

The time of arrival of each particle is measured by means of two 18 mm diameter 5.5 mm thick quartz input window microchannel plate photomultipliers (MCP-PMTs) [68] that provide a better timing accuracy than those used on the previous beam test, of about 4 ps (see Section 5.5.2).

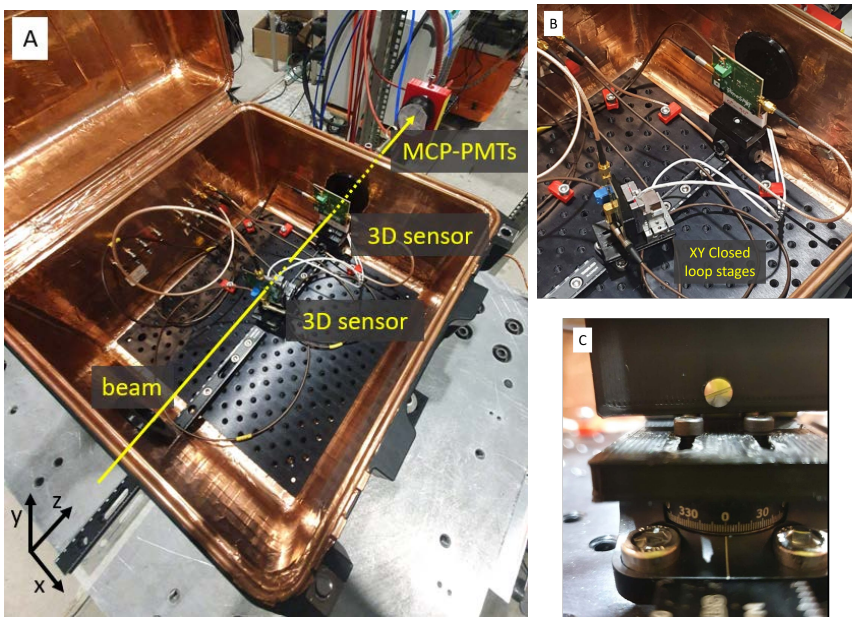

Fig. 5.3 The setup used for the measurements described in this work. (A) The sensors mounted on their FEE boards inside the RF shielded and light tight box and the two MCP-PMTs downstream; (B) The board mounted on the piezoelectric stages aligned to the another 3D trench sensor. (C) Manual rotation that allows to test sensors in non-normal beam incidence condition.

The signals from the silicon sensors and the two MCP-PMTs are acquired by means of an 8 GHz analog bandwidth 20 GSa/s 4 channels digital oscilloscope [69]. The sensors and the MCP-PMTs are connected to the oscilloscope using low-loss RF cables. The oscilloscope trigger condition is chosen in such a way that the sensor under test is not in the trigger. A typical trigger condition is the logical AND between one

MCP-PMT signal and one 3D sensor signal, this allows to reduce the rate of events without a signal in the DUT. A typical event recorded with this setup is shown in Figure 5.4.

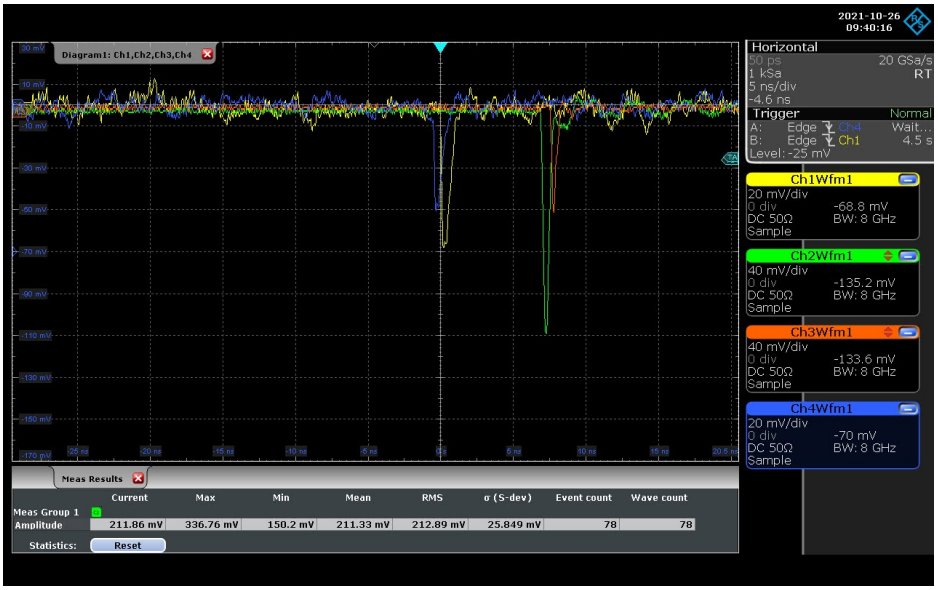

Fig. 5.4 A typical event. The signals from the two silicon sensors are shown in yellow and blue while the signals from the two MCP-PMTs are shown in green and orange. The relative timing between silicon sensors and MCP-PMTs signals is digitally adjusted to optimize the trigger condition.

5.3.1 Alignment procedure

An important step that guarantees an efficient data taking is the DUT alignment procedure with respect to the triggering pixel/strip. This step allows not only to maximize the rate of impinging particles on the trigger sensor but, since the DUT is not in the trigger, also the fraction of event containing signals of the DUT. A first alignment of the setup to the beam direction was performed using a laser level by adjusting the moving table position to center the two targets mounted on the red holders, as shown in Figure 5.5. This guarantees a preliminary relative alignment between the beam line and the optical rail in which all the sensors are mounted. The second phase is the alignment between two 3D silicon sensors, typically a 3D trench single pixel ($55 \times 55\,\mu m^2$) and a 3D trench pixel-strip ($55 \times 550\,\mu m^2$), but in some cases also alignments between two single pixels were made. Due to the small dimensions of the sensors a pre-alignment has been made by means of a USB microscope mounted

on a sliding support, as reported in Figure 5.5. The microscope has been used to accurately measure the position of the downstream silicon sensor with respect to the rail, then the sensor on the piezo stages has been moved up to the same position of the downstream sensor on the microscope's field of view. This procedure facilitate the fine alignment between the two sensors that is done with a scan in which the rate of coincidence signals between the two 3D sensor is measured. The result of a typical alignment scan of two pixels is reported in Figure 5.6.

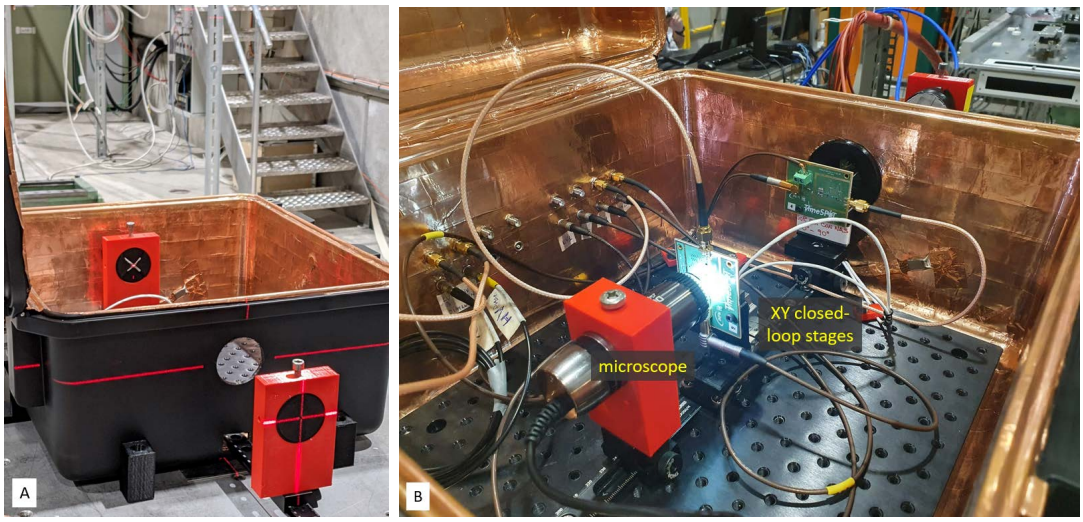

Fig. 5.5 (A) Adjusting the moving table position to align the optical rail with the beam line. (B) Relative alignment of silicon sensors by means of the USB microscope.

5.4 Waveforms analysis

The recorded waveforms of the four detectors placed in the beam line are analyzed offline in order to obtain informations on the DUT such as the amplitude distributions, the timing performances and the geometrical efficiency. The time of arrival (ToA) of each sensor signal is determined by different methods referred to as *reference*, *Spline* and Leading Edge (LE). The LE and the reference methods are the same of the previous beam test (see Section 4.5), while the Spline method is a constant fraction discriminator algorithm (CFD) and it interpolates the waveforms with cubic splines and sets the ToA to the time at which the signal exceeds a specific fraction of its maximum amplitude. The interpolation step allows to reduce the jitter due to the signals digitization made by the oscilloscope and is preferred to a linear fit (see PSI method of Section 4.5)

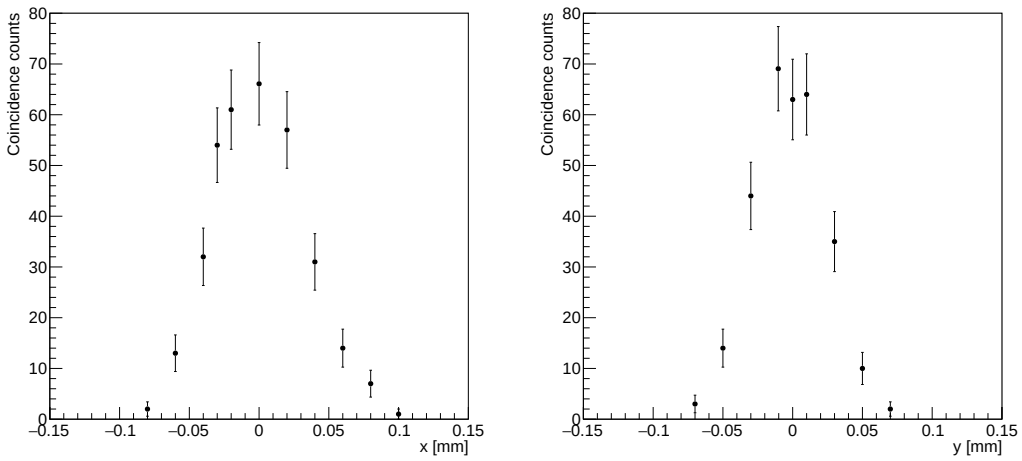

Fig. 5.6 Coincidence counts of two pixels during the alignment scans on the two ortoghonal transverse directions. The counts refers to two beam spills at the H8 beam line.

because it was found to be more stable. Finally, an amplitude-dependent time walk correction is applied to the LE method (LE amplitude corrected method).

5.5 Single pixel results

The results shown in this sections refers to 3D trench silicon single pixel structures. The characterizations concern the charge collection efficiency, by studing the DUT signals amplitude, and the sensor timing performances at room temperature operation.

5.5.1 Amplitude distributions

The amplitude distributions of a single 3D trench pixel are shown in Figure 5.7 for different applied bias voltages. The distributions follow the characteristic Landau shape and are well separated from the noise distributions which extend up to about 20 mV. For bias voltages higher than -50 V an amplitude reduction is noticed, this is due, as described in Chapter 6, to the fast front end amplifier that for higher charge collection times generates signals with lower amplitude (ballistic deficit). The measured distributions confirm the good charge collection efficiency of 3D trench sensor even if operated at very low bias voltages and, since the DUT was not on the trigger, it is assured that all the events crossing the DUT are taken into account for the characterization.

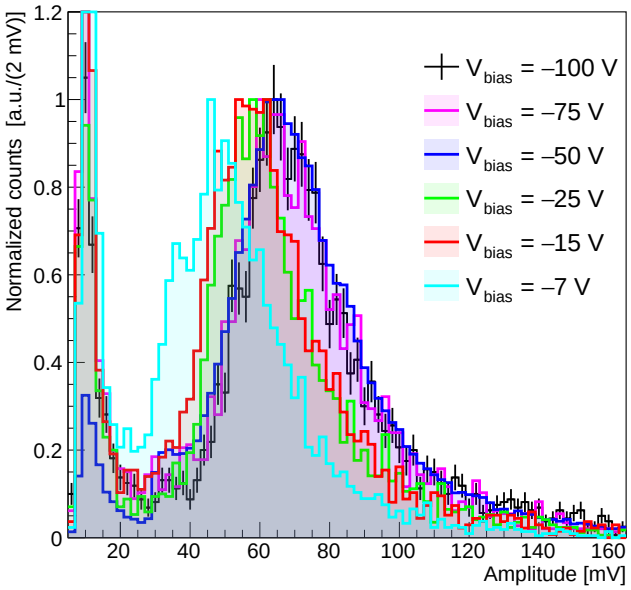

Fig. 5.7 Amplitude distribution of the single pixel at normal beam incidence and for different bias voltages. The distributions are normalized at the Landau peak.

5.5.2 Timing performances

The timing performances of the 3D trench pixel are evaluated by measuring several time the ToA of the 3D trench pixel's signals (using all the method reported in Section 5.4) with respect to the pions time of arrival, defined as the average time of the two MCP-PMTs. Before measuring the DUT time resolution the timing performances of the MCP-PMTs are evaluated. Figure 5.8 shows the time difference distribution, $t_{MCP-PMT1} - t_{MCP-PMT2}$, which has a resolution $\sigma_{\Delta_t} = 6.8\,ps$ that lead to a pions time of arrival accuracy ($\sigma_{\langle t_{MCP-PMTs}\rangle}$) less than 4 ps when the time information of the two MCP-PMTs are averaged, as Equation 5.1 shows:

$$\sigma_{\langle t_{MCP-PMTs}\rangle} = \frac{1}{2}\sqrt{\sigma^2_{t,MCP-PMT_1} + \sigma^2_{t,MCP-PMT_2}} = \frac{1}{2}\sigma_{\Delta_t}, \tag{5.1}$$

where $\sigma_{t,MCP-PMT_i}$ is the time jitter of the i-th MCP-PMT.

Figure 5.9 (left) shows the distribution of the time difference between the 3D trench sensor signal and the pion arrival time, $t_{\mathrm{Si}} - \langle t_{\mathrm{MCP-PMTs}}\rangle$. The distribution, obtained with the reference method, has a peaking structure with a very short tail of late signals, as predicted in the simulation reported on Section 4.7, and similar to the intrinsic time distribution of Figure 6.22 measured with the laser setup. A two Gaussian function is

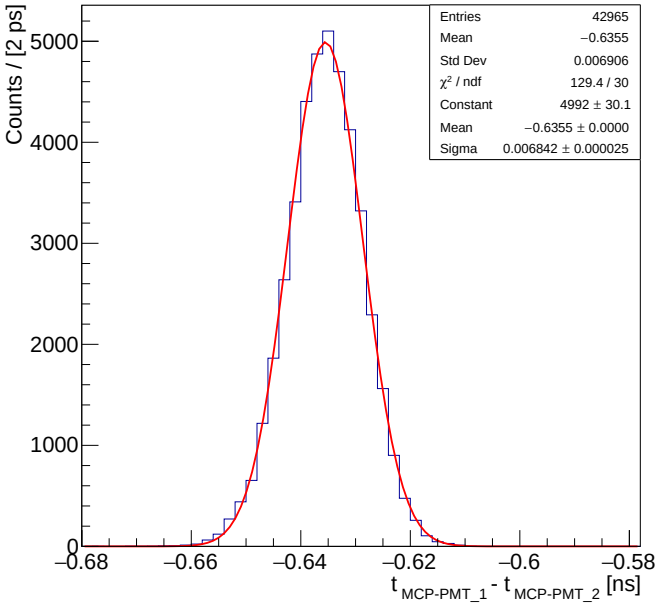

Fig. 5.8 Distribution of the time difference between the two MCP-PMTs with a Gaussian fit overlaid

used to determine the time resolution from the distribution. This function allows to describe the contribution of the signals originated in the central region of the sensor, while the secondary Gaussian describes the contribution of the signals originated close to the trenches that feature a slightly larger ToA as studied in detail in Section 6.4.2. In this case also the noise signals are present since no amplitude threshold is imposed to the DUT's signals, that are described by a constant added to the fit function. In fact, since the noise signals of the DUT are not correlated with the reference detectors a flat ToA distribution of the DUT noise signals is expected. The contribution of the two Gaussian functions are combined to compute the effective time resolution, according to the mixture probabilistic model [70], as:

$$(\sigma_t^{\text{eff}})^2 = f_1(\sigma_1^2 + \mu_1^2) + (1 - f_1) \cdot (\sigma_2^2 + \mu_2^2) - \mu^2, \tag{5.2}$$

where f_1 is the fraction of the core Gaussian and μ is defined as

$$\mu = f_1\mu_1 + (1 - f_1) \cdot \mu_2. \tag{5.3}$$

The result of the fit lead to an effective resolution of $\sigma_t^{\text{eff}} = 13.9 \pm 1.3$ ps, corresponding to a time resolution of the single pixel of $\sigma_t^{\text{Si}} = 12.4 \pm 1.3$ ps, that is obtained by subtracting in quadrature the jitter due to the time reference detector.

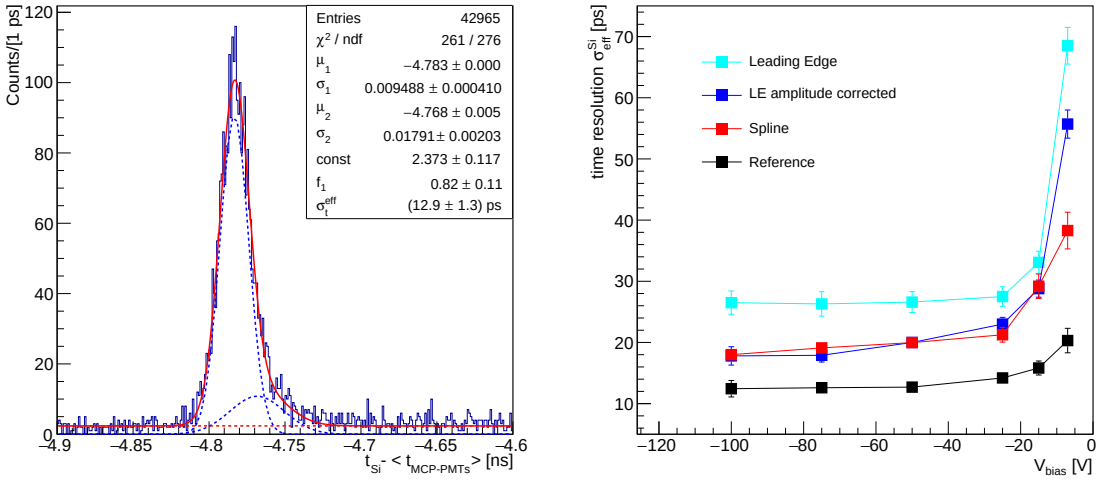

Fig. 5.9 (Left) Distribution of the time difference between the 3D trench single pixel and the time reference for $V_{\text{bias}} = -100$ V with the *reference* method. The distribution is fit with the sum of two Gaussian functions (blue dashed lines) describing the signal, and a constant (red dashed line) modelling the background. (Right) Time resolution of the single pixel at different bias voltages for the different analysis methods, the contribution due to the resolution of the time reference is subtracted.

Figure 5.9 (right) shows the measured values of σ_t^{Si} for the single 3D trench pixel operated at different bias voltages, for the analysis methods presented in previous section. The timing performances are almost constant for $V_{\text{bias}} < -25$ V, while they worsen rapidly for lower absolute bias voltages, this is mainly due to the sensor non-uniformity contributions that is investigated in detail in Section 6.4.2.

The best performances are obtained using the *reference* method, thanks to its capability of minimizing the time walk caused by charge collection time variations. Also, despite its simplicity, the LE method with fixed threshold provides time resolutions below 30 ps, while the LE method corrected for the time walk performs similarly to the *Spline* method.

5.5.3 Tilt operation characterization

Trenches in 3D pixel sensors are non-sensitive volumes, so if a charged particle crosses a 3D sensor inside a trench no signal will be recorded, as shown in Figure 5.10. To avoid

the channelling of the particles inside the electrodes, 3D pixels sensors are typically mounted at a slightly tilt angle with respect to normal incidence. This makes the characterization of 3D trench pixel operated tilted with respect to the normal incidence necessary.

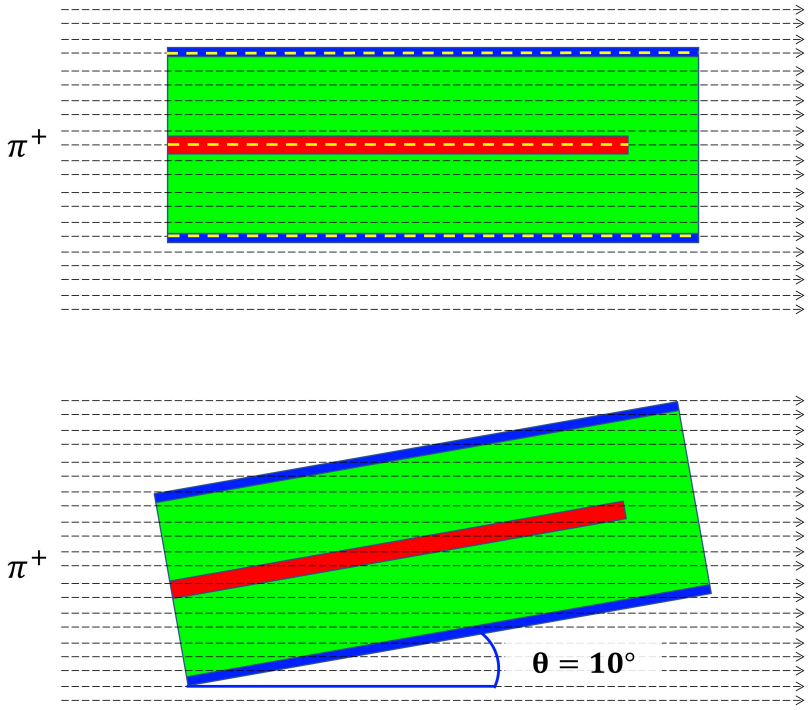

Fig. 5.10 (Top) Scheme of a 3D trench single pixel operated with beam normal incidence, the yellow lines represents the pions tracks that do not release collectible charges in the sensor. (Bottom) Scheme of the same pixel operated at a tilt angle of 10°, in this case no tracks channels into the trenches.

For various 3D trench pixel tilt angles (0°, 5°, 10°, 20°) 60k events are acquired. The acquisition runs are made using the same unbiased trigger used for the characterization at normal beam incidence condition and, for these studies, the pixel bias voltage is -100 V. Figure 5.11 shows the amplitude distributions of the 3D trench pixel for the four tilt angles. The distributions show that starting from 5° the low amplitude region starts to populate (18 mV $<$ Amplitude $<$ 50 mV). This behaviour is due to the particles that at small angles are not completely channeled and thus start to release collectible charges in the sensor active area. However, as the tilt angle increases (see Figure 5.10) the average tracks length decreases due to track sharing between adjacent pixels causing a reduction of the most probable value of the amplitude distributions. An amplitude decreases less than 30% is observed at 10° with respect to the one

obtained at normal incidence condition, leading the 2 fC to about a charge of 1.4 fC (most probable value) generated by the passage of a MIP.

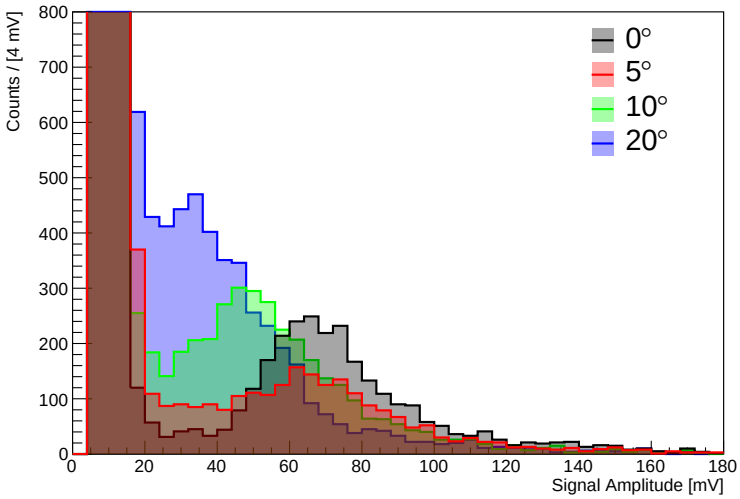

Fig. 5.11 Amplitude distributions of the 3D trench pixel operated at -100 V for different tilt angle operation.

The timing performances of the pixel for the different angles are also evaluated. Figure 5.12, shows that the time distributions obtained for the different angles do not change significantly. The time resolutions obtained from the fits show that there is no significant degradation of the time resolution for angles up to 10° while a slightly worse resolution is observed at 20°. This result might seem in contrast with the decreasing of signal amplitudes shown in Figure 5.11, which should lead to an increased electronic jitter, due to a decreasing SNR. However, the fact that no significant time resolution degradation have been measured could be due to a reduction of the sensor non-uniformity time contribution (see Section 3.6.1) that, since the contribution due to different distances from the trenches are mixed up for the tilted tracks, becomes smaller. This non-uniformity jitter reduction could compensate the increasing electronic jitter, due to the amplitude decreasing, allowing to obtain excellent timing performances even for tilted operation condition.

5.6 Efficiency measurements

Operating 3D trench sensors with a tilt angle with respect to normal incidence allows to increase the detection efficiency by avoiding the channeling of the particles inside

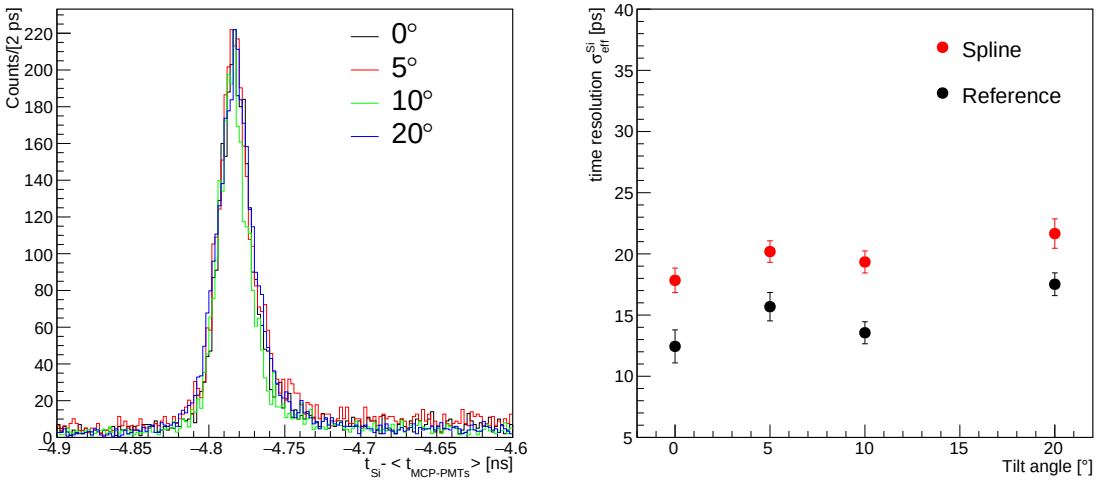

Fig. 5.12 Timing performances of a 3D trench single pixel operated at different tilt angles: (left) time distributions; (right) time resolution of as a function of the tilt angle, here the contribution of the time reference is subtracted.

the electrodes. In this section the effect of the geometrical acceptance on the detection efficiency of 3D trench silicon pixel sensors is studied as a function of the tilt angle with respect to normal incidence. This study allows to determine the optimum angles to operate the sensor in such a way that the detection efficiency of 3D trench sensors is maximized. The efficiency measurements are performed on a triple strip structure since a DUT with a higher geometrical acceptance than the trigger sensor is required for this method. The trigger sensor, in fact, acts as a reference counter of the particle detectable by the DUT that are those that crosses the DUT. The measurement are performed by triggering on a single 3D trench pixel which was precisely centered, along the beam line, on a triple strip (3 adjacent strips, each made of 10 pixels), acting as the DUT. The two MCP-PMTs signals are also acquired to obtain a precise charged particle time reference, useful for the noise rejection of the triple strip sensor. The efficiency measurements are performed at tilt angles of 0°, 5°, 10° and 20° with respect to the normal incidence by rotating the DUT around the pixel-strip axis. Moreover, to minimize the overlapping of insensitive volumes, the pixel trenches were oriented perpendicularly to the triple strip trenches, as shown in Figure 5.13.

The efficiency is computed as $\varepsilon = N_{ts}/N_{trks}$, where N_{ts} and N_{trks} are the number of tracks detected by the triple strip and the tracks crossing the triple strip volume, respectively. The number of tracks crossing the triple strip volume, is obtained by measuring the number of triggered signals, N_{trig}, with a minimum pulse height both in

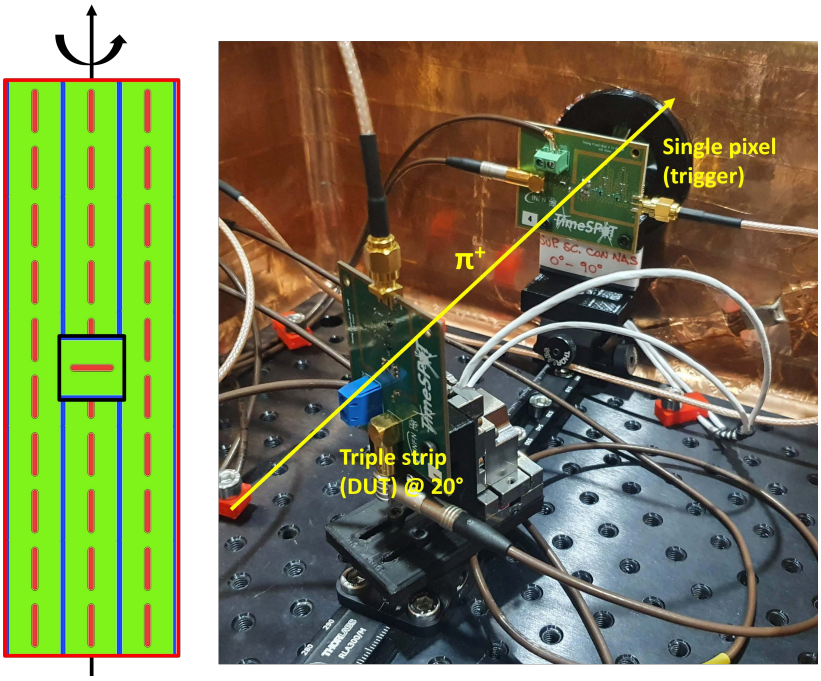

Fig. 5.13 (Left) Scheme of the efficiency setup: a single pixel is aligned on a triple strip sensor. (Right) Picture of the efficiency setup, several acquisition runs rotating the the triple strip around the vertical axis have been made.

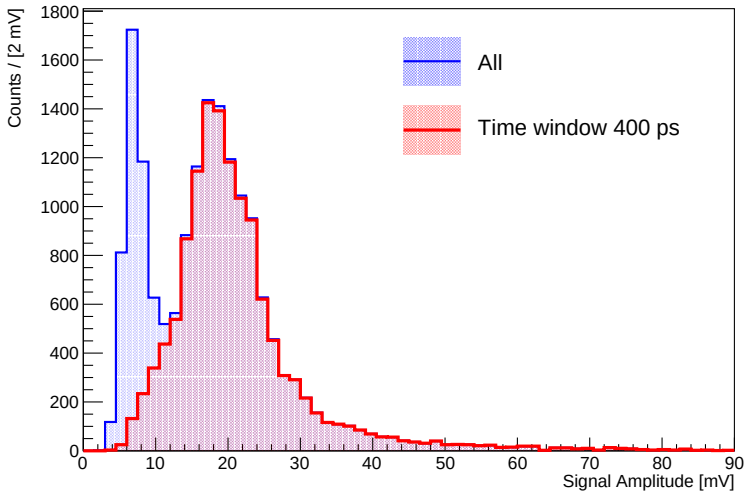

Fig. 5.14 Amplitude distribution of the triple strip sensor: (blue) all the triggered events, (red) events that have a ToA inside a time window of 400 ps centered at the ToA most probable value.

the single pixel and in the MCP-PMTs. This number is corrected by the fraction of tracks that miss the triple strip due to a small beam divergence: $N_{trks} = N_{\text{trig}} \cdot (1 - f_{\text{miss}})$. This fraction is estimated using a data sample acquired with the triggering single pixel shifted by 165 μm along the short side of the triple strip and amounts to $f_{miss} = 1.4 \pm 0.6\%$.

The estimation of the number of the tracks detected by the DUT is more complex because the signals of the triple strip sensor have a very low SNR. This is due to the 30 times higher capacitance at the input of readout electronic board since 30 pixels are connected to the same amplifier channel. For this reason a standard method, in which a voltage threshold is imposed to the signals, is not usable. In order to overcome this problem the timing performances of the 3D trench detector was exploited. In fact it is possible to use the time information to have a better selection of triple strip noise and signals. As an example of this, Figure 5.14 shows the signal amplitude distributions of the triple strip sensor for all the recorded signals and for the signals that have a ToA inside a time window of 400 ps centered to the ToA most probable value. The red distribution show that almost all the events with amplitude greater than 10 mV are maintained while a good portion of the events under the noise peak can be selected using the time information. The number of detected tracks is determined using the triple strip time distributions ($t_{\text{triplestrip}} - \langle t_{\text{MCP-PMTs}} \rangle$) and is estimated

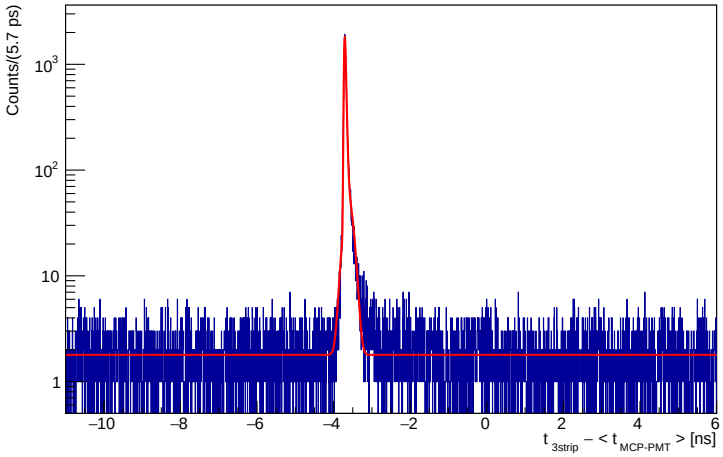

Fig. 5.15 Distribution of the difference between the TOA of the triple strip and the time reference, $t_{3\text{strip}} - \langle t_{\text{MCP}-\text{PMT}} \rangle$ for the triggered tracks with a minimum pulse height both in the pixel and in the MCPs in a time window of 200 ps, N_{trig}. The detected tracks populate the peaking structure around -3.5 ns, while the undetected tracks are uniformly distributed. The red curve represents the result of the fit to the distribution and it is used to determine the yield of detected tracks N_{ts} for the efficiency calculation.

imposing a fit of a peaking function, given by the sum of a Gaussian and an exponential convoluted with a Gaussian, to model the signal, and measuring the number of event under the peak. A constant function is also used to describe the undetected particles which feature random ToA values. Figure 5.15 shows the distribution of the difference between the TOA of the triple strip and the time reference for all the triggered events for the triple strip at 0°. From the fit function the number of events under the peak is measured and a detection efficiency of $\varepsilon = 79.0 \pm 0.7\%$ has been measured. As a cross check, the efficiency at 0° is also calculated simply by counting the number of events for which the triple strip signal has an amplitude above a certain threshold. For thresholds above the noise level (> 10 mV) the results agree with those obtained from the fit to the time distribution method, as reported in Figure 5.16. This supports the validity of the proposed method. For the tilt angle operation the efficiency, as expected, increases as a function of the incident beam angle with respect to normal sensor incidence, as shown in Figure 5.17. The results at 5°, 10° and 20° are $\varepsilon = 90.4 \pm 1.0\%$, $98.2 \pm 0.7\%$ and $99.1 \pm 0.6\%$, respectively.

The results reported in this work clearly shows that 3D trench sensors operated at a tilt angle with respect to normal incidence recover full efficiency for angles larger than 10°.

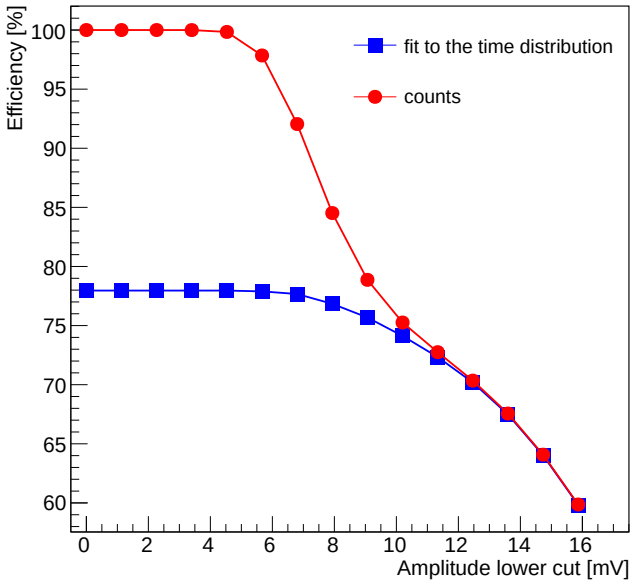

Fig. 5.16 Triple strip efficiency calculated by counting the yield of signal events from a fit to the time distribution (blue) and from the number of events with the amplitude above a given threshold (red).

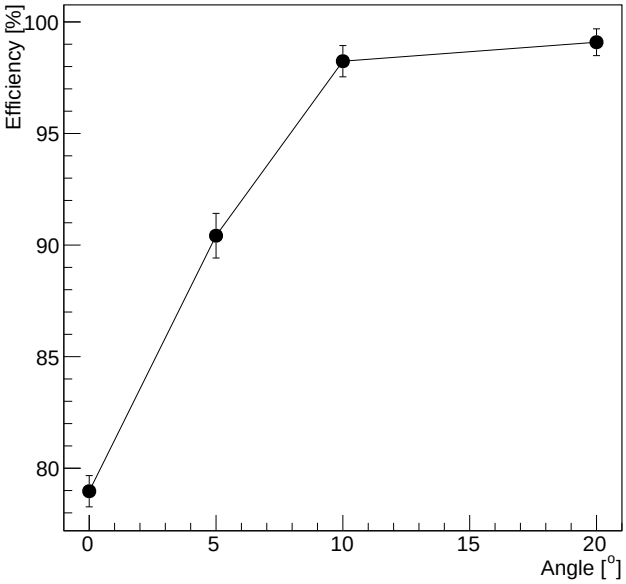

Fig. 5.17 Triple pixel strip efficiency as a function of the tilt angle with respect to normal sensor incidence. The DUT is rotated around the pixel-strip axis.

5.7 Charge sharing

The studies shown in the previous section have proven that 3D trench sensors must be operated at a tilt angle in excess of 10 degrees to achieve 99% detection efficiencies. However, in case of tilted operation, more charged particles typically crosses the active volumes of two adjacent pixels, and in these cases both pixels contribute to the particle detection. In this section studies of the charge sharing between two adjacent pixels, located on the same row, are reported for different incident beam angles. The DUT consists of two neighbour pixels which are individually readout using a multi channel board. The data acquisition is triggered by the coincidence of a signal detected by a single pixel and a signal of one MCP-PMT placed, respectively, upstream and downstream the DUT. For these acquisitions, since the oscilloscope has only 4 channels, a single MCP-PMT provides the time reference for the pions ToA. The triggering pixel was carefully aligned on the beam line and centered on the DUT to equalize the occupancies on the two pixels. The pixels were biased at a voltage $V_{\text{bias}} = -100$ V. This setup allows to study both the performance of a single pixel alone and that of the two pixels when considered as a cluster. Depending on the impact position and on the incident angle a particle can create a signal in one or both the adjacent pixels. In this study the following event categories were defined: the *whole pixel*, the *single pixel*, the *shared pixel*. All the events that satisfy minimal requirements on the pixel signal amplitude and on the ToA are labelled as *whole pixel* event type. The events for which the signal amplitude of the neighbour pixel is less than 15 mV and $|t_{\text{pixel}} - t_{\text{MCP-PMT}}|$ is greater than 100 ps are labelled *single pixel*. Viceversa, if a signal on the neighbour pixel is present ($A > 15$ mV AND $|t_{\text{pixel}} - t_{\text{MCP-PMT}}| < 100$ ps), the event is labelled *shared pixel* and, in this case, a *cluster* is made by combining the information of the two pixels. Figure 5.18(left) shows the amplitude distributions at 20° for the different event types. The distribution of the *whole pixel* events deviates from the characteristic Landau shape due to the contribution of the *shared pixel* events, populating the region of small amplitudes ($A < 40$ mV). By applying a clusterization algorithm to shared pixels events the resulting amplitude, given by the sum of the amplitudes recorded on the two pixels, recovers the expected Landau distribution. Figure 5.18(right) shows the amplitude distributions of the clusterized pixel for all measured angles, including both the information of the single pixel events (cluster size equal to 1) and of the shared pixels after clusterization (cluster size equals to 2). The distributions overlap for amplitudes higher than 45 mV and the shape of normal incidence beam condition is recovered for all the measured angles. The differences in the distributions at low amplitudes at 20°, are due to the events with cluster size equal to three that for this

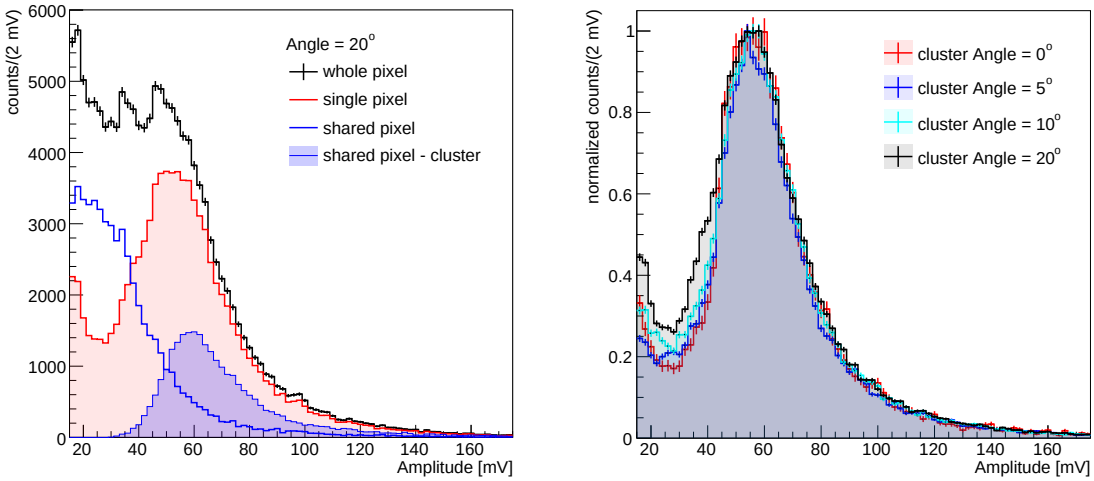

Fig. 5.18 (Left) Amplitude distributions at 20° with respect to normal incidence for different event categories; (Right) Cluster amplitude at various particle incident angles.

large angle become possible, so that a small amount of charge is lost in the presented two pixel setup. Concerning the timing performances, a clustering algorithm is applied to the shared pixel events. To do that the time distributions of the two pixels, obtained with the Spline method, are calibrated to have the same mean then, event by event, the ToA of the two pixels are combined together by means of an amplitude weighted mean:

$$t_{\text{cluster}} = \frac{t_1 A_1 + t_2 A_2}{A_1 + A_2}. \tag{5.4}$$

This is done for different fractions of shared charge, and several time distributions are obtained for different amount of shared charge. The time resolution evaluated from the time distributions are shown in Figure 5.19, for a tilt angle of 20°, as a function of the fraction of the amplitude deposited in one of the two pixels $A_1/(A_1 + A_2)$. From the plot emerges that the time resolution of the cluster is equal to the one of a single pixel when a low fraction of charge is shared (0.2 and 0.8) while for higher fraction of charge sharing, and in particular approaching 0.5, the clusterization give an improvement in time resolution. This results are not directly comparable to the one obtained for the single pixel characterization because the multi channel board have a lower SNR and only one MCP-PMT is used as a time reference. However what can be seen from the data is an improvement of the time resolution larger than 25% obtained with a cluster of the time information rather than using only the time of one of the two hit pixels.

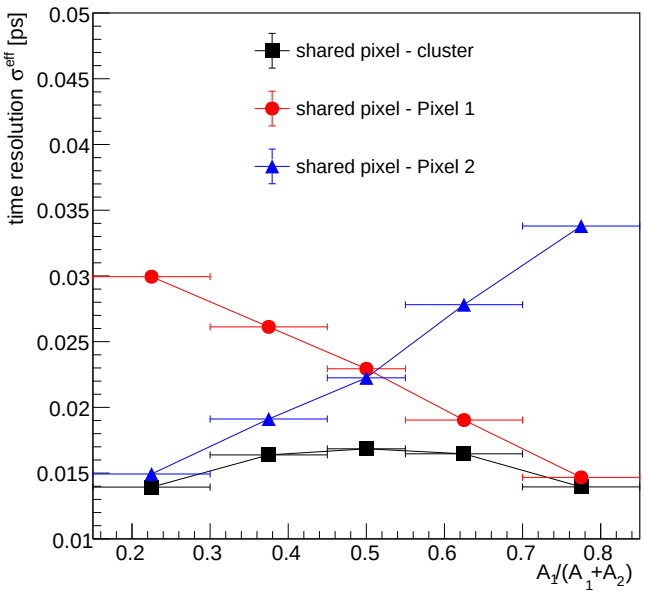

Fig. 5.19 Two-pixel cluster time resolution as a function of the ratio of the amplitude of one pixel to the sum of the two. The time resolution estimated using only the individual pixel information is also shown (red and blue curves). Results correspond to an incident beam angle of 20°.

5.8 Summary

In this chapter it was shown that high-energy charged-particle timing with a time resolution close to 10 ps can be achieved using the TimeSPOT innovative 3D trench silicon pixel sensors. This result is obtained using constant-fraction discrimination algorithms on the signals processed by a custom front-end electronics developed for the TimeSPOT sensors. The use of other timestamping methods, as the simpler leading edge discrimination technique, also allows to obtain excellent time resolutions close to 25 ps. Since the trenches in 3D pixel are an inactive detection material, pixel efficiency measurements at particles impact angles up to 20 degrees with respect to normal incidence were performed. As already observed in other types of 3D pixels, also 3D trench sensors recovers the full geometrical efficiency by tilting the sensors at 10° or more while maintaining excellent timing performances. Finally, since tilting the sensor increases the chance of having particles crossing two adjacent pixels, the two-pixels cluster was studied. By combining the ToA of two adjacent pixels with an amplitude-based weighted average of the individual pixels ToA, similar performances

to the one of a single pixel for all the sharing fractions are obtained. This guarantees an excellent time resolution also when the charge is shared between pixels.

Chapter 6

Infrared laser timing characterizations of 3D silicon sensors

The accurate characterization of a silicon pixel sensor, at a sub-pixel level, typically requires complex beam test campaigns in which several pixelated planes are used to obtain the hit position with a sub-pixel spatial accuracy. However, infrared (IR) laser excitation of the sensors allows to emulate the energy deposition of a Minimum Ionizing Particle (MIP). This allows to characterize silicon pixel sensors directly in the lab without the need of a beam test campaign and the use of several pixelated planes. Moreover, the advantage of a laser setup, with respect to the most common test systems (i.e. radioactive source and beam test characterizations), is the precise control of the energy deposition process in the device under test (DUT). This kind of setups typically allows to change the amount of charge deposited, the volume and the position in which the charge deposition occurs. They also provide reproducible energy deposition with high repetition rate, allowing to collect higher statistics, with the same acquisition time, compared to typical test systems. In this chapter a new IR laser-based setup made for sensor characterization, with a timing accuracy less than 1 ps, is presented. Finally the accurate characterizations of two 3D silicon sensors, a trench type and a columnar type are reported with an accurate comparison of the obtained results.

6.1 The laser setup

The IR-laser setup was realized in Cagliari for the characterization of the TimeSPOT 3D trench silicon pixel sensors. The laser system is a test-bench capable to emulate the charge deposition of a MIP (Minimum Ionizing Particle) in silicon pixel sensors with typical thickness of $\mathcal{O}(100\ \mu\text{m})$. The first element for the setup realization is the laser itself and, in the following, the arguments that have led to its choice are reported.

The attenuation of light that crosses a material follows the Lambert-Beer law that, in case of uniform attenuation, is expressed by:

$$I(x) = I(0)e^{-x/\lambda}. \tag{6.1}$$

Where *I(x)* is the intensity of the transmitted light after a length path x through the material and the initial light intensity and λ is the absorption length, a coefficient that depends both on the wavelength of the incident light and on the material through which the light is travelling.

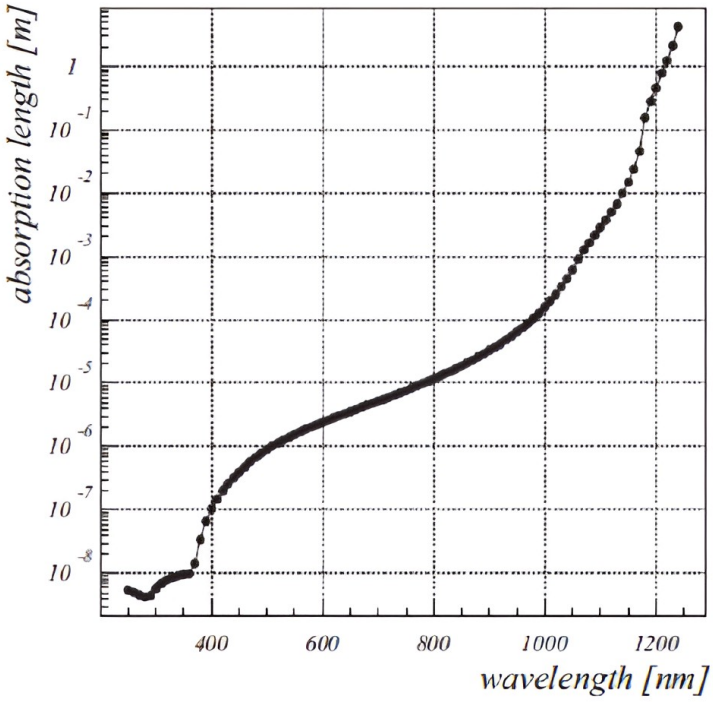

Fig. 6.1 Absorption length of light in silicon as a function of the wavelength of the incident light [12].

Figure 6.1 reports the absorption length in silicon as a function of the wavelength of the incident light. Wavelengths in the order of 1000 nm are a good compromise to

have enough light absorption, in O(100 μm) thick sensor, that is also homogeneous in all the sensor thickness. A higher wavelength does not create enough energy deposition in the sensor thickness while, for lower wavelengths the deposition profile along the sensor thickness become more and more inhomogeneous.

Another important parameter to emulate a MIP charge deposition is the pulse time duration that must be as short as possible. A long duration energy deposition would affect the charge collection process and so would bias the sensor induced current.

These requirements lead to the choice of a femtosecond pulsed laser and the chosen one is the Onefive Origami 10 [71]. It is a 40 MHz pulsed laser with a very short pulse duration, less than 200 fs. All the technical specifications are listed in Figure 6.2. In addition to those already specified, a very good beam quality (M^2) is required in order to maintain a Gaussian intensity profile when the laser is focused. Finally, since the setup is built to perform timing characterizations, the extremely low time jitter between consecutive laser pulses of this laser makes it ideal for this scope.

Optical

Model	ORIGAMI 05	ORIGAMI 08	ORIGAMI 10 (40 MHz)	ORIGAMI 10 (80 MHz)	ORIGAMI 10 (100 MHz)	ORIGAMI 15 (80 MHz)	ORIGAMI 15 (100 MHz)
Center wavelength [1]	515 ± 3 nm	780 ± 5 nm	1030 ± 2 nm			1560 ± 5 nm	1560 ± 10 nm
Pulse duration [1]	<180 fs	<160 fs	<200 fs			<200 fs	<100 fs
Average power [1]	>25 mW	>20 mW	>100 mW	>160 mW	>200 mW	>120 mW	>100 mW [2]
Pulse energy [1]	>0.625 nJ	>0.4 nJ	>2.5 nJ	>2 nJ	>2 nJ	>1.5 nJ	>1 nJ
Peak power	>2 kW	>2 kW	>10 kW	>8 kW	>8 kW	>6 kW	>8 kW
Repetition rate [1]	40 ± 2 MHz	50 ± 2 MHz	40 ± 2 MHz	80 ± 2 MHz	100 ± 2 MHz	80 ± 2 MHz	100 ± 2 MHz
Spectral band-width	Transform-limited ($\tau_p \cdot \Delta\nu \sim 0.32$)						N.A.
Beam quality	M^2<1.4, TEM_{00}	M^2<1.2, TEM_{00}	M^2<1.1, TEM_{00}				
PER	> 23 dB					> 18 dB	
Amplitude noise	< 0.2% rms, < 0.5% pk-pk (24h)						
Timing jitter	<30 fs rms [1 kHz-10 MHz]	<50 fs rms [1 kHz-10 MHz]	<30 fs rms [1 kHz-10 MHz]			<30 fs rms [1 kHz-10 MHz]	<30 fs rms [1 kHz-10 MHz]
Laser output	Collimated free space						PM fiber, FC/APC [3]

1) Please inquire for possible combinations of wavelength, pulse duration, average power, pulse energy and repetition rate
2) Ex. fiber
3) Armored single mode fiber, 20 or 50 cm, other lengths are available

Fig. 6.2 Onefive Origami 10 Laser technical specifications.

The Origami 10 has a fixed repetition rate of 40 MHz, meaning that in this setup a charge deposition occurs every 25 ns. To avoid events pile-up on slow DUT, a pulse picker is added to the setup in order to have a controllable laser repetition rate. The

pulse pickers systems are typically based on electro-optic or acusto-optic modulators, they are both able to select pulses with minimal pulse modification from a train of pulses. For this setup an electro-optic system based on Pockels-cells was chosen, the EKSMA Optics UP1 Ultrafast Pulse Picker [72], for which a scheme of its operation principle is reported in Figure 6.3. The setup is arranged so that the laser travels

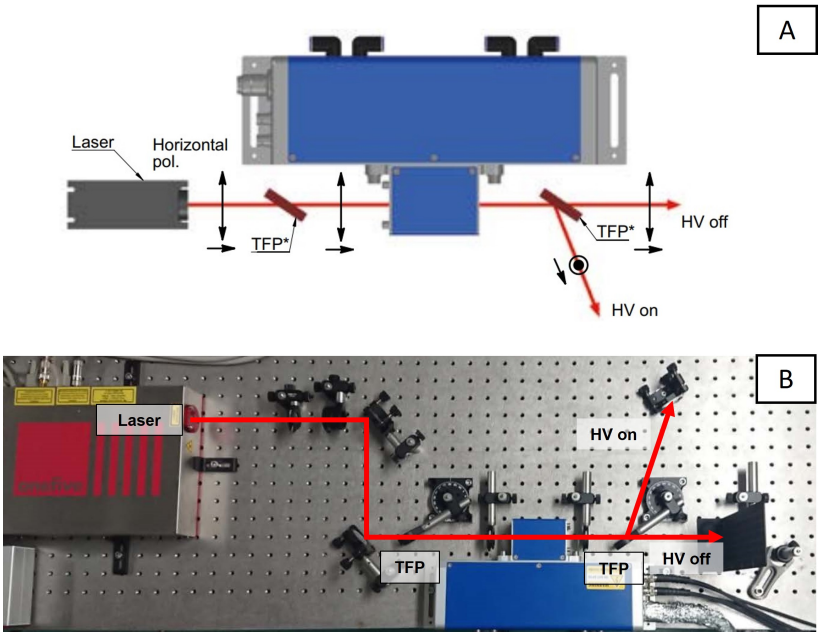

Fig. 6.3 (A) Schematic of EKSMA Optics UP1 Pulse picker typical usage. (B) Actual pulse picker implementation in the Laser setup.

through free air and reaches a first Thin Film Polarizer (TFP) that select the horizontal polarized light. Since the laser light is horizontal polarized this first filter is only used to remove spurious unpolarized light. After the first TFP the input of the pulse picker intercept the laser light and the Pockels-cells rotate its polarization of 90 degrees if an electrically controlled high voltage pulse, synchronous to the laser pulse to be selected, is applied. Finally the second TFP deflects the selected laser pulse while those not selected keep the same trajectory until they reach an absorber. The EKSMA Optics UP1 allows to select pulses from a single shot mode to a rate of 1 kHz. The path of the selected pulses is deflected by means of neutral filters that are used to adjust the laser intensity and so modify the amount of charge pairs generated in the DUT. A fiber port convey the laser light inside a single mode optic fiber that ends in the laser port of a microscope shown in Figure 6.4, the Mitutoyo VMU-L4B. Before its input a beam expander, reverse mounted, convey the light through a pinhole of 100 μm diameter which reduces the size of the laser beam. Finally the beam is focused on the

DUT through a 5X, 10X or 20X objective depending on the desired beam size. The

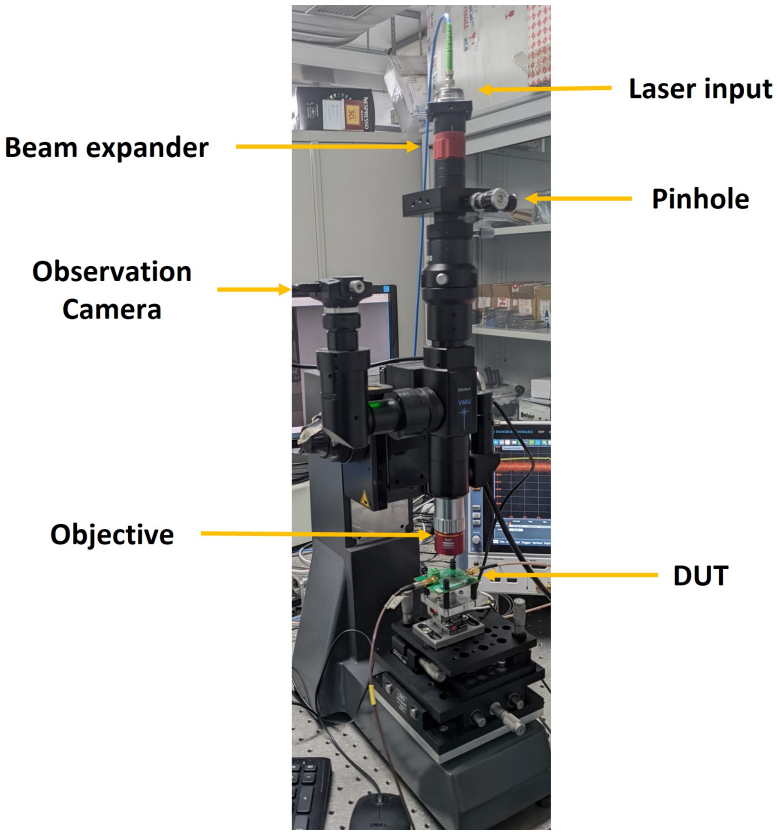

Fig. 6.4 Picture of the Mitutoyo VMU-L4B, the microscope used in the laser setup.

microscope is also equipped with a second arm that convey the light reflected from the DUT surface to an observation camera that is used to see the effective excitation position. Figure 6.5 shows a picture, taken by the observation camera, of the laser spot focused on the surface of a silicon 3D trench sensor, in which it is possible to see the very localized laser spot. From the images taken by the microscope camera it was possible to determine the laser beam transverse profile for the three different objectives. Figure 6.6 shows the recorded data from the camera. The width is determined imposing a 2D Gaussian fit to the data and it is of about 6 μm (FWHM), 3 μm and 1.8 μm respectively for the 5X, 10X and 20X objectives. Finally the DUT is placed on a custom made holder mounted on two perpendicular piezoelectric stages used to precisely move the DUT and perform laser scanning, with an accuracy of about 10 nm.

The simulated laser beam propagation in 150 μm of silicon active thickness is shown in Figure 6.7 for two cases: focusing on the surface or in the middle of the sensor thickness. Focusing inside the sensor thickness allows to have a more regular intensity

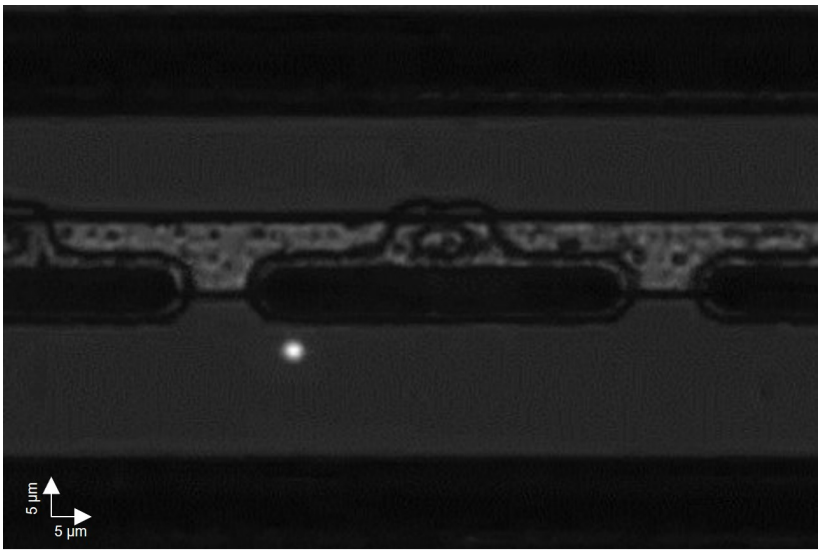

Fig. 6.5 Image taken by the microscope camera. Part of the laser spot is reflected on the sensor surface.

profile, very similar to a columnar shape that characterize the average one of a MIP charge deposition.

6.2 Laser scans and Data Acquisition System

A system of two piezoelectric stages allows to perform laser scans of the DUT allowing to measure the sensor response at a sub-pixel level. A LabVIEW software was developed to perform the scans. The software controls the stages and synchronizes the motion with the DAQ (Data Acquisition) system. The front panels of the LabView software are shown in Figure 6.8.

The DAQ is performed using a high bandwidth, ultra low noise oscilloscope, the Rhode&Schwarz RTP 084, featuring 20 GSa/s and 8 GHz of bandwidth. The oscilloscope records the DUT and Reference sensor signals which outcomes from the front-end amplifier boards described in Section 5.2 and are then analyzed offline.

The process flow of the LabView DAQ system is reported in Figure 6.9. The first phase is the initialization of the stages and of the oscilloscope, then the user can modify the DAQ parameters i.e. the number of waveforms to acquire for each position of the scan, average or single waveforms acquisition mode etc. After the definition of the DAQ parameters, the user selects the scanning area and the motion steps (a typical value is 1 μm). A grid of points is created according to the scanning area and the desired steps. Then the stages move to the first point of the grid and, when the position is

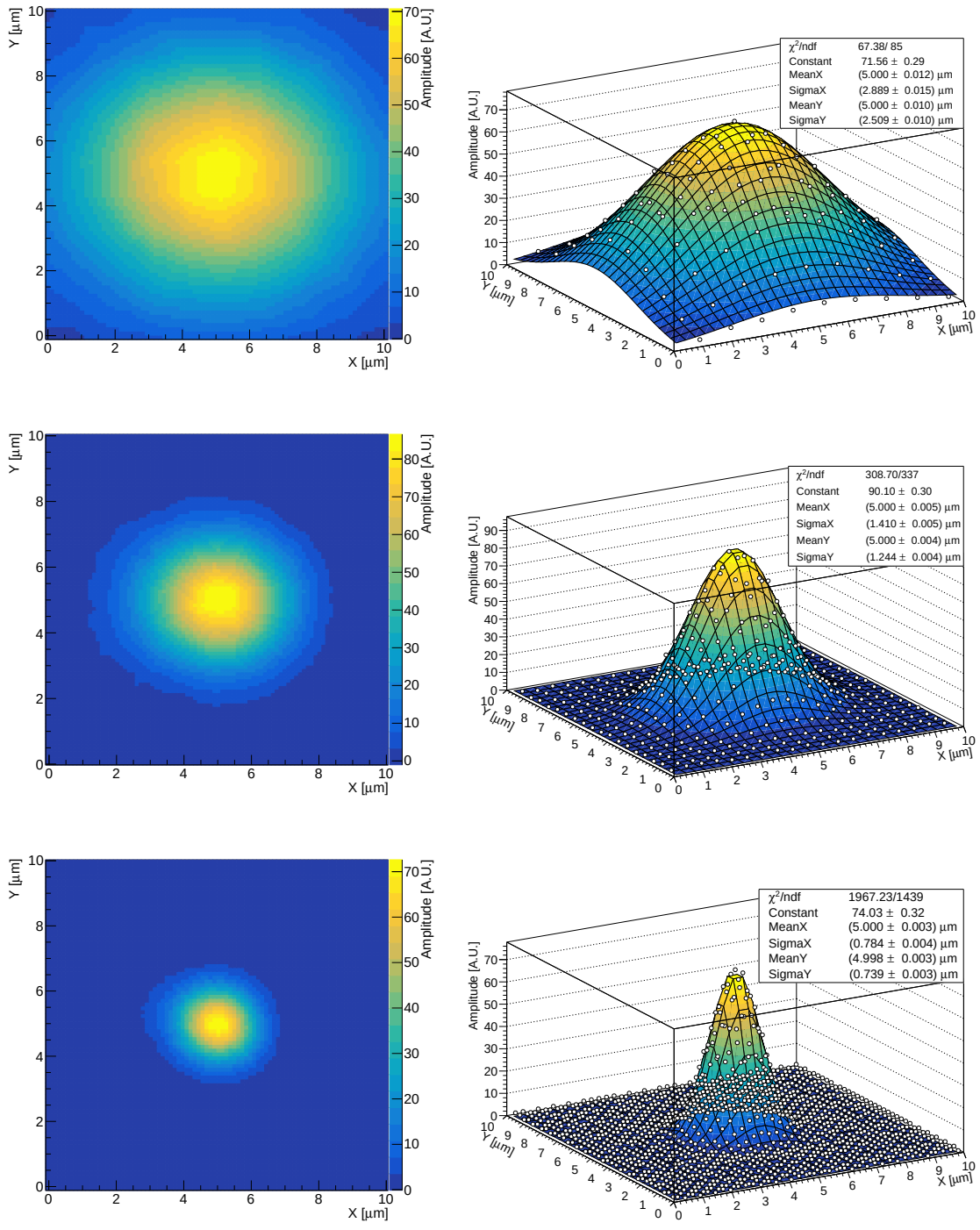

Fig. 6.6 Beam transverse profile, for (top) 5X objective, (central) 10X objective, (bottom) 20X objective. (left) Images of the laser taken with the microscope camera; (right) 2D Gaussian fit is imposed to the data in order to measure the beam width.

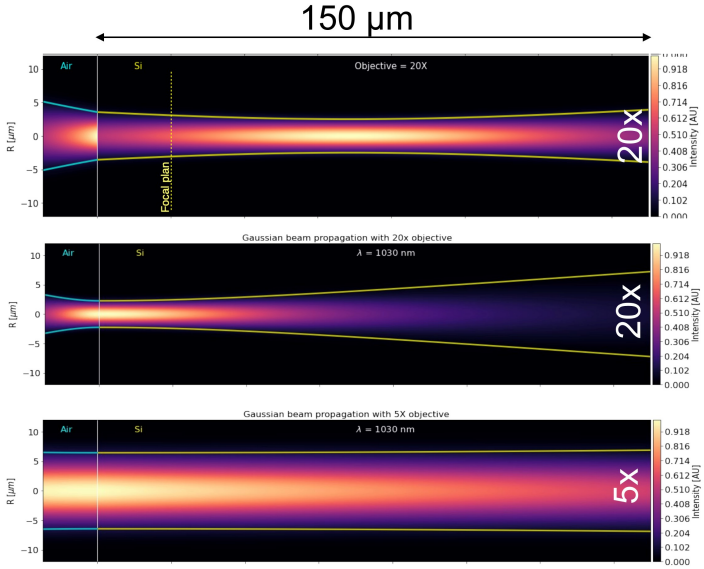

Fig. 6.7 Laser intensity inside the 150 μm sensor active thickness, (up) 20X objective focusing on the middle of the active thickness, (center) 20X objective focusing on the sensor surface. (bottom) 5X objective focusing on the middle of the active thickness.

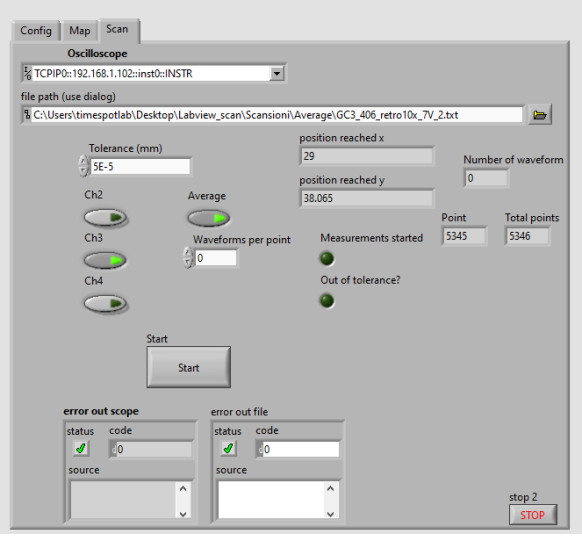

Fig. 6.8 Main panel of the LabVIEW software developed for the control and monitoring of the laser scans.

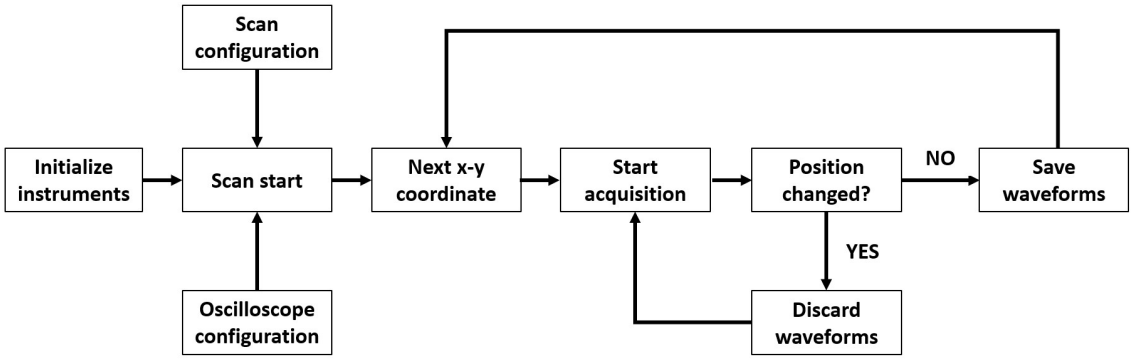

Fig. 6.9 Flux diagram of the LabVIEW software developed in this work for the laser system scans and DAQ.

reached, the oscilloscope trigger is armed and the waveforms acquisitions starts. During this phase the stages absolute position is monitored and if it differs from the nominal position, more than an adjustable tolerance, the recorded waveforms are deleted and the acquisition is restarted, otherwise the waveforms are wrote to a file and the stages move to the next point and so on until all the points of the grids are scanned.

6.3 A sub picosecond time reference detector

In order to perform accurate timing characterizations, a very precise time reference detector is mandatory. This detector have to measure the Time of Arrival (ToA) of the laser pulses with the minimum uncertainty, since it provides the time reference for the measurements of the ToA of the tested device. Specifically the DUT timing accuracy is evaluated by measuring the ToA variations of the DUT signals and the ToA is measured with respect to the absolute time t_0 given by the reference detector. Given t_{DUT}, the ToA of the DUT signal, the variations of the quantity $t_{DUT} - t_0$ can be expressed as:

$$\sigma_{\Delta t} = \sqrt{\sigma^2_{t_{DUT}} + \sigma^2_{t_0}}, \tag{6.2}$$

if $\sigma_{t_0} << \sigma_{t_{DUT}}$ it is possible to measure the DUT time fluctuations without the addition of the time reference jitter. If the time reference has a comparable resolution to the DUT the timing characterization is affected by the time fluctuation of the reference detector and a more sophisticated methodolgy of jitter subtraction must be applied to properly characterize the DUT. The reference detector used in the laser

setup has a time accuracy less than 1 ps [73]. The detector is a 3D trench TimeSPOT silicon pixel strip sensor that intercepts a spurious laser reflection coming from a lens crossed by the laser beam during its path in open air, as shown in Figure 6.10. Typical pulses of the reference sensors are reported in Figure 6.11. The measurements of its timing accuracy is done recording multiple waveforms of consecutive pulses. Since the laser has a repetition rate of 40 MHz, the time interval between two pulses Δt is 25 ns. The fluctuations of Δt represents the system accuracy for the measurement of the ToA of laser pulses. The Δt distribution is reported in Figure 6.12, the time of each signal is obtained with a CFD algorithm at 50% of the signal amplitude, and it shows that the fluctuation of two consecutive pulses, quoted as the σ of a Gaussian fit, is 1.28 ps. However, since Δt is the difference between the time of two consecutive signal its fluctuation is $\sqrt{2}\sigma_t$ (assuming that the noise of the two signals is not correlated) and so the time accuracy for a single ToA measurement, σ_t, is 900 fs. This time resolution is made by two contributions, the time resolution of the reference detector but also the time jitter of the laser itself. The very high amplitude, of about 10 MIP, and the homogeneous illumination bring the time resolution of a 3D silicon pixel sensor down to 900 fs, one of the best results ever obtained for timing detectors.

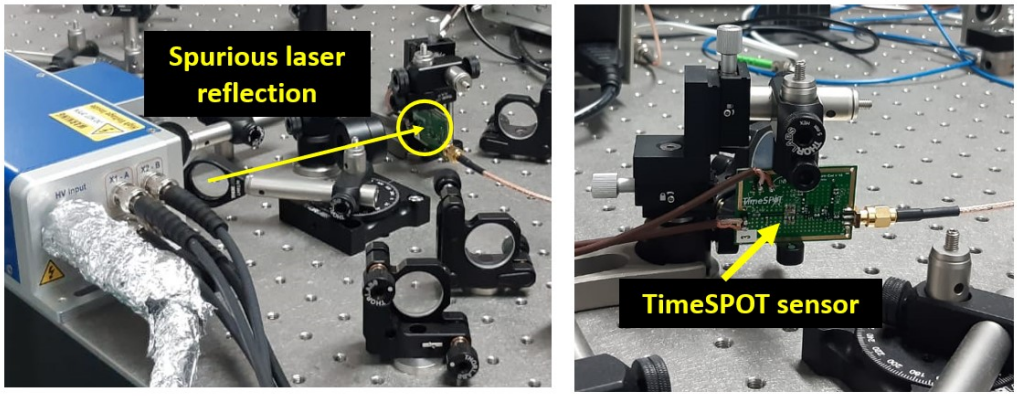

Fig. 6.10 Picture of the time reference detector, a 3D trench sensor, catching a spurious laser reflection.

6.4 3D trench pixel characterization

In this section the results of the laser scans of 3D trench silicon pixel sensor are shown. The DUT is a 3D trench silicon single pixel test structure fabricated in the second TimeSPOT batch of sensors and it is the same type of device tested with pions in

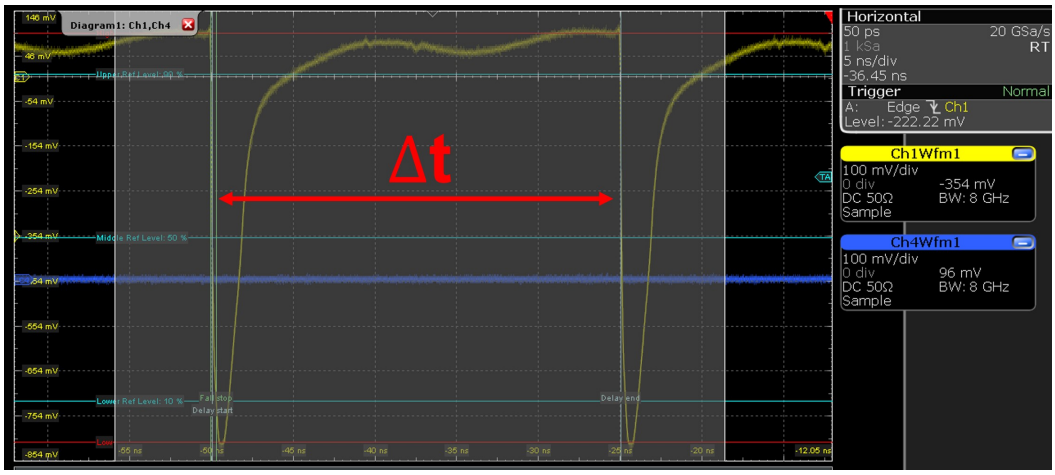

Fig. 6.11 Typical laser pulses of the reference detector. The repeated measurement of the time difference between two consecutive signals allows to estimate the reference detector time resolution.

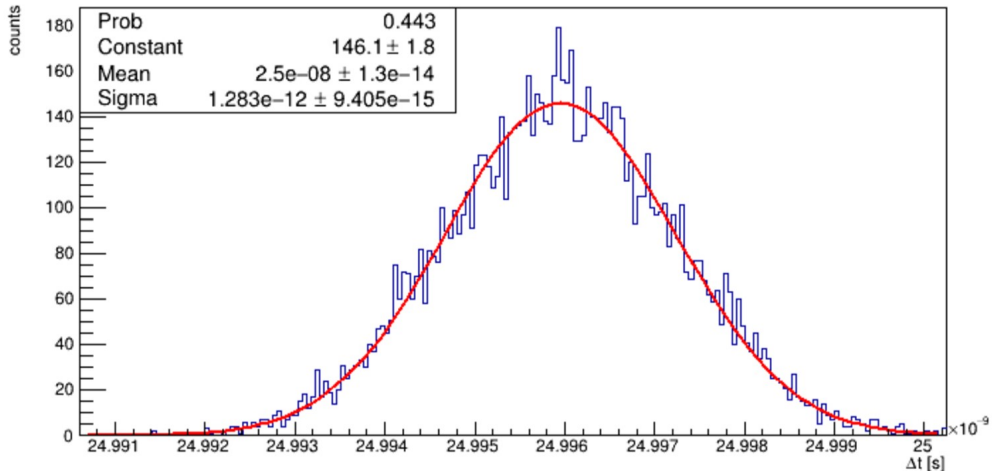

Fig. 6.12 Distribution of the time difference between two consecutive laser pulses. A Gaussian fit is imposed to the distribution, and a time resolution equal to $\sigma/\sqrt{2} \sim$ 900 fs is obtained.

the beam test described in Chapter 5. The test structure contains two lines of single pixels that can be tested individually. Wire bonding connection are made in order to connect the central pixel (DUT) of the top line to the amplifier board, which is the one reported in Section 5.2, while the two adjacent pixels are grounded, as shown in Figure 6.13. This configuration allows to test a pixel with an electric field condition similar to the one of a pixel inside a matrix of pixels.

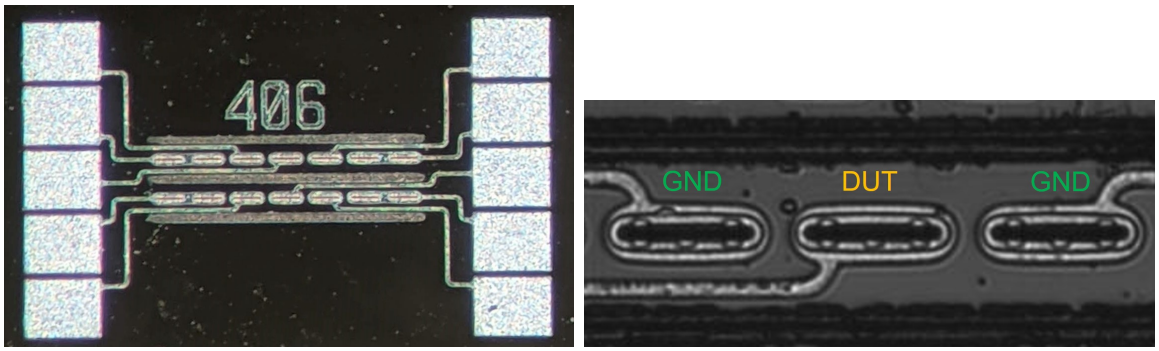

Fig. 6.13 3D trench single pixel structure. (Right) Magnification of the characterized pixel, the central pixel is connected to the amplifier while the two adjacent pixels are properly biased.

The metallizations on the surface of this sensor does not allow to excite it with the laser except of a very small area. To have access to the whole volume the sensor is excited from the back. To do that the laser light goes through a drilled hole in the PCB and then crosses 350 μm of support wafer before reaching the sensor active area, as shown in Figure 6.14. The laser focusing is done in such a way that the waist of the laser beam is located at about 75 μm under the sensor surface (half depth of the active thickness).

6.4.1 Amplitude measurements

The amplitude measurements allow to obtain information on the charge collection efficiency of silicon detectors. In this case, since the amplifier board is a fast transimpedance amplifier (current follower), the signal response, such as the signal amplitude, is affected by the charge carriers mobility and, as explained in the subsequent paragraphs, this affect the amplitude characterization. Figure 6.15 show an amplitude map of a 3D trench single pixel operated at a bias voltage of -100 V. The amplitude absolute value is not representative of a MIP charge deposition since, exciting the sensor from the back, much of the laser intensity is absorbed before reaching the active volume. Moreover to keep the SNR as high as possible averaged signals are recorded

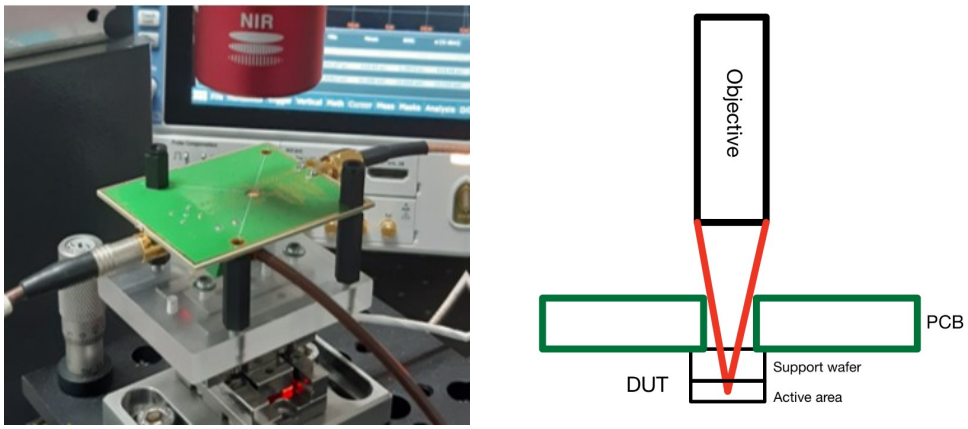

Fig. 6.14 (Left) Picture of the DUT excited from the back. (Right) Scheme of the DUT excitation: the laser beam out from the objective crosses the drilled PCB and 350 μm of silicon support wafer before reaching the focal plane in the middle of the sensor active thickness.

for each excitation position. From the amplitude map it is possible to recognize the characteristic elements that are present in the picture of the sensor. The metallization on the sensor surfaces appears as a higher amplitude region. This is due to the upside down excitation condition that makes the laser light being reflected back again after crossing the detector volume and causing the effect of creating more e-h pairs.

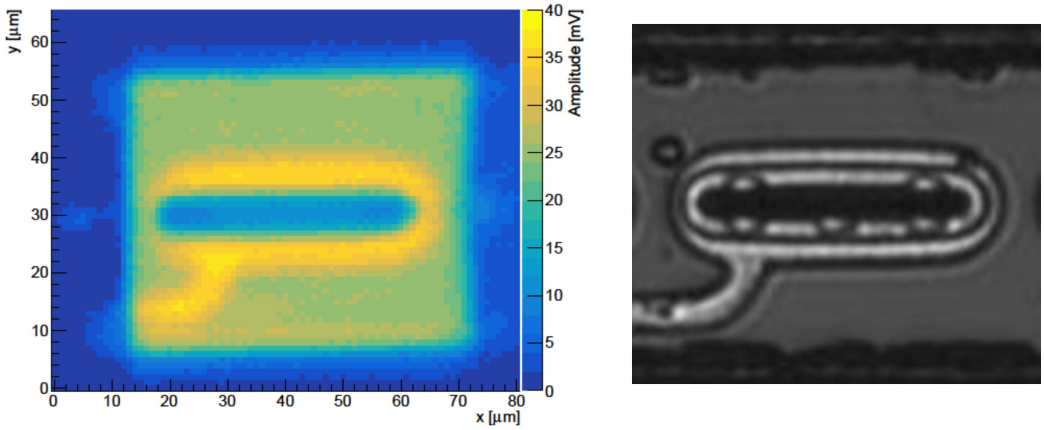

Fig. 6.15 (Left) Amplitude map of a 3D trench pixel biased at -100 V. (Right) Picture of the DUT.

The map shows that the trenches, as expected, are not active volumes, neither the 5 μm $\times$ 40 μm central readout trench nor the two 2.5 μm $\times$ 55 μm biasing trenches. This is more evident looking to the amplitude projections shown in Figure 6.16. The

x projection, made for the points $45\,\mu\text{m} < y < 50\,\mu\text{m}$, shows that the sensor active area is well defined and with the proper dimension of about $55\,\mu m$. However the y projection, from $36\,\mu\text{m} \leq x \leq 46\,\mu\text{m}$, shows that not all the $55\,\mu\text{m}$ length is active and thus gives a first indication on the reduced geometrical efficiency of these devices for normal incident particles detection.

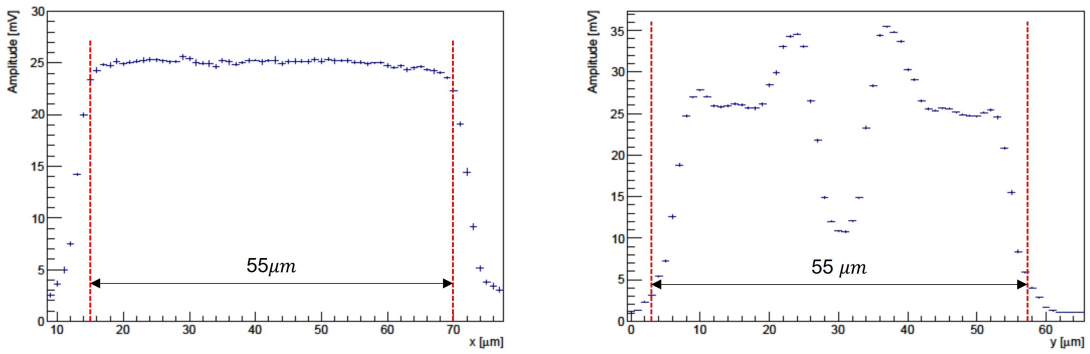

Fig. 6.16 (Left) X projection of the amplitude map of Figure 6.15. (Right) y projection of the region $36\,\mu\text{m} \leq x \leq 46\,\mu\text{m}$.

The sensor charge collection efficiency is evaluated for different bias voltages. The resulting amplitude maps, reported in Figure 6.17, show an amplitude decreasing up to about 20% for -7 V and -15 V. This behaviour is not expected for 3D trench sensor, since the full depletion occurs at about -7 V and so no variation of the amount of collected charge should be measured for bias voltages lower than -7 V. However, since the sensor is connected to a fast transimpedance amplifier, the amplitude measurements are affected by the ballistic deficit. An amplifier with a short shaping time cuts the charges with drift times longer than the shaping time. This causes a reduction of the amplitude of the signal at the output of the preamplifier due to an increasing of the drift time that, as shown in the next section, it depends on sensor bias voltage. This effect is known as ballistic deficit.

The amplitude maps also allows to estimate the fraction of the sensor active area. To do that an amplitude threshold of 20 mV is imposed to the DUT signals. This value represent the 80% of the signal amplitude obtained in a full active zone for a bias voltage of -100 V. An high threshold value is chosen so that the areas in which the laser spot partially intercept the trenches are removed. In fact for those areas the light is transmitted and reflected in an unpredictable way and this could bias the measurements. Table 6.1 shows the fraction of active area obtained for those scans. For a bias voltage of -100 V an active area of $(77 \pm 2)\%$ of the $55 \times 55\,\mu\text{m}^2$ nominal

pixel dimension is measured. Figure 6.18 shows the results obtained for the different bias. A constant active area is found down to -50 V with a rapid decrease for lower magnitude of bias voltage that, also in this case, is caused by the ballistic deficit. It is important to emphasize that the amplifier used for these tests is made to fully exploit the timing capabilities of the 3D trench pixel and so these amplitude measurement do not provide a full representation of the sensor charge collection efficiency.

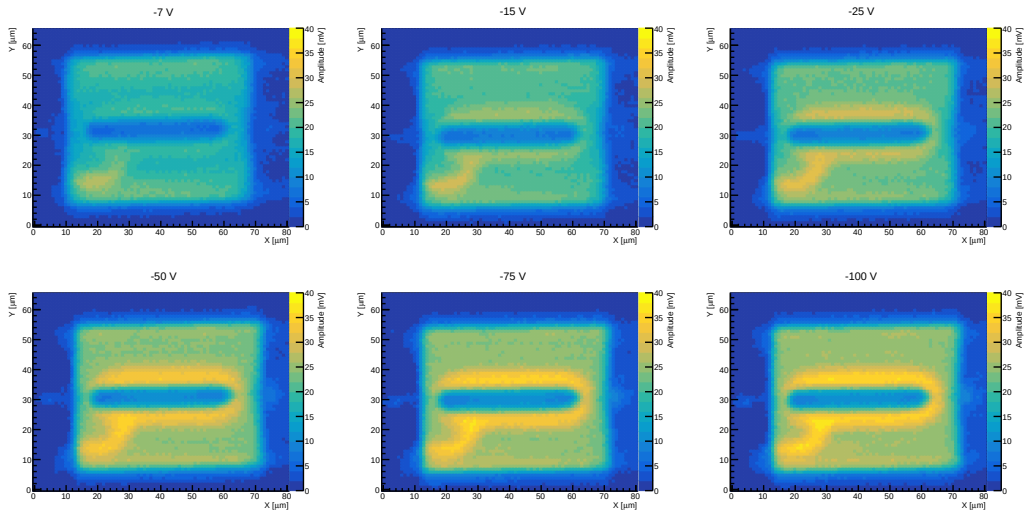

Fig. 6.17 Amplitude maps of the 3D trench sensor for -7 V, -15 V, -25 V, -50 V -75 V and -100 V bias voltages.

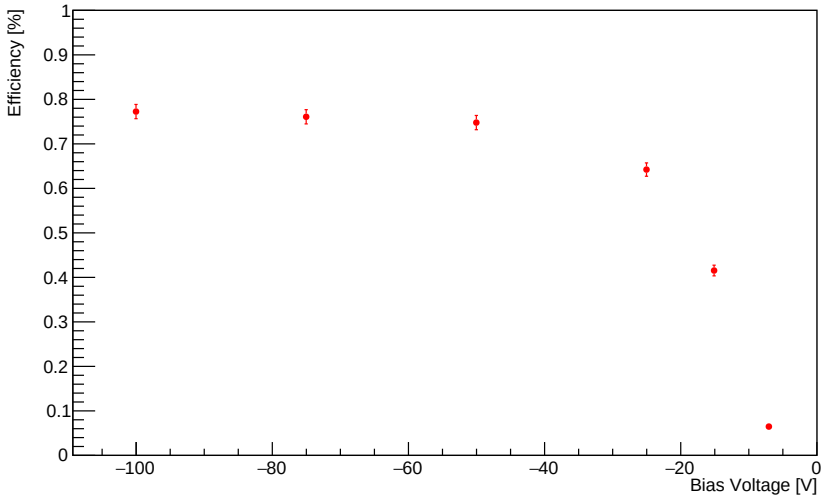

Fig. 6.18 Active area as a function of the bias voltage.

Bias Voltage [V]	Efficiency [%]
-7	6.0 ± 0.5
-15	41 ± 1
-25	64 ± 1
-50	75 ± 2
-75	76 ± 2
-100	77 ± 2

Table 6.1 Fraction of active area requiring an amplitude higher than 80% of 25 mV.

6.4.2 Measurements of timing non-uniformity contribution

The ToA of a particle detected with a 3D sensor, operated at normal incidence, depends on where the particle crosses the sensor. This effect is due to the variation of the shape of the sensor current depending on the excitation position, as described in Section 3.3. The shape variation of the signal depends on the specific electrodes geometry (weighting field) and on the charge carriers drift velocity, which is related to the electric field through the mobility. The ToA variation due to this effect causes a time jitter referred in this text as non-uniformity jitter contribution, σ_{un} (see Section 3.6.1). In this section the ToA variation and the consequent σ_{un} are evaluated for the 3D trench pixel thanks to the laser scans.

To better evaluate the ToA variation it is important to reduce the effect of the electronic jitter (σ_{ej}). This is done by recording averaged waveforms during the scans. This allows to increase the waveforms SNR and so decrease the σ_{ej} contribution. The average of one thousand waveforms are recorded for each excitation position to keep $\sigma_{ej} < 1$ ps. A full laser scan is performed and the ToA of the DUT is measured from the recorded signals. This is estimated, for each position, as the difference between the ToA of the DUT and the precise ToA of the laser pulses given by the reference detector. A CFD at the 20% of the signal amplitude algorithm is used to determine the signals ToA of the 3D trench pixel. Figure 6.19 shows the ToA map for a 3D trench silicon pixel sensor biased at -100 V. From the map it clearly emerges a dependence of the ToA on the laser excitation position. This effect, as predicted, is due to different shapes of the sensor signals that lead to a different time in which the signals reach the imposed amplitude fraction, as can be seen in Figure 6.20. The variation of the pulse shape is due to a different current induced in the detector which, as described in Section 3.3, it depends on the position in which the e-h pairs are generated, on the different mobility of the electrons and holes in silicon but also on variation of electric field and weighting field inside the sensor active volume. All these factors contribute

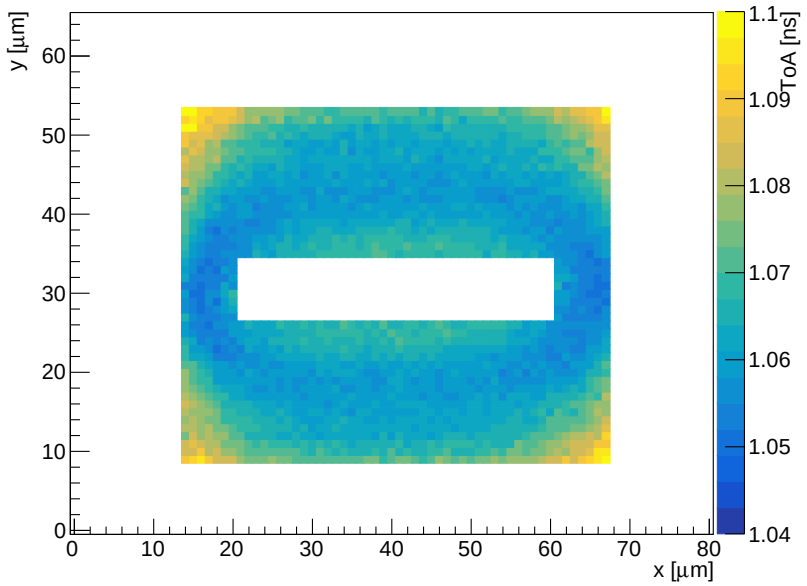

Fig. 6.19 ToA map of a 3D trench pixel operated at a bias voltage of -100 V. The ToAs are obtained from average signals with a 20% CFD algorithm.

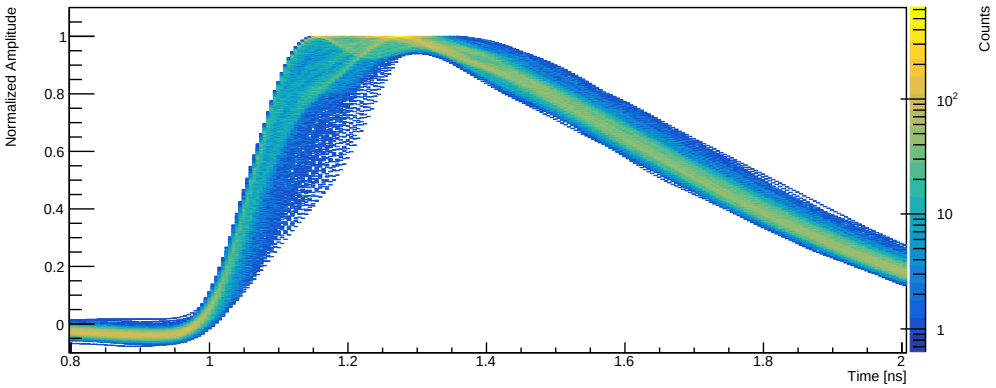

Fig. 6.20 All the normalized signals measured in the laser scan of a 3D trench pixel operated at -100 V. Each signal is the average of 1000 waveforms recorded in a specific excitation position. The figure shows that different signals reach a fixed amplitude fraction at a different time.

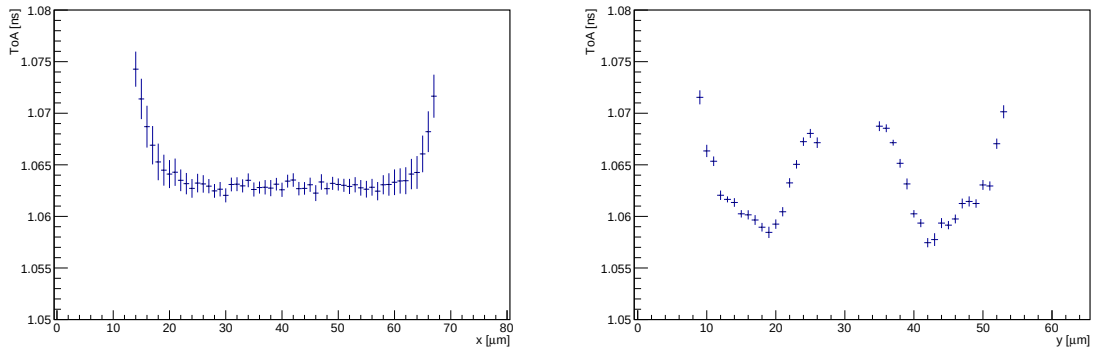

Fig. 6.21 (Left) x projection of the ToA map of Figure 6.19. (Right) y projection of the region $36\,\mu\text{m} \leq x \leq 46\,\mu\text{m}$.

to the variation of signal shape and thus different ToA depending on the excitation positions are measured. The regions in which the signals are the slowest are the four corners, in which the electric field is expected to be lower [74], while the regions with fastest signals is the zone for which both the charge carriers have to travel the minimum distance to reach the electrodes. The x profile of the ToA, reported in Figure 6.21, show that for all the $40\,\mu$m length of the readout electrode ($20\,\mu\text{m} < x < 60\,\mu\text{m}$) the ToA is constant, while outside this region the ToA increases. In the y direction it can be noticed that the minimal ToA is obtained where both the charge carriers have to travel the minimum distance before reach the trenches ($y \sim 18$ μm and $y \sim 44$ μm) and it increases approaching the trenches.

The distribution of the ToA, obtained from the laser scan, is reported in Figure 6.22. A ToA non-uniformity σ_{un} of about 8 ps (RMS) is obtained for the 3D trench silicon pixel sensor. This result represents the intrinsic limit of the time resolutions of a 3D trench silicon pixel sensor for normal incidence particle detection.

Since the timing non-uniformity depend on the sensor electric field several laser scan were made operating the sensor at different bias voltages. The ToA maps of Figure 6.23 show that operate the sensor at higher magnitude of bias voltage reduce the sensor non-uniformity.

The profiles of the ToA maps of Figure 6.24 show a decreasing ToA for higher magnitude of bias voltages. This effect is in agreement with the increasing of the charge carriers drift velocities as the electric field increases. Moreover at lower fields the drift velocities of electron and holes become more different [42] and this increases the timing non-uniformity.

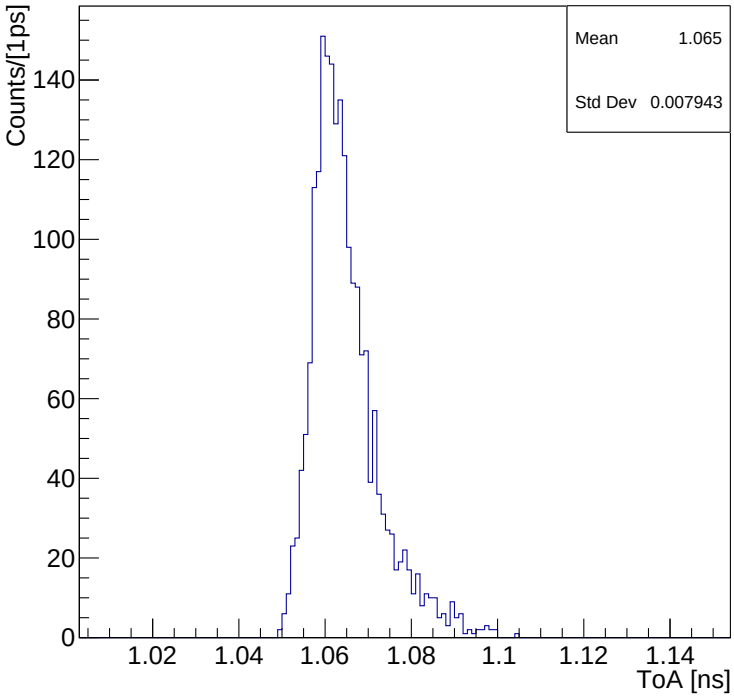

Fig. 6.22 ToA distribution for the 3D trench pixel operated a -100 V. The 8 ps RMS represents the intrinsic time resolution of the sensor. Result obtained with the 20% CFD algorithm.

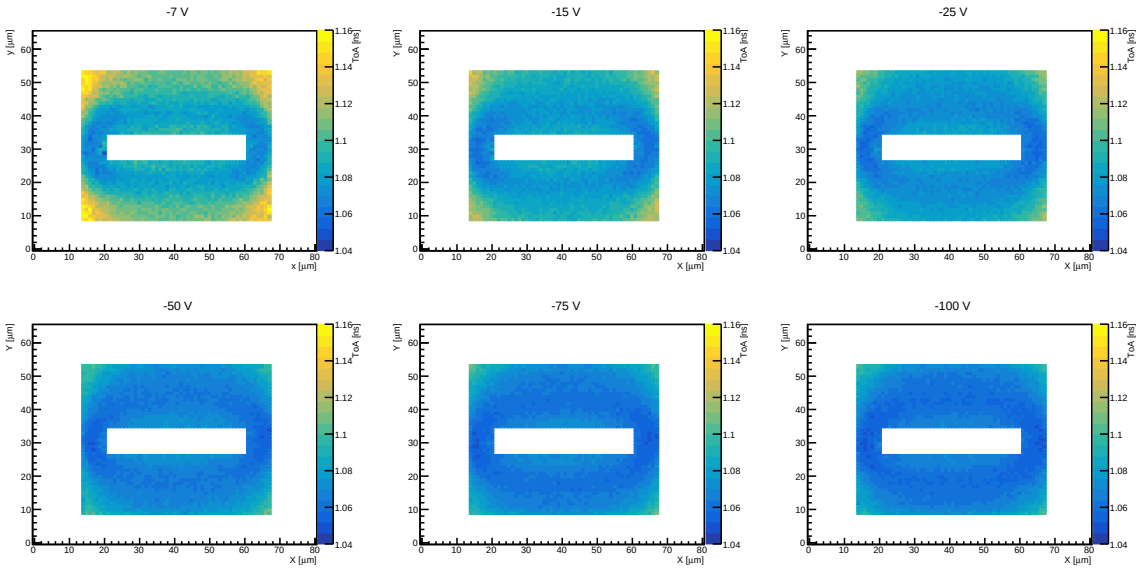

Fig. 6.23 ToA maps of the 3D trench pixel for 6 different bias voltages.

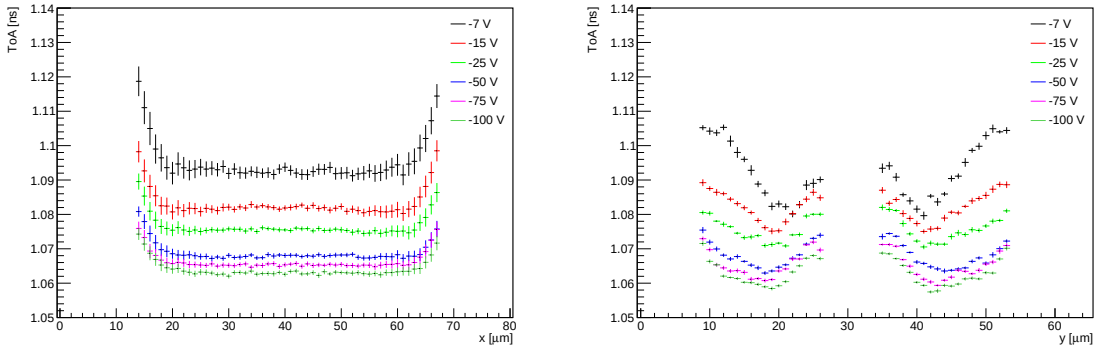

Fig. 6.24 (Left) x projections of the ToA maps of Figure 6.23 for different bias voltages. (Right) y ToA projections of the region $36\,\mu\text{m} \leq x \leq 46\,\mu\text{m}$, for different bias voltages.

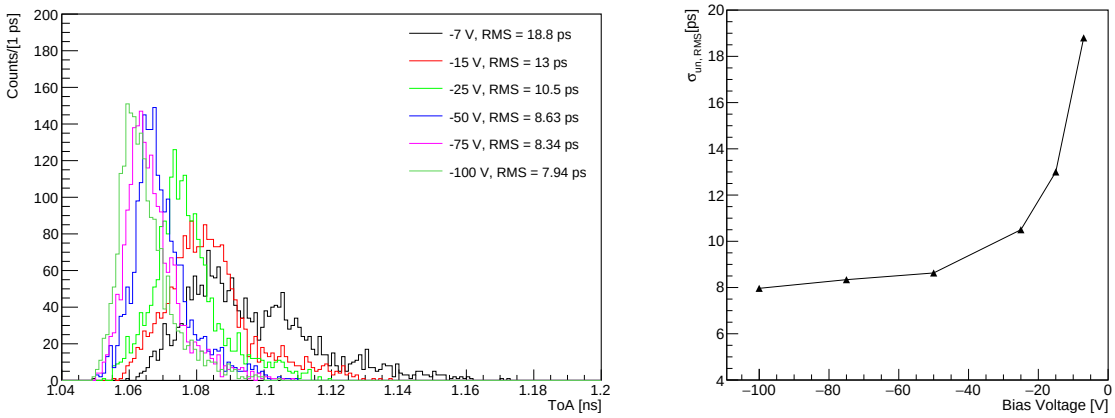

Fig. 6.25 (Left) ToA distributions for the 3D trench pixel for different bias voltages. (Right) Intrinsic time resolution (RMS) as a function of the sensor bias voltage.

This trend is confirmed by the overall ToA distributions, shown in Figure 6.25. The quoted RMS, reported as a function of the bias voltages, show that for bias voltages lower than -50 V the sensor uniformity does not improve significantly while, below that bias, the sensor performances get worse up to 20 ps at -7 V.

The normalized signals of Figure 6.20 also give an indication that different timing performances are achievable by varying the fraction at which the CFD algorithm extracts the ToA. Higher non-uniformity is expected for higher fractions, while a lower threshold allows to trigger when the signals are more uniform. The ToA maps for six different CFD fractions are shown in Figure 6.26.

As expected the sensor looks more uniform for lower CFD fractions. The worst result is obtained, instead, at a CFD fraction of 90% for which the ToA variation is maximum. For that threshold a strong position dependent ToA structure appears. The

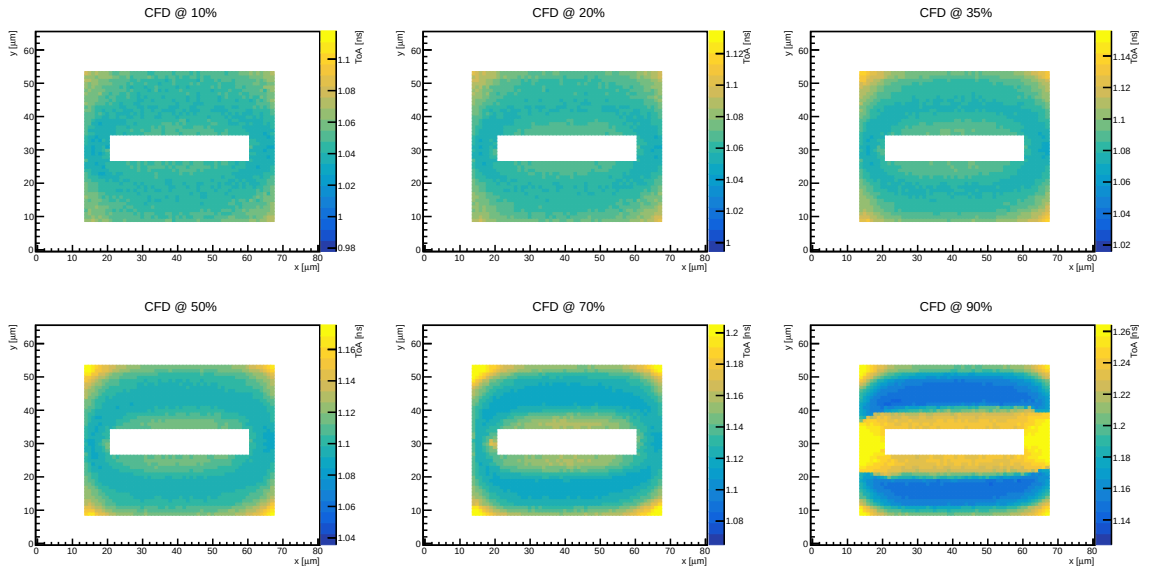

Fig. 6.26 ToA maps of the 3D trench pixel biased at -100 V for six different CFD fractions.

explanation of this is related to the different drift velocities of the two charge carriers, but also on the different contribution that electrons and holes gives to the sensor current depending on the excitation position (see Section 3.3). A detailed simulations of signal formation of 3D trench sensors had already foreseen this behaviour [59]. The ToA overall distributions, reported in Figure 6.27, show that for thresholds higher than 35% a slower contribution appears and become more evident as the CFD fraction increases. This measurement clearly indicate the importance on trigger the signals at the lowest fraction in order to reduce the non-uniformity jitter contribution. However even with a 50% CFD fraction σ_{un} remains below 15 ps.

This study is repeated for different sensor bias voltages and the results are summarized in Figure 6.28. The plot of σ_{un} as a function of the CFD threshold shows that this contribution is under 10 ps for CFD fractions lower than 20% even for bias voltages up to -25 V. Even considering a conservative condition in which the amplitude noise does not allow to trigger below a 50% fraction the non-uniformity jitter contribution remains under 20 ps for sensor bias voltages up to -25 V.

6.4.3 Electronic noise jitter

The laser setup also allows to have information on the other main contribution of a 3D sensor time resolution, the electronic jitter σ_{ej} component. To do that it was important to make negligible the σ_{un} jitter component and to perform the measurements with the

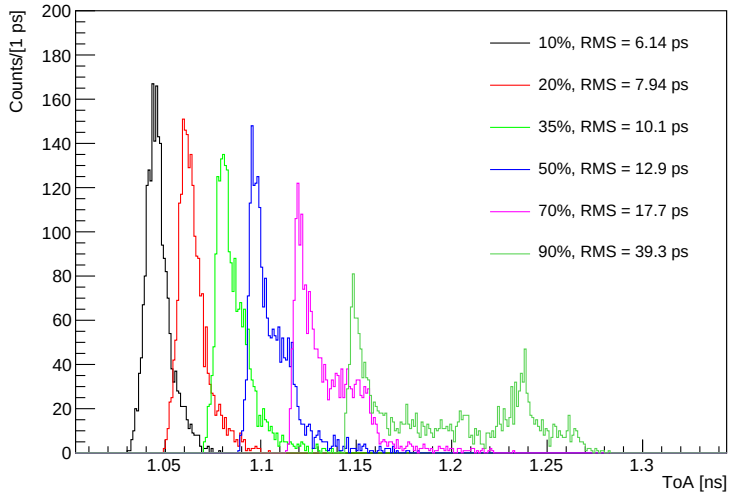

Fig. 6.27 ToA distributions for the 3D trench pixel biased at -100 V for six different CFD fractions.

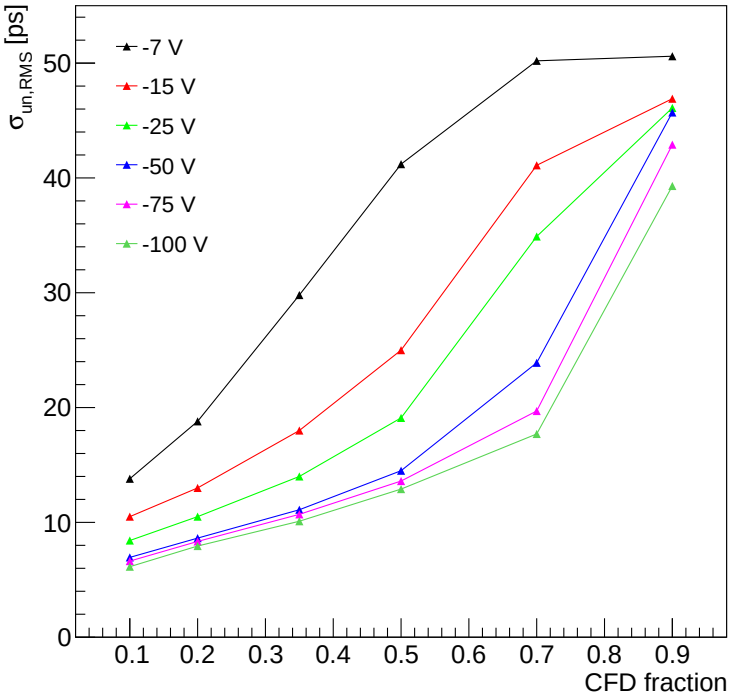

Fig. 6.28 Summary of the intrinsic time resolution of a 3D trench pixel: Intrinsic time resolution as a function of the CFD fraction for different bias voltages.

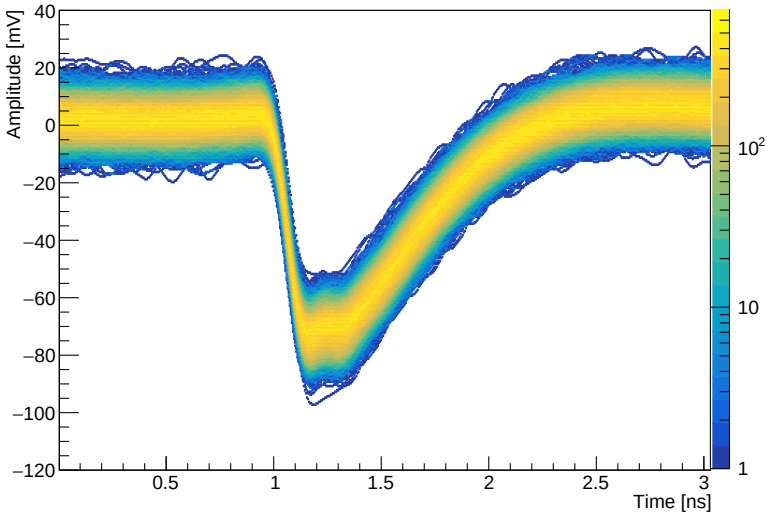

Fig. 6.29 Superposition of 10k signals recorded for the 3D trench pixel operated at -100 V obtained injecting the laser light in a single position.

proper SNR condition (similar to that one of a MIP). For this reason the laser intensity is equalized to that one of a MIP, equivalent to a signal amplitude of about 75 mV corresponding to the most probable value of the Landau distribution of Figure 5.7, measured at the beam test (see Section 5.5.1). The acquisition was switched to single shot signals and 10^4 signals were recorded corresponding to the same laser excitation position, this allowed to make negligible the σ_{un} component. The 10^4 recorded signals are shown in Figure 6.29.

All the signals are analyzed with the CFD algorithm at different CFD fractions. The resulting ToA distributions and the RMS of those distributions, quoted as σ_{ej}, are shown in Figure 6.30.

A value of σ_{ej} of about 6 ps is measured for CFD fractions from 50% to 70%, while an increasing jitter outcomes for lower and higher fractions. This behaviour can be explain considering the variation of the signal slope in its falling edge. In fact the electronic jitter is defined as

$$\sigma_{ej} = \frac{\sigma_{noise}}{|dV/dt|} \text{ [8].} \tag{6.3}$$

A comparison of the measurements to the theoretical equation is shown in Figure 6.31. The theoretical curve is obtained from Equation 6.3 by calculating $|dV/dt|$ at different signal fraction from the average signal of the 10k signals; the value of σ_{noise} is estimated of about 4.7 mV as the RMS of the minimum waveform value of the 10k signals.

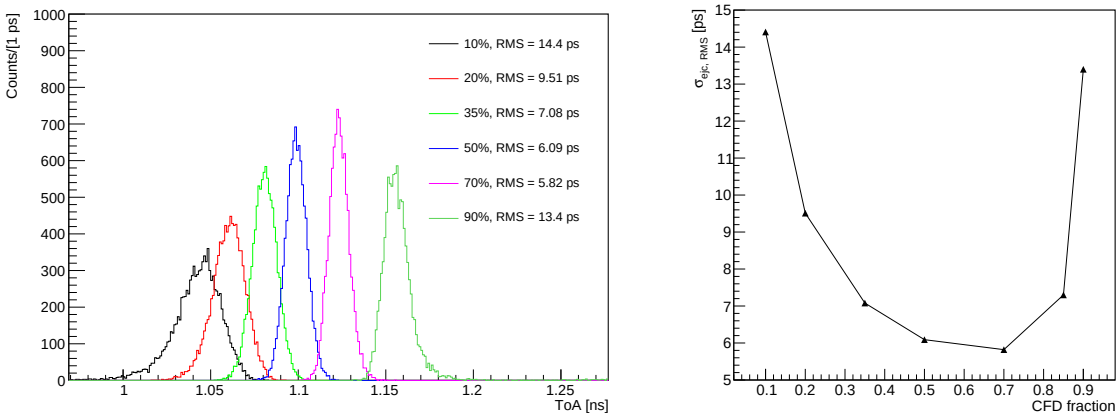

Fig. 6.30 (Left) ToA distributions for the 3D trench pixel for a single excitation position for different CFD fractions. (Right) Electronic jitter component (RMS) as a function of the CFD fraction.

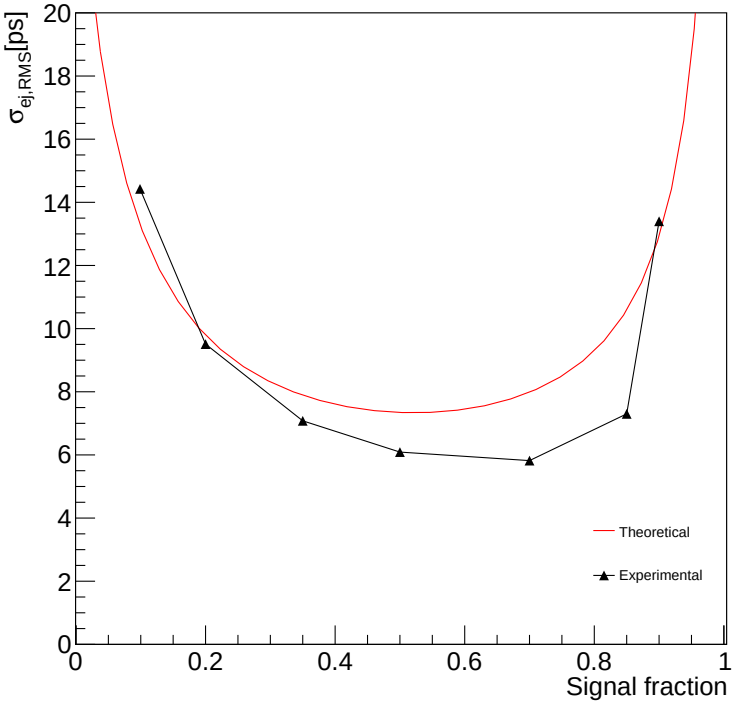

Fig. 6.31 Electronic jitter component as a function of the CFD fraction for the experimental measurements (black) and the theoretical prediction evaluated according to Equation 6.3 (red).

The behaviour of experimental data, even if not in fully agreement are similar to the one of the theoretical jitter which allows to explain that the behaviour of σ_{ej} is related to the signal slope.

This result give also an important indication on the fact that, since the signal shape changes for different excitation positions, a variation of the electronic jitter is expected by exciting the sensor in different position. Unfortunately due to the presence of the metal that cause a variation in the charge deposition, this structure does not allow to make electronic jitter measurements for all the sensor active volume, however repeating the measurements for several excitation positions a maximum degradation of the electronic jitter of about 20% has been found.

6.4.4 Overall time resolution

The measurements of the two main contributions of the time resolution of a 3D trench pixel show that the better results are obtained for different CFD fractions.The minimum σ_{un} is obtained for the lowest CFD fraction while, to minimize σ_{ej}, is better to trigger where the signal reaches its maximum slope. Assuming that the overall time resolution is given by:

$$\sigma_t = \sqrt{\sigma_{un}^2 + \sigma_{ej}^2}, \tag{6.4}$$

an intermediate CFD fraction that minimize σ_t is expected. Figure 6.32 reports the σ_t, calculated according to Equation 6.4 by combining the results of the two independent studies of σ_{un} and σ_{ej}, as a function of the CFD fraction for a bias voltage of -100 V, an overall time resolution of 13 ps is found for a CFD fraction between 20% and 35%.

Another study made with the laser setup is the variation of the timing performances for different amount of deposited charge. While σ_{un} depends only on the sensor geometry and on the electric field, σ_{ej} is expected to decrease if the amount of charge deposited in the detector increases, as it can be seen rewriting Equation 6.3:

$$\sigma_{ej} = \frac{\sigma_{noise}}{|dV/dt|} \sim \frac{t_r}{SNR}. \tag{6.5}$$

If more e-h pairs are created in the sensor a higher SNR is expected and, according to Equation 6.5, σ_{ej} must decreases. To study this effect several waveforms are recorded exciting the sensor in a fix position for different laser intensity. Figure 6.33 show the σ_{ej} measured as a function of the deposited charge, expressed in MIP equivalent. The red line represents the σ_{un} value, previously measured, and the black curve is computed as the squared sum of the two contributions. The results refers to a sensor bias voltage

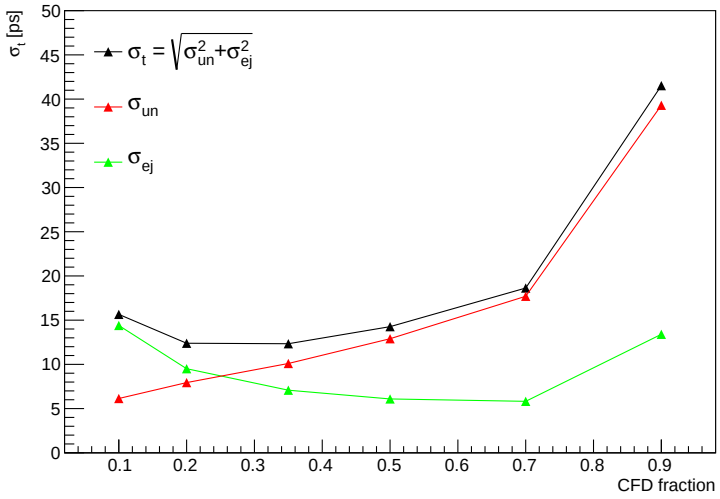

Fig. 6.32 Timing jitter main contributions vs CFD fraction for a 3D trench pixel biased at -100 V: (green) electronic jitter; (red) intrinsic time resolution; (black) overall time resolution.

of -100 V and the CFD fraction is 20%. The measurements show that, as expected, σ_{ej} decreases as the deposited charge increases. For charge depositions higher than 1.3 MIP equivalent the electronic jitter become smaller than σ_{un} until it became negligible at higher charge depositions.

6.5 Trenches vs Columns: the hexagonal geometry

The 3D sensors were first designed with columnar electrodes [45]. The evolving technology of the last years allows to develop different shape of electrodes. To validate the effective benefit of trench electrodes with respect to the more production ready columnar 3D sensors [75], a comparison of their intrinsic timing properties is studied in this section. The tested columnar sensor is a 3D silicon sensor with n++ readout columns and p++ bias columns [76]. The test structure, shown in Figure 6.34, is composed of six p++ columnar electrodes placed at 30 μm distance from the central n++ electrode forming an hexagonal shape. The hexagonal pixel is surrounded by six pixels that have the central electrodes shorted together and forming a guard ring.

The structure is read by the same amplifier board used for the 3D trench sensor. Similarly to the trench sensor a laser scan is performed but in this case, since the metallization covers a smaller region compared to the trench sensor the scan is performed with the laser entering from the sensor top surface. A full scan is performed at a

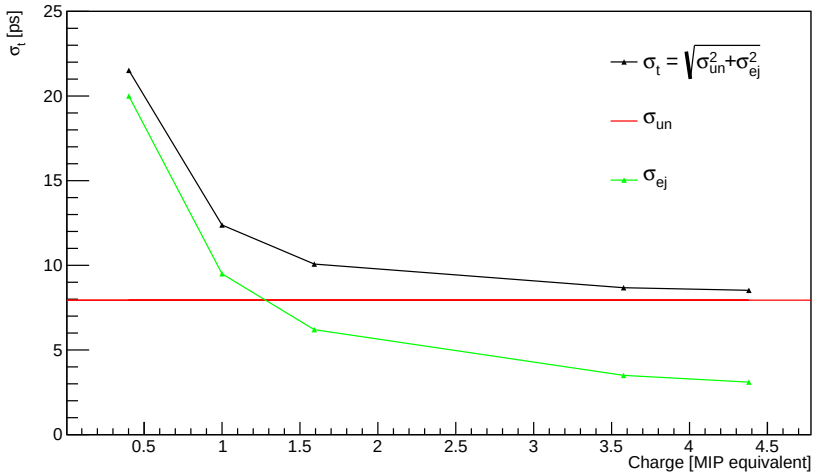

Fig. 6.33 Timing jitter main contributions as a function of the deposited charge expressed in MIP equivalent deposition for a 3D trench pixel biased at -100 V: (green) electronic jitter; (red) intrinsic time resolution; (black) overall time resolution.The time is obtained with a 20% CFD algorithm.

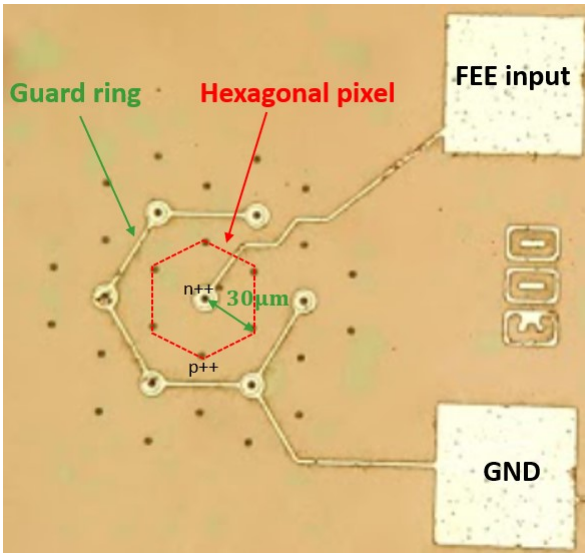

Fig. 6.34 3D hexagonal sensor structure. The hexagonal pixel is formed by a n++ central columnar collection electrode and six p++ columnar biases electrodes. The distance between the central electrode and the biases electrodes is 30 μm

.

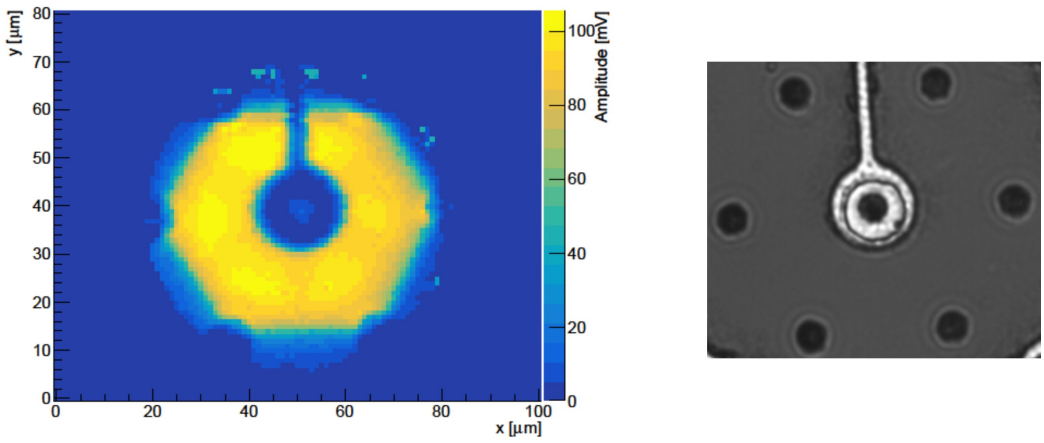

Fig. 6.35 (Left) Amplitude map of a 3D hexagonal pixel biased at -100 V. (Right) Picture of the tested device in scale.

bias voltage of -100 V, also in this case averaged waveforms are recorded in order to make negligible the σ_{ej} contribution. The amplitude map is shown in Figure 6.35, the sensor active area appears uniform in its hexagonal shape and the amplitude drop fast outside the hexagonal perimeter. Not all the sensor active volume is explorable, a small metallization line and a circle with a radius of about 10 μm, that surround the n++ column, blocks the laser light. The ToA map obtained with the laser scan, is compared in Figure 6.36 to the one of the 3D trench pixel studied in the previous sections. The map is obtained with a 50% CFD at a bias voltage of -100 V. The colour scale, for both sensors, is 200 ps wide and shows clearly an higher ToA non-uniformity for the columnar sensor with respect to the trench design. A peculiarity of the hexagonal shape is that while moving away from the central electrode the ToA increases. This effect is likely due to the velocity of the charge carriers, that for this geometry is not uniform on the active volume, but as the electric field, it decreases moving away from the central electrode.

Evaluating the average ToA as a function of the distance from the central column (r), shown in Figure 6.37, a linear dependence of the ToA to r is found with a coefficient of about 8 ps/μm. This feature represents the main limit on the intrinsic time resolution of this device.

Besides the overall timing performances of the hexagonal sensor, the linear dependence of the ToA to the distance of the central column, found for this device, appears very interesting since it opens the way for future developments in which the spatial

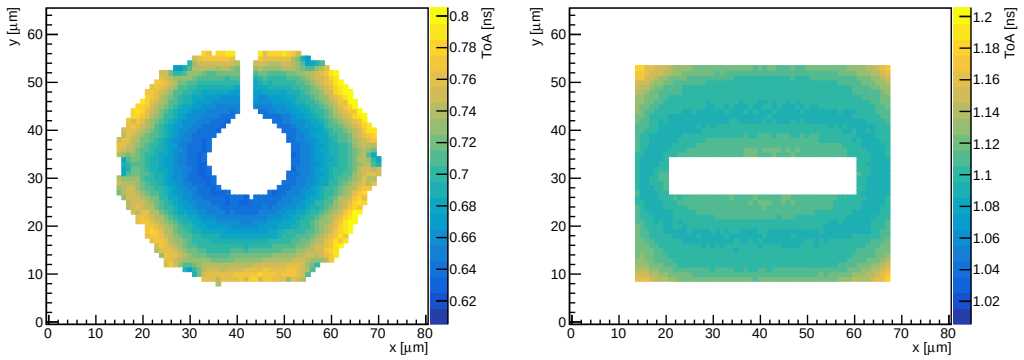

Fig. 6.36 ToA maps for (left) an hexagonal pixel and (right) the 3D trench pixel. For both sensors the bias voltage is -100 V and the ToA are obtained with a 50% CFD. The colour scale for both graphs is 200 ps wide.

resolution of a pixel could be improved by using the strong correlation between r and the ToA.

In conclusion the comparison of the ToA distributions of the columnar hexagonal and the trench pixel is shown in Figure 6.38. It is important to underline that the distributions are obtained with the same amplifier board, at the same bias voltage -100 V, and using the same timestamping algorithm, a 50% CFD. The ToA distribution of the columnar hexagonal pixel is almost flat and 130 ps wide (FWHM), while the trench sensor produces a ToA distribution with a narrow peak. To quantitative compare the intrinsic timing performances of the two pixels the RMS of the two distributions are calculated, obtaining 43 ps for the hexagonal columnar pixel and 13 ps for the 3D trench sensor. These results clearly show the better timing performances of a 3D sensor optimized for timing measurements with respect to a more classic 3D columnar sensor.

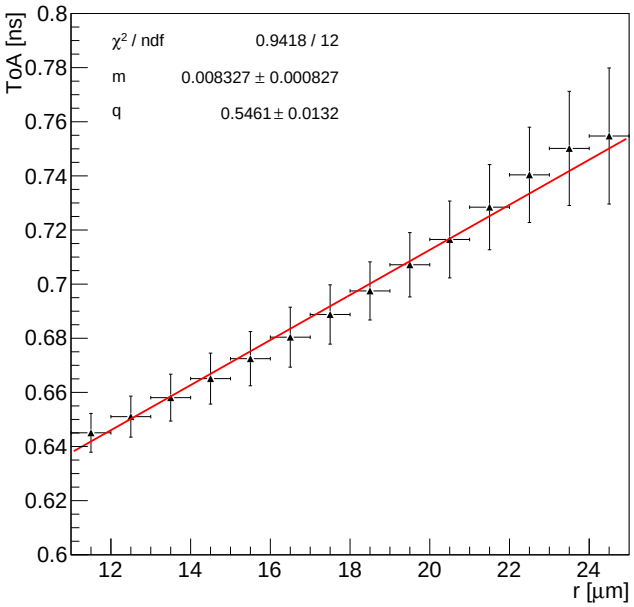

Fig. 6.37 ToA of the map reported in Figure 6.36 as a function of the distance to the central n++ column. A linear fit is performed on the data.

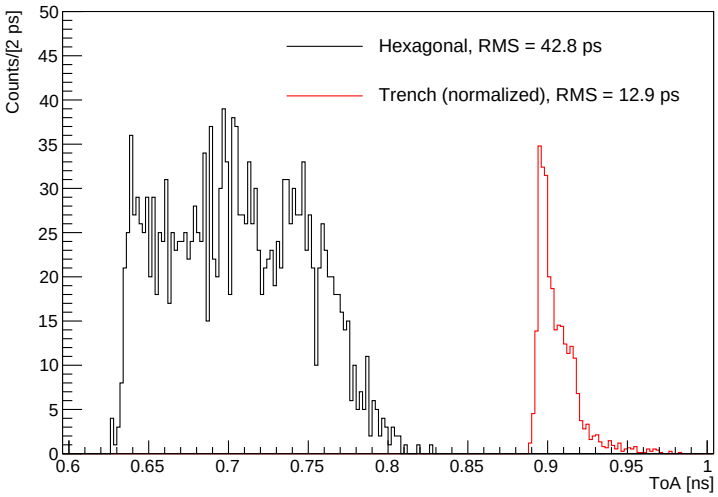

Fig. 6.38 Comparison of the ToA distributions for the 3D hexagonal pixel (black) and the 3D trench pixel (red). The 3D trench pixel distribution is scaled and shifted.

Chapter 7

Highly irradiated TimeSPOT sensors

This chapter describes the beam test measurements carried on in May 2022 at the SPS H8 beam line. The main purpose of these tests is the characterization of the TimeSPOT sensors irradiated at very high fluences, up to $2.5 \cdot 10^{16}\, 1\, MeV\, n_{eq}\, cm^{-2}$. The measurements, reported in the following, are the first timing characterizations of irradiated 3D silicon sensors made in a beam test. They represent an important step forward towards the high luminosity upgrades of LHC experiments and beyond to the Future Circular Collider (FCC) experiments.

7.1 Test structures

The tested devices are 3D trench silicon sensors of the second TimeSPOT production batch. The test structures, shown in Figure 7.1, were irradiated at the TRIGA Mark II Reactor at the Jožef Stefan Institue in Ljubljana, Slovenia [77] at different irradiation fluences:

- Single pixel irradiated at a fluence of $1.0 \cdot 10^{16}\, 1\, MeV\, n_{eq}\, cm^{-2}$;
- Single pixel irradiated at a fluence of $2.5 \cdot 10^{16}\, 1\, MeV\, n_{eq}\, cm^{-2}$;
- Triple pixel-strip irradiated at a fluence of $1.0 \cdot 10^{16}\, 1\, MeV\, n_{eq}\, cm^{-2}$;
- Triple pixel-strip irradiated at a fluence of $2.5 \cdot 10^{16}\, 1\, MeV\, n_{eq}\, cm^{-2}$.

Similarly to what shown for the non irradiated devices, the single pixel structures have been used for the charge collection (amplitude) and timing characterizations while for

the measurements of the detection efficiency triple pixel-strip sensors have been used. The sensors, after the irradiation, were wire bonded to the TimeSPOT single channel amplifier boards, already described in Section 5.2. The wire bonding of the single pixel structures are made in such a way that a central pixel is connected to the amplifier pixel while the two adjacent pixels are connected to ground to guarantee the proper electric field in the outer region of the central pixel. The bias voltage is provided by the front-end board on the back of the sensor, attached to the board by means of a conductive tape. The irradiated sensors, as expected, feature a higher leakage current than the non-irradiated pixels. This is measured at the input of the amplifiers boards and it was of about 40 nA for the $2.5 \cdot 10^{16}\, 1\, MeV\, n_{eq}\, cm^{-2}$ pixel and 20 nA for the $1.0 \cdot 10^{16}\, 1\, MeV\, n_{eq}\, cm^{-2}$ pixel, both operated at a bias voltage of -150 V and at a temperature close to -30° C.

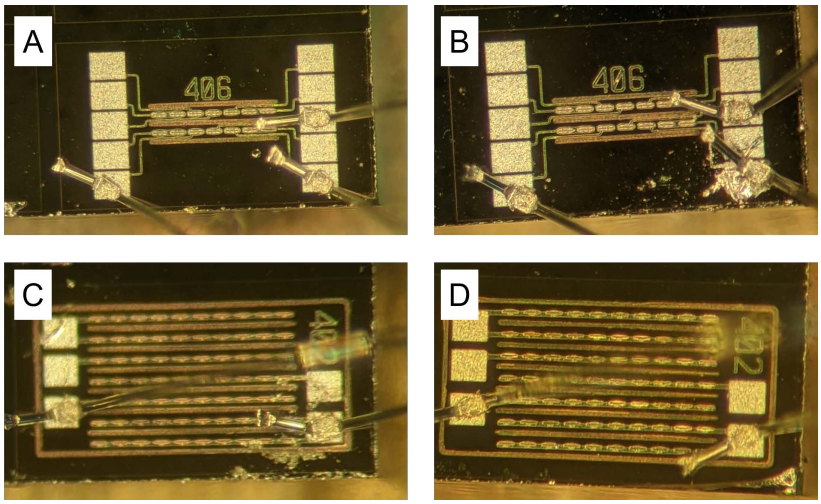

Fig. 7.1 Irradiated test structure. (A) Single pixel irradiated at a fluence of $1.0 \cdot 10^{16}\, 1\, MeV\, n_{eq}\, cm^{-2}$, (B) Single pixel irradiated at a fluence of $2.5 \cdot 10^{16}\, 1\, MeV\, n_{eq}\, cm^{-2}$, (C) Triple pixel-strip irradiated at a fluence of $1.0 \cdot 10^{16}\, 1\, MeV\, n_{eq}\, cm^{-2}$, (D) Triple pixel-strip irradiated at a fluence of $2.5 \cdot 10^{16}\, 1\, MeV\, n_{eq}\, cm^{-2}$.

7.2 The setup

The irradiated sensors were tested at the SPS H8 beam line with a 180 GeV/c positive pion beam. The setup is very similar to the one used for the previous beam test (see Section 5.3). Two MCP-PMT detectors are used as a time reference for the Time of Arrival (ToA) of the pions and two 3D trench sensors are fine aligned together along

the beam line. An accurate setup description is reported in Section 5.3, while in the following the improvements required for the test of the irradiated sensors are reported.

Due to the radiation damage, irradiated silicon sensors must be operated at low temperature, typically -20°, in order to reduce the leakage current. To ensure a low temperature operation to the sensor the setup of the previous beam test has been upgraded. The DUT is located at the center of the black box, shown in Figure 7.2, between two 3D printed plastic containers. The containers are used to carry the dry ice used to low down the sensor temperature. The thermal isolation is ensured by means of a polystirene box that covers the DUT and the containers. A PT100 sensor is used to monitor the temperature of the DUT during the acquisitions. This system allowed to assure data acquisition runs with a sensor temperature range from -40° C to -20° C. The data acquisition consists on the recording of the sensor and MCP-PMTs waveforms by means of a high bandwidth oscilloscope. The acquisition trigger condition is made by triggering on the AND of one of the two MCP-PMTs and of a single pixel sensor placed upstream to the DUT (see Figure 7.2). The alignment procedures and the oscilloscope used for the waveforms acquisitions are the same of the previous beam test and are reported in Section 5.3.1.

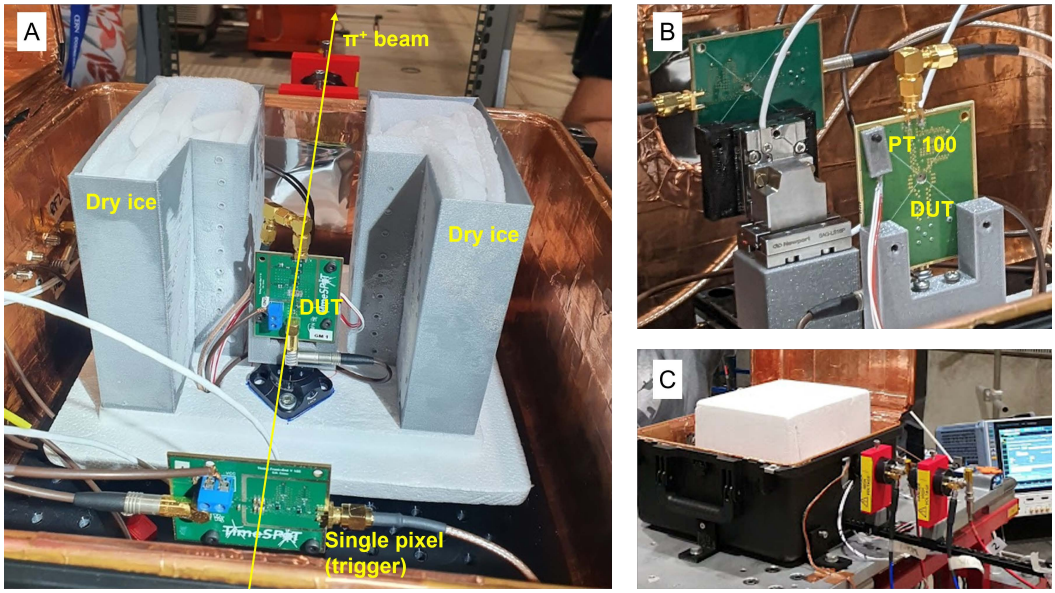

Fig. 7.2 Pictures of the beam test setup. (A) Two sensor aligned,the DUT is placed between two dry ice containers used for the cooling. (B) Back view of the two 3D trench devices in which the PT100 sensor is visible. (C) The DUT is thermally isolated from the outside by means of a polystirene box, the MCP-PMTs used as a time reference detectors are also visible in the picture.

7.3 Results

This section reports the characterizations of the irradiated TimeSpot 3D trench sensors. The results are obtained by means of algorithms capable to extract the informations from the silicon sensors and MCP-PMTs waveforms, recorded by the oscilloscope. In particular for the amplitude and the timing performances a single pixels sensors is used, while for the efficiency measurement the DUT were triple pixel-strip sensors. The algorithms used to analyze the sensors and MCP-PMTs waveforms have been optimized in the previous beam tests and are described in detail in Section 5.4 and Section 5.6 for the timing and efficiency methods, respectively.

7.3.1 Amplitude measurements

Radiation generates traps on the sensor silicon that traps the charge carriers and thus have the effect of reduce the charge collection efficiency of irradiated sensors. Typically the charge collection performances of irradiated silicon sensors are restored by increasing the sensor absolute bias voltage. This effect is studied for the irradiated 3D trench pixels by means of several acquisitions at different values of the DUT bias voltages. Similarly to the former beam test, since the DUT's signals are not part of the trigger, all the sensor signals are recorded. Figure 7.3 shows the amplitude distributions obtained at different sensor bias voltages (HV) for the single pixels irradiated at $1.0 \cdot 10^{16}\, 1\, MeV\, n_{eq}\, cm^{-2}$ and $2.5 \cdot 10^{16}\, 1\, MeV\, n_{eq}\, cm^{-2}$ which are compared to the measurements of the non-irradiated pixel of Chapter 5. Comparing the distributions it can be noticed that, differently to the non-irradiated pixel, both the irradiated sensors present a lowering of the amplitude most probable value when the magnitude of the bias voltage is decreased. Since the amplifier boards used for the irradiated sensors have a slightly different gain, a quantitative comparison of the amplitude values can not be done. However what emerges clearly from the distributions is that the $2.5 \cdot 10^{16}\, 1\, MeV\, n_{eq}\, cm^{-2}$ pixel have similar performances of the non-irradiated sensor when a bias voltages slightly lower than -100 V is applied. A similar behaviour was found for the $1.0 \cdot 10^{16}\, 1\, MeV\, n_{eq}\, cm^{-2}$ pixel which seems to reach a stable amplitude distribution already from -100 V. These studies show that 3D trench sensors survive to those very high fluences and good amplitude distributions can still be obtained by operating irradiated sensors at a bias voltage of about -100 V. Moreover the fact that the irradiated pixels at the highest fluence shows similar performances of the non-irradiated pixel is an evidence that the limit of 3D trench radiation hardness has not been reached yet.

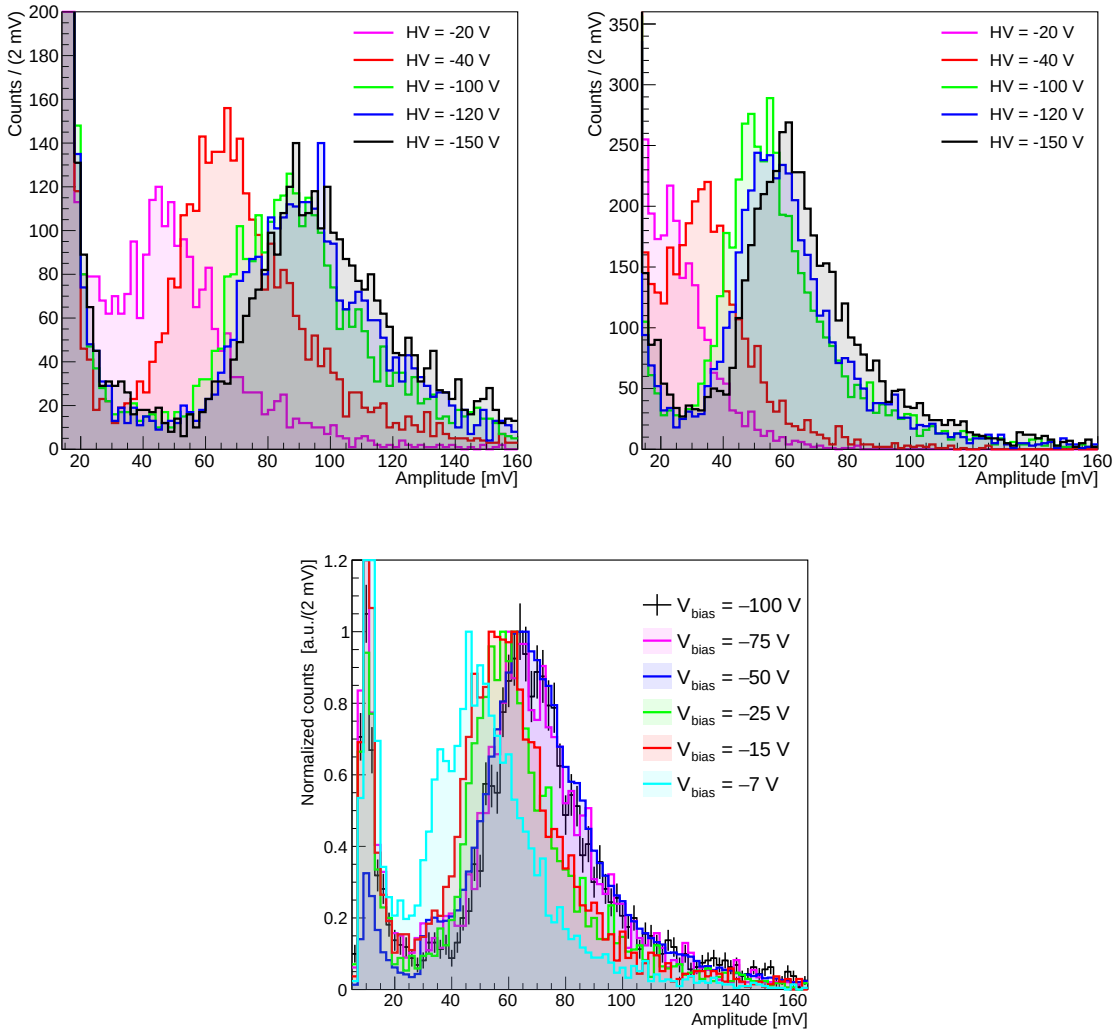

Fig. 7.3 Amplitude distributions of 3D trench single pixels for different bias voltage operation at irradiation fluences of: (top left) $1.0 \cdot 10^{16}\,1\,MeV\,n_{eq}\,cm^{-2}$, (top right) $2.5 \cdot 10^{16}\,1\,MeV\,n_{eq}\,cm^{-2}$, (bottom) non-irradiated.

7.3.2 Time resolution

The measurements of the time resolution of irradiated 3D sensors are evaluated for the first time, in a beam test campaign, in this work. The time resolution is evaluated by applying the Reference and the Spline algorithms, already used and described in Section 5.4, to the waveforms. Also in this case, the time of the tested sensor (t_{Si}) is evaluated with respect to the pion time of arrival that is given by the average time of the two MCP-PMTs signals ($\langle t_{\mathrm{MCP-PMTs}} \rangle$). Figure 7.4 shows the distributions of $t_{Si} - \langle t_{\mathrm{MCP-PMTs}} \rangle$ for the two irradiated pixels obtained with the Reference method for a bias voltage of -150 V. The two distributions are very similar and presents the

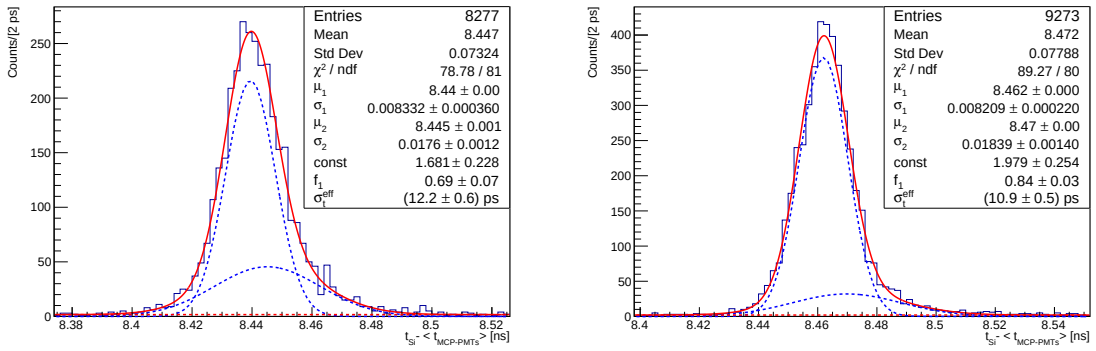

Fig. 7.4 Distributions of the time difference between the 3D trench single pixel and the time reference for $V_{\mathrm{bias}} = -150$ V with the *reference* method for (Left) the $1.0 \cdot 10^{16}\, 1\, MeV\, n_{eq}\, cm^{-2}$ pixel and (Right) the $2.5 \cdot 10^{16}\, 1\, MeV\, n_{eq}\, cm^{-2}$ pixel. The distributions are fit with the sum of two Gaussian functions (blue dashed lines) describing the signal, and a constant (red dashed line) modelling the background.

same features of the one of the non-irradiated pixel (see Figure 5.9): a narrow peak with a small tale of late signals. To obtain the time resolution a two Gaussian fit function is imposed to the time distributions and the standard deviation, σ_t^{eff}, of the distribution is evaluated according to Equation 5.2 (for a detailed description of the standard deviation estimation see Section 5.5.2). These steps are done for several acquisition runs in which the irradiated sensors were operated at several bias voltages and, for each run, the time resolutions σ_t^{Si} of the 3D trench pixels are computed by subtracting in quadrature the MCP-MPTs average time resolution $\sigma_{MCP-PMTs}$ to σ_t^{eff}. Figure 7.5 shows the obtained values of σ_t^{Si} as a function of the sensor bias voltage for the two irradiated pixel and for the non-irradiated pixel (operated at room temperature), studied in the Chapter 5 of this thesis. Both the results obtained with the reference and the spline methods are reported. The curves obtained for both

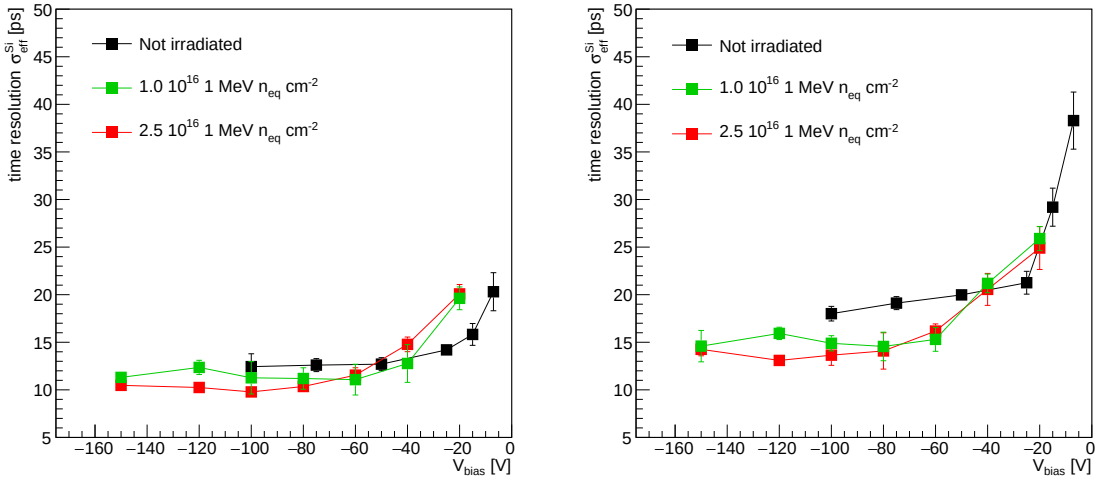

Fig. 7.5 Time resolution of the single pixels as a function of the bias voltage for the different irradiation fluences obtained with the (left) reference method, (right) spline method. The contribution due to the resolution of the time reference is subtracted. Not irradiated pixel operated at room temperature.

methods show that the irradiated sensors have very similar timing performances to the non-irradiated pixel. The time resolution obtained with the reference method at a bias voltage of -100 V are 9.8 ± 0.4 ps for the $2.5 \cdot 10^{16}\, 1\, MeV\, n_{eq}\, cm^{-2}$ pixel and 11.3 ± 0.7 ps for the $1.0 \cdot 10^{16}\, 1\, MeV\, n_{eq}\, cm^{-2}$ pixel to be compared to the 12.4 ± 1.3 ps of the non-irradiated sensor operated at the same bias voltage. These results clearly show that the time resolution of 3D trench sensor is not affected by the radiation damage, at least for the considered fluences. The obtained values, despite are very similar, seems to show a slightly improvement of the timing performances of the irradiated sensors, but since they are very close, this effect could be faked by small different performances of the front-end electronic boards used for the different sensors and by the fact that the not-irradiated sensor is operated at room temperature. This is a very small effect that, if present, would requires more dedicated studies to be understood. The curves also show that despite the time resolution of the non-irradiated sensor does not improve significantly for bias voltages lower than -25 V, the irradiated sensors reach this condition for higher magnitude of bias voltage that is of about -60 V for the $1.0 \cdot 10^{16}\, 1\, MeV\, n_{eq}\, cm^{-2}$ and about -80 V for the $2.5 \cdot 10^{16}\, 1\, MeV\, n_{eq}\, cm^{-2}$. This effect could be related to the amplitude decreasing of the irradiated sensors when operated at lower absolute bias voltages, that leads to an increasing timing jitter.

The time resolution of the $2.5 \cdot 10^{16}\,1\,MeV\,n_{eq}\,cm^{-2}$ pixel is also evaluated when operated at a tilt angle of 20° with respect to the normal beam operation. This was done since, as shown in Chapter 5, 3D trench sensors achieve a 99% efficiency only if operated with a tilt angle higher than 10° with respect to the normal incidence. The results, reported in Table 7.1, show that also the irradiated sensor features a small increasing in time resolution when operated at 20° passing from 9.8 ± 0.4 ps to 13.5 ± 0.6 ps with the reference method and for a bias voltage of -100 V. The results presented in this section clearly show that 3D trench sensors have comparable timing performances of the non-irradiated pixels and this make them one of the best candidate for the sensor technology of high luminosity LHCb vertex locator detector.

Table 7.1 Time resolution for non irradiated and irradiated 3D trench pixels operated at different tilt angles. The sensors were operated at a bias voltage of -100 V.

Fluence	σ_t^{Si} (Reference) [ps]		σ_t^{Si} (Spline) [ps]	
	0°	20°	0°	20°
Non irradiated	12.44 ± 1.4	17.5 ± 0.9	17.84 ± 1.0	21.66 ± 0.9
$2.5 \cdot 10^{16}\,1\,\mathrm{MeV\,n_{eq}\,cm^{-2}}$	9.8 ± 0.4	13.5 ± 0.6	13.6 ± 1.1	16.9 ± 0.9

7.3.3 Detection efficiency

In order to measure the detection efficiency of 3D trench irradiated sensors a 3D trench single pixel is aligned to the DUT, that in this case is a 3D trench triple-strip structure. This configuration allows to estimate the efficiency as $\eta = N_{ts}/N_{tr}$, where N_{ts} is the number of events detected by the triple-strip sensor and N_{tr} is the number of trigger (number of particles that geometrically cross the triple-strip sensor), the methodology used for the evaluation of N_{ts} and N_{tr} is the same of the previous beam test campaign and is reported in Section 5.6. Several acquisition runs are performed for the irradiated triple-strip sensor operating the DUT at various tilt-angle. The results reported in Figure 7.6(right) show that the $2.5 \cdot 10^{16}\,1\,MeV\,n_{eq}\,cm^{-2}$ triple-strip have a compatible efficiency to the non-irradiated sensor. In fact also the irradiated sensor reaches a 99% detection efficiency when tilted at higher angles than 10 degrees. The reported measurements are obtained for a bias voltage of -130 V and -100 V for the irradiated and non-irradiated sensors, respectively. For the triple strip irradiated at a fluence of $1.0 \cdot 10^{16}\,1\,MeV\,n_{eq}\,cm^{-2}$ the efficiency is studied only for normal beam incidence (0 degrees) but for different bias voltages. The results, reported in Figure 7.6(left), show that while the efficiency of the non-irradiated sensor do not depend on the bias voltage

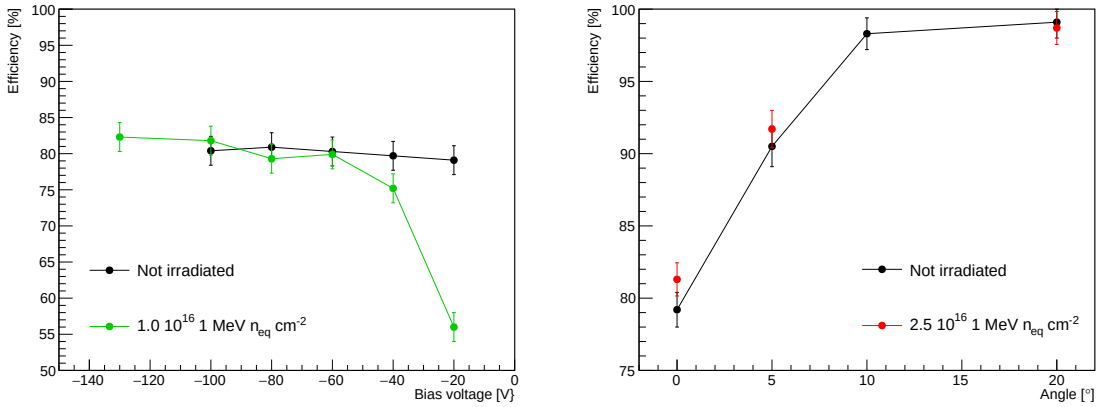

Fig. 7.6 (Left) Detection efficiency versus the bias voltage for the irradiated and non-irradiated 3D trench sensors operated at normal beam incidence condition. (Right) Detection efficiency versus tilt angle for the irradiated and non-irradiated 3D trench sensor operated at a bias voltages of -130 V and -100 V, respectively.

for the irradiated sensor a significant drop of efficiency is found for a magnitude bias voltage below -60 V.

7.4 Summary

The results shown in this chapter have proven a time resolution of about 10 ps and a detection efficiency close to 99% for the 3D trench silicon sensors irradiated to a fluence up to $2.5 \cdot 10^{16}\, 1\, MeV\, n_{eq}\, cm^{-2}$. The amplitude distributions, the time resolutions and the efficiency of the irradiated sensors operated at a different bias voltages give a clear indication that irradiated 3D trench sensors recovers the same performances of the non-irradiated ones by increasing the magnitude of bias voltage less than 50 V with respect to the normal operation. Finally the measurements have also shown that the limit of radiation hardness of these sensors have not yet been reached at the tested fluences.

These results prove that 3D trench sensors are one of the best candidate for 4D tracking detectors operated at very high fluences in high energy physics experiments.

Chapter 8

Design studies for tracking charged B mesons

In the other chapters of this thesis the technological sensors developments for the realization of a future vertex locator detector that will allow the LHCb experiment to continue its heavy flavour physics program has been shown. However, the implementation of new methods for the reconstruction of B mesons decays which were considered unfeasible up to now at LHCb will allow to expand the LHCb physics programs. Theses methods also give new tools to better exploit the increased luminosity starting from Run 3 and even more after the LHCb high luminosity upgrade.

In this chapter the feasibility studies of a new method which aims to directly track charged B mesons for the first time by exploiting the LHCb VELO detector are shown. Several VELO geometries have been simulated to evaluate the performances of this method even in future upgrade LHCb scenarios.

8.1 Introduction

The physics of heavy flavours, particularly of b-hadrons, is a fantastic probe for our understanding of the fundamental interactions, specifically of the violation of Charge-Parity (CP) symmetry or searches for new phenomena in rare decays. The study of partially reconstructed b-hadron final states poses challenges that limit the sensitivity with respect to fully reconstructed ones. This is particularly true at hadron colliders where there is no possibility of closing the kinematics without information from the initial state, or where reconstructing the opposite side b-hadron would severely limit the statistics. In particular, for charged B mesons (B^+ or B_c^+) some final states present minimal information reconstructible at experiments such as only one charged track

and one or no calorimetric deposit from neutral particles. Among these are rare decays such as $B^+ \to \tau^+\nu_\tau$, sensitive to extensions of the Standard Model with charged heavy particles, or CP sensitive decays such as $B^+ \to \pi^+\pi^0$. Increasing the yield and/or background suppression of these and other partially reconstructed decays can enhance the performances of several experiments as well as opening new ways of looking for new physics.

In the next sections a new method is proposed to search for partially reconstructed decays of charged b-hadrons, by tracking the hadron before its decay in detectors placed very close to the hadron production vertex. Given the typical lifetime of B^+ and B_c^+ decays [78], when produced in high energy collisions, their boost allows them to fly up to few centimeters before decaying. Few of these mesons therefore are able to reach two or more tracking stations. The reconstructed track segment can be found and used to constrain the direction, and thus the momentum of the parent B^+ meson. This in turn can open the road to a new set of measurements or improve their precision, such as semileptonic and other partially reconstructed decays. The proposed method is viable also at hadron colliders, where these measurements were typically thought to be infeasible [79], although it is not limited to them. The VELO detector is used as an example, however the method is more general and not limited to the LHCb experiment. The use of tracks of long living particles, that is charged strange hadrons, in the LHCb experiment was discussed in [80]. There the hadron would fly up to one meter and transverse the whole VELO detector. Standard tracking was exploited and connected to the decay vertex. Here it is proposed to exploit down to a single energy deposit (hit) in the tracking detectors to improve the background rejection and kinematic reconstruction of charged B decays. This can improve: the identification of the relevant primary vertex among many, the direction of the B^+ momentum, the background rejection from neutral B decays. It is also considered the cases from one to three or more deposits, and the efficiency to reach those stations for different realistic geometry configurations is evaluated.

8.2 Tracking close to the particle collision

The proposed method relies on tracking detectors very close to the interaction point were the B hadrons are produced. Such subdetectors are present in recent particle physics experiments [81], [82] and [83], to identify and distinguish the primary vertices, track and find displaced particles and improve tracking performances. In this work the (VELO) [84] detector of the LHCb experiment and its current and future upgrades are

considered as a benchmark of the proposed method. However results can be applied to any detector with similar distance to the interaction point with minor changes.

The detailed descriptions of the Run 1/2 and Run 3/4 VELO detectors are reported in Section 1.4. The method takes advantages of the close distance of the VELO sensors from the beam-line, which is 8 mm (5.1 mm) in Run 1/2 (Run 3/4), thus the typical radial distance of the first hit of a charged particle decreases from 10 mm to about 6 mm. The distance between two consecutive stations is of 3 cm (2.5 cm) in Run 1/2 (Run 3/4), as shown in the following this is a major parameter to optimise this method.

In the following it is considered a tracking detector with this configuration, identifying 2D coordinates of particles at fixed z distances regardless of the hardware technology that allows this.

8.3 Event generation

Proton-proton collisions are generated with Pythia [85], and decays of B mesons are generated with EvtGen [86]. A sample of 4 million pp collisions at 13 TeV, with $B^+ \to J/\psi K^+$ decays in the LHCb acceptance is generated and used as benchmark for these studies.

Only events where the K^+ meson and the two muons produced in the decay of the J/ψ meson are inside the LHCb acceptance are considered in this work. These particles are required to be in a pseudorapidity range of $2 < \eta < 5$. The kinematics variables of the generated particles are reported in Figure 8.1 for reference.

8.4 Geometries description

This study has the goal of proving the feasibility to directly track B^+ and B_c^+ mesons using a tracking detector very close to the interaction region. Five different geometries are considered, all of them are built with a custom C++ code, two examples of the built geometries are shown in Figure 8.2. Each detector configuration is composed of several identical tracking stations, for the studied geometries four type of tracking stations are considered. In order to simplify the geometries the stations are simulated with an infinitesimal thickness since the sensor thickness is negligible with respect to the typical B^+ flight distances considered.

Different designs of the LHCb Vertex Locator detector, both past and future, are taken. This study covers both the former VELO used in Run 1 and 2 between 2010 and 2018 (VELO Run 1/2), the new VELO detector based on silicon pixel technology,

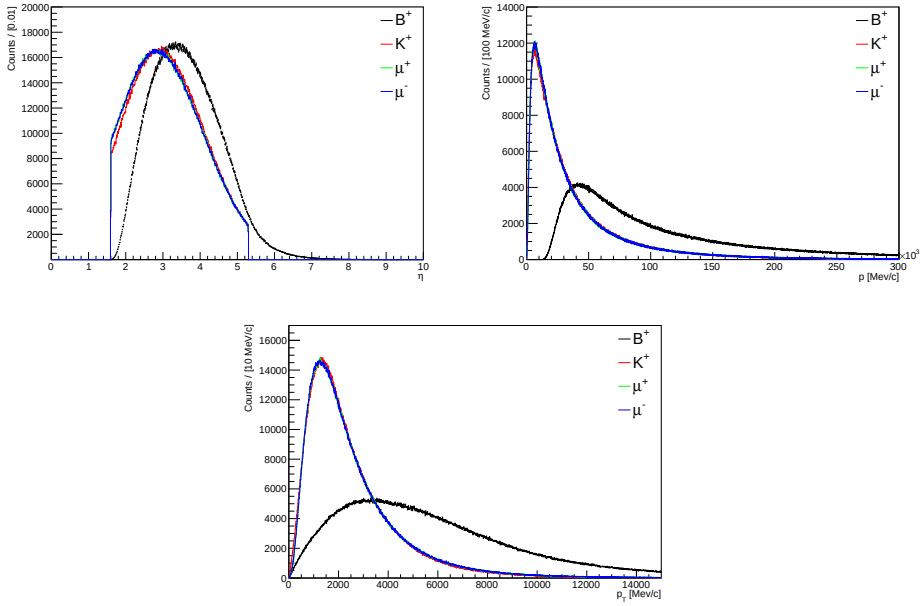

Fig. 8.1 Kinematics variables of all the generated particles. (Top Left) Pseudorapidity;(Top Right) Momentum; (Bottom) Tansverse Momentum

installed for Run 3 and Run 4 (Run 3/4), but also new scenarios that are being considered in view of future LHCb upgrades. The Run 1/2 geometry is composed of 42 tracking stations. The stations are parallel to the beam direction and spaced at a distance of 30 mm. Each tracking station is a semi-circle with a radius of 42 mm. The inner 8.2 mm radius semi-circle is not sensitive.

The Run 3/4 geometry has 52 equal tracking stations transverse to the beam direction and spaced 25 mm from each other. Each tracking station has an L shaped sensitive area consisting of two adjacent rectangles of 42.57 mm × 28 mm. The detector sensitive areas are placed at 5.1 mm from the beam line.

This first two geometries are a representation of two existing detectors; three more geometries were developed to test the method in different conditions. Two of them try to maximise the method performance during possible LHC Run 5 and 6 scenarios, and one is similar to the proposed detector in the LHCb Upgrade II FTDR [20].

The *Closer* geometry is equal to the Run 3/4 one but with a reduced distance from the beam line from 5.1 mm to 4 mm. This distance is chosen such that the radiation damage to the innermost sensors is equal to $1 \cdot 10^{17}$ 1 MeV $n_{eq}cm^{-2}$, that is the highest radiation damage of current silicon 3D pixel sensors [28], one of the sensor technology candidates for the new LHCb VELO detector after the upgrade II.

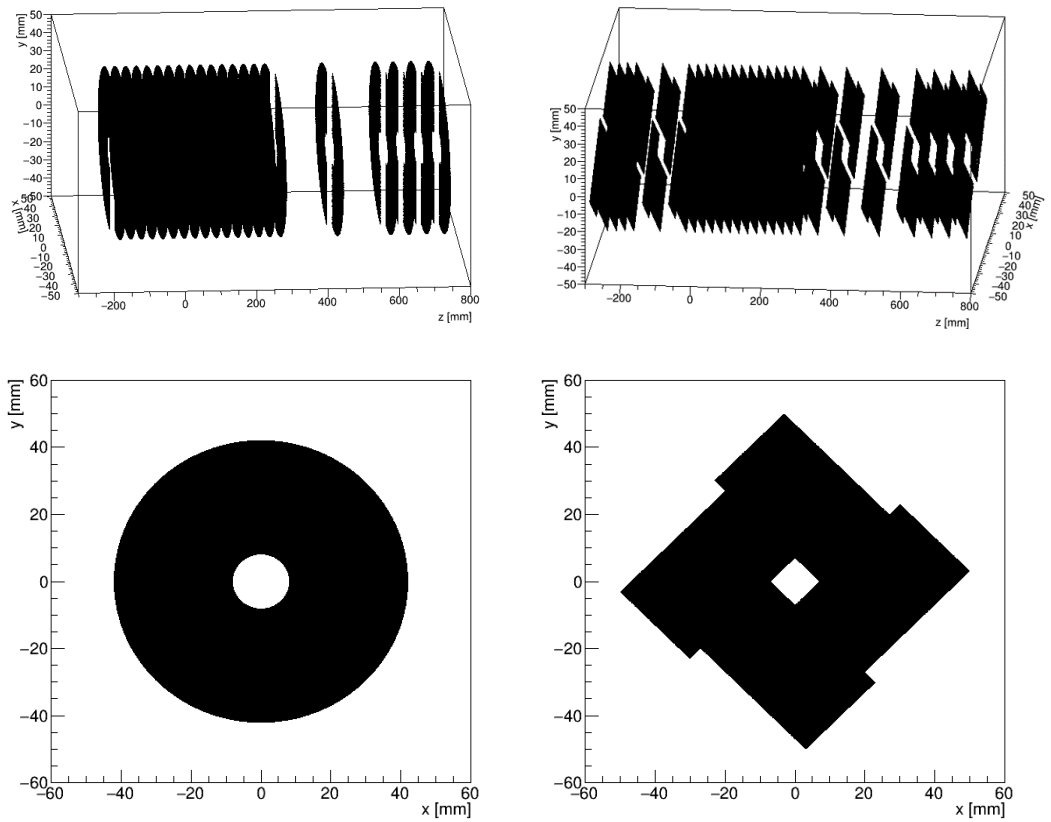

Fig. 8.2 Examples of the simulated geometries.(Left) Run 1/2 VELO; (Right) Run 3/4 VELO.

The *B scenario* is a geometry presented in the LHCB FTDR [20] for the upgrade II that is similar to the Run 3/4 VELO geometry but with an increased distance from the beam line up to 12.5 mm.

The last simulated geometry is named *Double*, and consists of a Run 3/4 geometry but with double the number of stations, so that the distance between the active planes is reduced from 25 mm to 12.5 mm.

A summary of the considered geometries with their characteristics is shown in Table 8.1.

Table 8.1 Geometry configuration of the considered detectors

Name	Geometry	Distance between stations	Distance to beam line
Run 1/2	Semi-circular	30.0 mm	8.2 mm
Run 3/4	L shape	25.0 mm	5.1 mm
Run 5/6 Closer	L shape	25.0 mm	4.0 mm
Run 5/6 Double	L shape	12.5 mm	5.1 mm
Run 5/6 B Scenario	L shape	25.0 mm	12.5 mm

Considering each of the detector geometries, the stations crossed by the B^+ between production and decay vertices are counted. The detecting efficiency of a station in its active area is assumed to be 100%, which is very similar to the one in real operating conditions. A sub-sample of the generated events as tracked in the Run 3/4 geometry is shown in Figure 8.3, it can be seen that a significant portion of the B^+ mesons crosses more than one station before decaying. From the number of deposits of the B^+ mesons in the tracking stations it is possible to estimate the fraction of B^+ that can be tracked and reconstructed according to conditions defined below. A B^+ meson is considered tracked if it intercepts at least 2 tracking stations, albeit a proper track is typically obtained by at least three hits. However one can consider the possibility that even just one hit, together with the information of the primary vertex, can be used to enhance the reconstruction of decays with open kinematics.

8.5 Results

The fractions of the B^+ mesons that intercept one or more detector stations are shown in Table 8.2. More than 1 per mil of the mesons have at least 1 hit in the Run 3/4 configuration, and $2.4 \cdot 10^{-4}$ have 3 ore more deposits. Other geometry configurations show that moving closer to the beam line and decreasing the distance between planes increases the efficiency as expected by meson decay length. The two Run 5/6 Closer

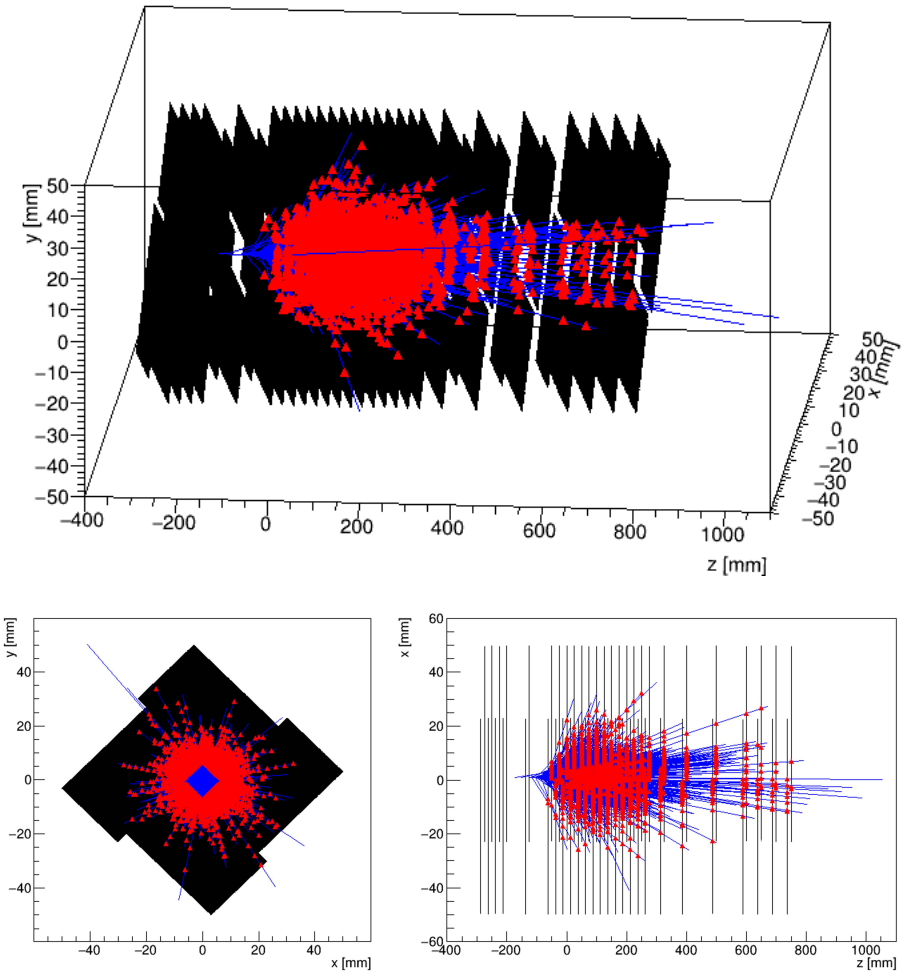

Fig. 8.3 Sample of simulated B^+ mesons in proton-proton collisions at 13 TeV traversing at least two detecting stations in the Run 3/4 geometry. Blue lines represent the paths of the mesons before decaying, red dots represent energy deposits.

Table 8.2 Fraction of B^+ that release one or more hits for the studied Vertex Locator geometries

Geometry	B^+ fraction		
	≥ 1 hit	≥ 2 hits	≥ 3 hits
Run 1/2	$(4.5 \pm 0.1) \cdot 10^{-4}$	$(1.28 \pm 0.06) \cdot 10^{-4}$	$(5.0 \pm 0.4) \cdot 10^{-5}$
Run 3/4	$(1.80 \pm 0.02) \cdot 10^{-3}$	$(5.3 \pm 0.1) \cdot 10^{-4}$	$(2.36 \pm 0.08) \cdot 10^{-4}$
Run 5/6 Closer	$(3.77 \pm 0.03) \cdot 10^{-3}$	$(1.11 \pm 0.02) \cdot 10^{-3}$	$(4.8 \pm 0.1) \cdot 10^{-4}$
Run 5/6 Double	$(2.41 \pm 0.02) \cdot 10^{-3}$	$(1.15 \pm 0.02) \cdot 10^{-3}$	$(6.4 \pm 0.2) \cdot 10^{-4}$
Run 5/6 B Scenario	$(7.1 \pm 0.4) \cdot 10^{-5}$	$(2.6 \pm 0.3) \cdot 10^{-5}$	$(1.1 \pm 0.2) \cdot 10^{-5}$

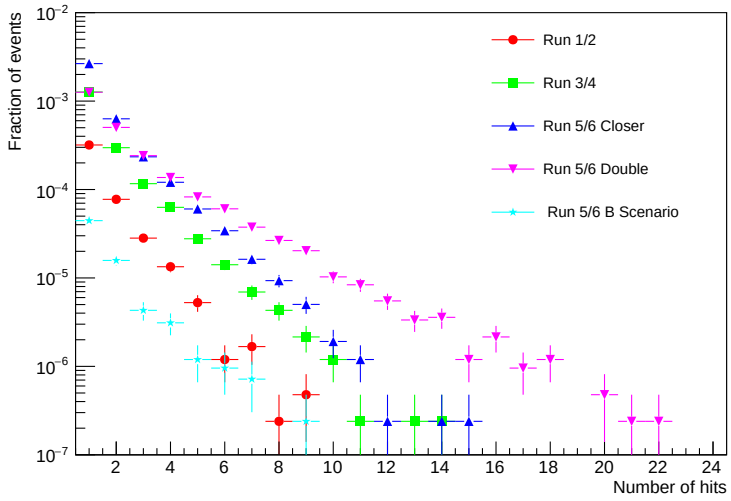

Fig. 8.4 Fraction of B^+ mesons as a function of the number of hits released for the different geometry configurations.

and Double geometries allow to increase the fraction of B^+ that can be tracked by a factor two. Reducing the spacing between tracking station increases significantly the number of events in which B^+ release more than two hits, as shown in Figure 8.4. The B scenario, having a larger distance, appears to be instead more disadvantaged even compared to the old Run 1/2 geometry. In Figure 8.5 the flight distance, meson lifetime and meson momentum are shown before and after requiring that the B^+ meson left two hits in the tracking stations, in the different geometries. As expected most of the reconstructed B^+ mesons have long lifetime and/or high boost due to momentum. These are however also characteristics that improve the trigger and selection efficiencies of a B^+ decay analysis, hence the combine effect will be better than the simple efficiency product, enhancing these kind of decays.

The results of these first studies clearly show that directly track charged B mesons seems feasible at LHCb with the VELO detector. More studies need to be done before this goal is achieved. However, the results obtained for the Run 3/4 VELO geometry and for the Run 5/6 future scenarios are very promising for the implementation of the proposed method.

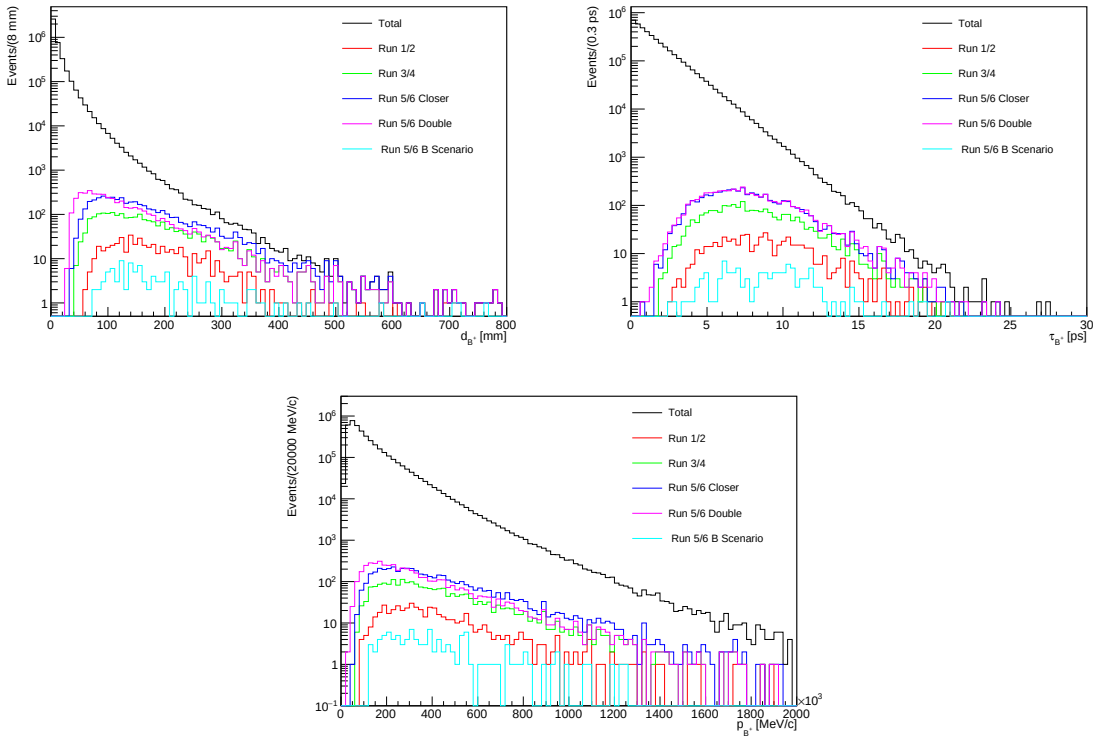

Fig. 8.5 Kinematics variables of B^+ mesons that release at least two hits on the detector stations for the different geometry configurations: (Top Left) Flight distance; (Top Right) Lifetime; (Bottom) Momentum.

Conclusions

In this thesis a comprehensive characterization of the innovative 3D trench silicon pixel sensors is presented. These sensors, developed by the TimeSPOT collaboration, have been proved to be a valid candidate to operate in the future high luminosity vertex locator detector of LHCb, after its second upgrade. Results from three beam tests for the accurate characterization of 3D trench sensors with charged particles are reported in this thesis. In the first beam test sensors from the first TimeSPOT batch were tested, allowing to achieve in 2019 the world record results of 20 ps time resolution for MIP detection with silicon pixel sensors. A detailed simulation was performed to better understand the results obtained at the beam test, proving that the measured time resolution was dominated by both the type of test structured used, not fully representative of a single 3D trench pixel, and by the readout electronic board, giving hints that better timing performances were achievable by these sensors. After the second production batch a new readout electronic board, optimized for the TimeSPOT sensors, was also developed and a second beam test campaign was carried on in 2021 at the SPS H8 beam-line. There for the first time, the efficiency of a 3D trench sensors was measured, proving that, similarly to other 3D sensors, trench sensors obtain a 99% efficiency when operated with an angle slightly larger than 10 degrees with respect to the normal incidence. The timing performances of a single 3D trench pixel were shown to be of about 10 ps obtained with CFD-based method and close to 25 ps when a simple Leading Edge method is used for the timing discrimination. An infrared laser based setup for Transient-Current-Techniques with micrometric spatial accuracy and capable to perform timing characterization with an accuracy of 900 fs is presented. This setup was used to study the non-uniformity timing contribution and the electronic noise jitter of a 3D trench sensor. The comparison of the timing performances of a 3D trench pixel, a sensor optimized for timing performances, and a production-ready technology such as a columnar 3D sensor shows that the optimization of the electrodes layout allows to improve the timing performances of a standard 3D sensor more than a factor 3. The beam test of May 2022 concludes the characterization of the 3D trench

sensors for which their radiation hardness was proven. The results show that irradiated sensors up to $2.5 \cdot 10^{16}\, 1\, MeV\, n_{eq}\, cm^{-2}$ fluence have performances compatible to those of non-irradiated sensors both in terms of time resolution and detection efficiency, if the magnitude of the bias voltage is increased of few tens of Volts. Finally the results of the first design studies for the development of a B tracking method clearly show that directly track charged B mesons seems feasible at LHCb with the VELO detector. Further studies have to be done in order to see the real benefits of the presented method in several decay channels but the results obtained for the Run 3/4 VELO geometry and for some of the Run 5/6 future scenarios are very promising for the development of the proposed method. The work of this thesis mainly focuses on the studies of 3D trench sensors. The obtained results clearly show that 3D trench sensors are a viable solution with high spatial and temporal accuracy which can withstand the high luminosity of LHCb upgrade. Before this work, the focus of the detector developer community was totally on the sensor R&D but, after these studies, it is clear that the focus must now be moved on the sensors readout electronics which, in addition to radiation hardness, timing and spatial resolution have also to take into account the limited power budget and the extremely high data rate that will be present in the high luminosity condition.

References

[1] Ewa Lopienska. The CERN accelerator complex, layout in 2022. Complexe des accélérateurs du CERN en janvier 2022. 2022. General Photo.

[2] Christian Elsässer. $\bar{b}b$ production angle plots.

[3] V. Coco et al. Velo Upgrade Module Nomenclature. Technical report, CERN, Geneva, 2019.

[4] R. Aaij et al. Expression of Interest for a Phase-II LHCb Upgrade: Opportunities in flavour physics, and beyond, in the HL-LHC era. Technical report, CERN, Geneva, 2017.

[5] C. Patrignani. Review of particle physics. *Chinese Physics C*, 40(10):100001, oct 2016.

[6] Michael Moll. *Radiation damage in silicon particle detectors: Microscopic defects and macroscopic properties*. PhD thesis, Hamburg U., 1999.

[7] Renate Wunstorf. A Systematic investigation of the radiation hardness of silicon detectors for high-energy physics experiments. Other thesis, 10 1992.

[8] William R. Leo. *Timing Methods and Systems*, pages 325–334. Springer Berlin Heidelberg, Berlin, Heidelberg, 1994.

[9] N. Cartiglia, R. Arcidiacono, B. Baldassarri, M. Boscardin, F. Cenna, G. Dellacasa, G.-F. Dalla Betta, M. Ferrero, V. Fadeyev, Z. Galloway, S. Garbolino, H. Grabas, V. Monaco, M. Obertino, L. Pancheri, G. Paternoster, A. Rivetti, M. Rolo, R. Sacchi, H. Sadrozinski, A. Seiden, V. Sola, A. Solano, A. Staiano, F. Ravera, and A. Zatserklyaniy. Tracking in 4 dimensions. *Nuclear Instruments and Methods in Physics Research Section A: Accelerators, Spectrometers, Detectors and Associated Equipment*, 845:47–51, 2017. Proceedings of the Vienna Conference on Instrumentation 2016.

[10] A. Loi, A. Contu, and A. Lai. Timing optimisation and analysis in the design of 3d silicon sensors: the TCoDe simulator. *Journal of Instrumentation*, 16(02):P02011–P02011, feb 2021.

[11] L. Paolozzi, M. Munker, R. Cardella, M. Milanesio, Y. Gurimskaya, F. Martinelli, A. Picardi, H. RÃ¼cker, A. Trusch, P. Valerio, F. Cadoux, R. Cardarelli, S. DÃ©bieux, Y. Favre, C.A. Fenoglio, D. Ferrere, S. Gonzalez-Sevilla, R. Kotitsa, C. Magliocca, T. Moretti, M. Nessi, A. Pizarro Medina, J. Sabater Iglesias, J. Saidi,

M. Vicente Barreto Pinto, S. Zambito, and G. Iacobucci. Picosecond avalanche detector â€" working principle and gain measurement with a proof-of-concept prototype. *Journal of Instrumentation*, 17(10):P10032, oct 2022.

[12] Martin A. Green and Mark J. Keevers. Optical properties of intrinsic silicon at 300 k. *Progress in Photovoltaics: Research and Applications*, 3(3):189–192, 1995.

[13] Lyndon Evans and Philip Bryant. Lhc machine. *Journal of Instrumentation*, 3(08):S08001, aug 2008.

[14] K. Aamodt et al. The ALICE experiment at the CERN LHC. *JINST*, 3:S08002, 2008.

[15] G Aad et al. The atlas experiment at the cern large hadron collider. *Journal of Instrumentation*, 3(08):S08003, aug 2008.

[16] S. Chatrchyan et al. The CMS Experiment at the CERN LHC. *JINST*, 3:S08004, 2008.

[17] A Augusto Alves Jr et al. The lhcb detector at the lhc. *Journal of Instrumentation*, 3(08):S08005, aug 2008.

[18] L. Rossi. LHC Upgrade Plans: Options and Strategy. page TUYA02, 2011.

[19] O. Aberle. *High-Luminosity Large Hadron Collider (HL-LHC): Technical design report*. CERN Yellow Reports: Monographs. CERN, Geneva, 2020.

[20] CERN (Meyrin) LHCb Collaboration. Framework TDR for the LHCb Upgrade II - Opportunities in flavour physics, and beyond, in the HL-LHC era . Technical report, CERN, Geneva, 2021.

[21] I. Bediaga et al. Framework TDR for the LHCb Upgrade: Technical Design Report. Technical report, 2012.

[22] Johannes Albrecht et al. Luminosity scenarios for LHCb Upgrade II. 2019.

[23] A. Lai, L. Anderlini, M. Aresti, A. Bizzeti, A. Cardini, G.-F. Dalla Betta, G.T. Forcolin, M. Garau, A. Lampis, A. Loi, C. Lucarelli, R. Mendicino, R. Mulargia, M. Obertino, E. Robutti, and S. Vecchi. First results of the timespot project on developments on fast sensors for future vertex detectors. *Nuclear Instruments and Methods in Physics Research Section A: Accelerators, Spectrometers, Detectors and Associated Equipment*, 981:164491, 2020.

[24] Apollinari G., Béjar Alonso I., Brüning O., Fessia P., Lamont M., Rossi L., and Tavian L. *High-Luminosity Large Hadron Collider (HL-LHC): Technical Design Report V. 0.1*. CERN Yellow Reports: Monographs. CERN, Geneva, 2017.

[25] Technical Design Report for the ATLAS Inner Tracker Pixel Detector. Technical report, CERN, Geneva, 2017.

[26] The Phase-2 Upgrade of the CMS Tracker. Technical report, CERN, Geneva, 2017.

[27] Falaphel fast links and rad-hard front end with integrated photonics and electronics for physics.

[28] Maria Manna, Chiara Grieco, Sebastian Grinstein, Salvador Hidalgo, Giulio Pellegrini, David Quirion, and Stefano Terzo. First characterisation of 3D pixel detectors irradiated at extreme fluences. *Nucl. Instrum. Meth. A*, 979:164458, 2020.

[29] Sherwood Parker, Angela Kok, Christopher Kenney, Pierre Jarron, Jasmine Hasi, Matthieu Despeisse, Cinzia Da Vià, and Giovanni Anelli. Increased speed: 3d silicon sensors; fast current amplifiers. *IEEE Transactions on Nuclear Science*, 58(2):404–417, 2011.

[30] M. Lozano, G. Pellegrini, C. Fleta, C. Loderer, J.M. Rafi, M. Ullan, F. Campabadal, C. Martinez, M. Key, G. Casse, and P. Allport. Comparison of radiation hardness of p-in-n, n-in-n, and n-in-p silicon pad detectors. *IEEE Transactions on Nuclear Science*, 52(5):1468–1473, 2005.

[31] X. Llopart, R. Ballabriga, M. Campbell, L. Tlustos, and W. Wong. Timepix, a 65k programmable pixel readout chip for arrival time, energy and/or photon counting measurements. *Nuclear Instruments and Methods in Physics Research Section A: Accelerators, Spectrometers, Detectors and Associated Equipment*, 581(1):485–494, 2007. VCI 2007.

[32] Franz Laermer, Sami Franssila, Lauri Sainiemi, and Kai Kolari. Chapter 21 - deep reactive ion etching. In Markku Tilli, Teruaki Motooka, Veli-Matti Airaksinen, Sami Franssila, Mervi Paulasto-Kröckel, and Veikko Lindroos, editors, *Handbook of Silicon Based MEMS Materials and Technologies (Second Edition)*, Micro and Nano Technologies, pages 444 – 469. William Andrew Publishing, Boston, second edition edition, 2015.

[33] G.T. Forcolin, M. Boscardin, F. Ficorella, A. Lai, A. Loi, R. Mendicino, S. Ronchin, and G.-F. Dalla Betta. 3d trenched-electrode pixel sensors: Design, technology and initial results. *Nuclear Instruments and Methods in Physics Research Section A: Accelerators, Spectrometers, Detectors and Associated Equipment*, 981:164437, 2020.

[34] Sandro Cadeddu, Luca Frontini, Adriano Lai, Valentino Liberali, Lorenzo Piccolo, Angelo Rivetti, Jafar Shojaii, and Alberto Stabile. Timespot1: A 28nm CMOS Pixel Read-Out ASIC for 4D Tracking at High Rates. 9 2022.

[35] William R. Leo. *Passage of Radiation Through Matter*, pages 17–68. Springer Berlin Heidelberg, Berlin, Heidelberg, 1994.

[36] Glenn F. Knoll. *Radiation Detection and Measurement*. Wiley, 2010.

[37] Gerald R. Lynch and Orin I. Dahl. Approximations to multiple coulomb scattering. *Nuclear Instruments and Methods in Physics Research Section B: Beam Interactions with Materials and Atoms*, 58(1):6–10, 1991.

[38] F. Scholze, H. Rabus, and G. Ulm. Mean energy required to produce an electron-hole pair in silicon for photons of energies between 50 and 1500 ev. *Journal of Applied Physics*, 84(5):2926–2939, 1998.

[39] Frank Hartmann. *Radiation Damage in Silicon Detector Devices*, pages 135–166. Springer International Publishing, Cham, 2017.

[40] William Shockley. Currents to conductors induced by a moving point charge. *Journal of Applied Physics*, 9:635–636, 1938.

[41] S. Ramo. Currents induced by electron motion. *Proceedings of the IRE*, 27(9):584–585, 1939.

[42] Karl W. Böer and Udo W. Pohl. *Carrier Scattering at High Electric Fields*, pages 931–960. Springer International Publishing, Cham, 2018.

[43] C. DaVia and S.J. Watts. The geometrical dependence of radiation hardness in planar and 3d silicon detectors. *Nuclear Instruments and Methods in Physics Research Section A: Accelerators, Spectrometers, Detectors and Associated Equipment*, 603(3):319–324, 2009.

[44] G. Pellegrini et al. Technology developments and first measurements of Low Gain Avalanche Detectors (LGAD) for high energy physics applications. *Nucl. Instrum. Meth. A*, 765:12–16, 2014.

[45] S.I. Parker, C.J. Kenney, and J. Segal. 3d a proposed new architecture for solid-state radiation detectors. *Nuclear Instruments and Methods in Physics Research Section A: Accelerators, Spectrometers, Detectors and Associated Equipment*, 395(3):328–343, 1997. Proceedings of the Third International Workshop on Semiconductor Pixel Detectors for Particles and X-rays.

[46] L. Paolozzi, R. Cardarelli, S. DÃ©bieux, Y. Favre, D. FerrÃ¨re, S. Gonzalez-Sevilla, G. Iacobucci, M. Kaynak, F. Martinelli, M. Nessi, H. RÃ¼cker, I. Sanna, D.M.S. Sultan, P. Valerio, and E. Zaffaroni. Time resolution and power consumption of a monolithic silicon pixel prototype in sige bicmos technology. *Journal of Instrumentation*, 15(11):P11025, nov 2020.

[47] Gian Matteo Cossu and Adriano Lai. Front-end electronics for timing with pico-seconds precision using 3d trench silicon sensors, 2022.

[48] H.F.-W. Sadrozinski, M. Baselga, S. Ely, V. Fadeyev, Z. Galloway, J. Ngo, C. Parker, D. Schumacher, A. Seiden, A. Zatserklyaniy, N. Cartiglia, G. Pellegrini, P. FernÃ¡ndez-MartÃnez, V. Greco, S. Hidalgo, and D. Quirion. Sensors for ultra-fast silicon detectors. *Nuclear Instruments and Methods in Physics Research Section A: Accelerators, Spectrometers, Detectors and Associated Equipment*, 765:7–11, 2014. HSTD-9 2013 - Proceedings of the 9th International "Hiroshima" Symposium on Development and Application of Semiconductor Tracking Detectors.

[49] G. Aglieri Rinella, D. Alvarez Feito, R. Arcidiacono, C. Biino, S. Bonacini, A. Ceccucci, S. Chiozzi, E. Cortina Gil, A. Cotta Ramusino, H. Danielsson, J. Degrange, M. Fiorini, L. Federici, E. Gamberini, A. Gianoli, J. Kaplon, A. Kleimenova, A. Kluge, R. Malaguti, A. Mapelli, F. Marchetto, E. MartÃn AlbarrÃ¡n,

E. Migliore, E. Minucci, M. Morel, J. NoÃ«l, M. Noy, G. NÃ¼essle, L. Perktold, M. Perrin-Terrin, P. Petagna, F. Petrucci, K. Poltorak, G. Romagnoli, G. Ruggiero, B. Velghe, and H. Wahl. The na62 gigatracker: a low mass high intensity beam 4d tracker with 65 ps time resolution on tracks. *Journal of Instrumentation*, 14(07):P07010, jul 2019.

[50] Federico Siviero et al. Optimization of the gain layer design of ultra-fast silicon detectors. *Nucl. Instrum. Meth. A*, 1033:166739, 2022.

[51] G. Kramberger, M. Carulla, E. Cavallaro, V. Cindro, D. Flores, Z. Galloway, S. Grinstein, S. Hidalgo, V. Fadeyev, J. Lange, I. MandiÄ‡, G. Medin, A. Merlos, F. McKinney-Martinez, M. MikuÅ¾, D. Quirion, G. Pellegrini, M. Petek, H.F.-W. Sadrozinski, A. Seiden, and M. Zavrtanik. Radiation hardness of thin low gain avalanche detectors. *Nuclear Instruments and Methods in Physics Research Section A: Accelerators, Spectrometers, Detectors and Associated Equipment*, 891:68–77, 2018.

[52] T. Croci, A. Morozzi, P. Asenov, A. Fondacci, F. Moscatelli, D. Passeri, V. Sola, L. Menzio, M. Ferrero, M. Mandurrino, R. Arcidiacono, N. Cartiglia, R. Mulargia, E. Robutti, O.A. Marti Villarreal, R. Cirio, R. Sacchi, A. Staiano, V. Monaco, and M. Arneodo. Development and test of innovative low-gain avalanche diodes for particle tracking in 4 dimensions. *Nuclear Instruments and Methods in Physics Research Section A: Accelerators, Spectrometers, Detectors and Associated Equipment*, 1047:167815, 2023.

[53] M. Milanesio, G. Iacobucci, L. Paolozzi, M. Munker, R. Cardella, Y. Gurimskaya, F. Martinelli, A. Picardi, H. RÃ¼cker, A. Trusch, P. Valerio, F. Cadoux, R. Cardarelli, S. Debieux, Y. Favre, D. Ferrere, S. Gonzalez-Sevilla, R. Kotitsa, C. Magliocca, T. Moretti, M. Nessi, J. Saidi, M. Vicente Barreto Pinto, and S. Zambito. Gain measurements of the first proof-of-concept picoad prototype with a 55fe x-ray radioactive source. *Nuclear Instruments and Methods in Physics Research Section A: Accelerators, Spectrometers, Detectors and Associated Equipment*, 1046:167807, 2023.

[54] G. Iacobucci et al. Testbeam results of the Picosecond Avalanche Detector proof-of-concept prototype. *JINST*, 17(10):P10040, 2022.

[55] L. Anderlini, M. Aresti, A. Bizzeti, M. Boscardin, A. Cardini, G.-F. Dalla Betta, M. Ferrero, G. Forcolin, M. Garau, A. Lai, A. Lampis, A. Loi, C. Lucarelli, R. Mendicino, R. Mulargia, M. Obertino, E. Robutti, S. Ronchin, M. Ruspa, and S. Vecchi. Intrinsic time resolution of 3d-trench silicon pixels for charged particle detection. *Journal of Instrumentation*, 15(09):P09029, sep 2020.

[56] Michela Garau. *Sviluppo di un rivelatore Cherenkov per la misura del tempo di arrivo di particelle ionizzanti ultra-relativistiche*. PhD thesis, Universita' Di Cagliari, Cagliari U., 2019. https://pubblicazioni.dsi.infn.it/tesi/gettesi.php?filename=14211-Garau-magistrale.pdf.

[57] Z.H. Cho and R.L. Chase. Comparative study of the timing techniques currently employed with ge detectors. *Nuclear Instruments and Methods*, 98(2):335–347, 1972.

[58] S Meroli, D Passeri, and L Servoli. Energy loss measurement for charged particles in very thin silicon layers. *Journal of Instrumentation*, 6(06):P06013–P06013, jun 2011.

[59] Angelo Loi. *Design and test of a timing optimized 3D silicon sensor for HL-LHC experiments*. PhD thesis, Universita' Di Cagliari, Cagliari U., 2020. http://hdl.handle.net/11584/284136.

[60] D. Brundu, A. Cardini, A. Contu, G.M. Cossu, G.-F. Dalla Betta, M. Garau, A. Lai, A. Lampis, A. Loi, M.M. Obertino, B.G. Siddi, and S. Vecchi. Accurate modelling of 3d-trench silicon sensor with enhanced timing performance and comparison with test beam measurements. *Journal of Instrumentation*, 16(09):P09028, sep 2021.

[61] Synopsys Inc. Synopsys Sentaurus TCAD Version 2018.06 K-2015.06, 2018.

[62] S. Agostinelli et al. Geant4: A simulation toolkit. *Nuclear Instruments and Methods in Physics Research Section A: Accelerators, Spectrometers, Detectors and Associated Equipment*, 506(3):250–303, 2003.

[63] D. Brundu, A. Contu, G. M. Cossu, and A. Loi. Modeling of solid state detectors using advanced multi-threading: The tcode and tfboost simulation packages. *Frontiers in Physics*, 10, 2022.

[64] C. Scharf and R. Klanner. Determination of the electronics transfer function for current transient measurements. *Nuclear Instruments and Methods in Physics Research Section A: Accelerators, Spectrometers, Detectors and Associated Equipment*, 779:1–5, 2015.

[65] Mauro Aresti, Alessandro Cardini, Adriano Lai, Angelo Loi, Gian Matteo Cossu, Michela Garau, Andrea Lampis, Gian-Franco Dalla Betta, and Giulio Forcolin. Laboratory characterization of innovative 3d trench-design silicon pixel sensors using a sub-picosecond precision laser-based testing equipment. In *2020 IEEE Nuclear Science Symposium and Medical Imaging Conference (NSS/MIC)*, pages 1–6, 2020.

[66] Gian Matteo Cossu and Adriano Lai. Front-end Electronics for Timing with pico-seconds precision using 3D Trench Silicon Sensors. 9 2022.

[67] High speed piezo linear stage, 16 mm travel model: CONEX-SAG-LS16P. https://www.newport.com/p/conex-sag-ls16p.

[68] Photonis Netherland B.V., Micro-channel plate photomultiplier model PP23565Y. https://www.photonis.com/products/mcp-pmt.

[69] Rohde & Schwarz, digital oscilloscope RTP084, https://www.rohde-schwarz.com/product/rtp-productstartpage_63493-469056.html.

[70] B. S. Everitt and D. J. Hand. *Mixtures of normal distributions*, pages 25–57. Springer Netherlands, Dordrecht, 1981.

[71] Origami Onefive 10. https://www.nktphotonics.com/products/femtosecond-lasers/origami-lp/.

[72] EKSMA Optics UP1 Pulse picker. https://www.tlsbv.nl/wp-content/uploads/2017/06/TLS-EKSMA-Optics-Pulse-Pickers.pdf.

[73] Mauro Aresti, Alessandro Cardini, Gian Matteo Cossu, Michela Garau, Adriano Lai, Andrea Lampis, and Angelo Loi. A sub-picosecond precision laser-based test station for the measurement of silicon detector timing performances. In *2020 IEEE Nuclear Science Symposium and Medical Imaging Conference (NSS/MIC)*, pages 1–4, 2020.

[74] A. Loi, A. Contu, and A. Lai. Timing optimisation and analysis in the design of 3d silicon sensors: the tcode simulator. *Journal of Instrumentation*, 16(02):P02011, feb 2021.

[75] G. Darbo. Experience on 3d silicon sensors for ATLAS IBL. *Journal of Instrumentation*, 10(05):C05001–C05001, may 2015.

[76] D M S Sultan. *Development of Small-Pitch, Thin 3D Sensors for Pixel Detector Upgrades at HL-LHC*. PhD thesis, University of Trento, 2020. http://eprints-phd.biblio.unitn.it/2574/.

[77] The TRIGA Mark-II reactor , jozef stefan institue in lubjiana, Slovenia, https://www.tuwien.at/en/trigacenter/trigareactor.

[78] C. Patrignani et al. Review of Particle Physics. *Chin. Phys.*, C40(10):100001, 2016.

[79] T. Aushev et al. Physics at Super B Factory. 2010.

[80] Andrea Contu. A method to study long lived charged particles at LHCb. Technical Report LHCb-PUB-2014-032. CERN-LHCb-PUB-2014-032, CERN, Geneva, Apr 2014.

[81] LHCb Collaboration. LHCb VELO Upgrade Technical Design Report. Technical report, 2013.

[82] The Tracker Group of the CMS Collaboration. The CMS Phase-1 Pixel Detector Upgrade. Technical report, CERN, Geneva, 2020.

[83] Technical Design Report for the ATLAS Inner Tracker Strip Detector. Technical report, CERN, Geneva, 2017.

[84] R. Aaij et al. Performance of the LHCb Vertex Locator. *JINST*, 9:09007, 2014.

[85] Torbjörn Sjöstrand, Stephen Mrenna, and Peter" Skands. A brief introduction to PYTHIA 8.1. *Comput.Phys.Commun.*, 178:852–867, 2008.

[86] D. J. Lange. The EvtGen particle decay simulation package. *Nucl. Instrum. Meth.*, A462:152–155, 2001.